

FIRST-PRINCIPLES COMPUTATIONAL INVESTIGATIONS OF
TITANIUM CARBIDE NANOCRYSTALS

by

QIN ZHANG

(Under the direction of Steven P. Lewis)

ABSTRACT

Stable transition-metal carbide nanocrystals were observed to form with sizable abundance in laser vaporization molecular-beam experiments of the 1990's [1, 2]. Inspired by the experimental observations, I have carried out first-principles total-energy calculations, employing density functional theory (DFT), for $3 \times 3 \times 3$ titanium carbide nanocrystals. Two sibling nanocrystals, $\text{Ti}_{14}\text{C}_{13}$ and $\text{Ti}_{13}\text{C}_{14}$, are compared in this dissertation. Both of them can be viewed as fragments of bulk TiC, but the first was found to be abundant and stable in the experiments while the second was not seen at all. The analysis of their structural, energetic, and vibrational properties shows differences in the nearest-neighbor Ti-C bonding in these two species and a significant weakening in the bond to the corner carbon atom in $\text{Ti}_{13}\text{C}_{14}$. In addition, an electronic level analysis, aided by visualization of the molecular orbitals of $\text{Ti}_{14}\text{C}_{13}$ and $\text{Ti}_{13}\text{C}_{14}$, shows the different adaptability for orbitals available to titanium and carbon atoms in different geometrical arrangements, resulting in a difference in the Ti-C bond strength in these nanocrystals.

In this dissertation, I also examine the effects of alloying on titanium carbide nanocrystals. DFT calculations are performed on a system similar to $\text{Ti}_{14}\text{C}_{13}$, but with one of its titanium atoms replaced with a zirconium atom, yielding $\text{Ti}_{13}\text{ZrC}_{13}$. Two categories of $\text{Ti}_{13}\text{ZrC}_{13}$ species — $\text{Ti}_{13}\text{Zr}^{cor}\text{C}_{13}$, with the zirconium atom at a corner site, and $\text{Ti}_{13}\text{Zr}^{fc}\text{C}_{13}$, with the zirconium atom at a face-center site — are compared to each other and to pure $\text{Ti}_{14}\text{C}_{13}$, in structural, energetic, and vibrational properties. My analysis shows that the change in the vibrational spectrum of $\text{Ti}_{13}\text{Zr}^{cor}\text{C}_{13}$ due to alloying is primarily the effect of the mass difference between Zr and Ti, while the change in $\text{Ti}_{13}\text{Zr}^{fc}\text{C}_{13}$ also reflects a modification of the bond strength in the molecule. Thus, the IR spectrum of $\text{Ti}_{13}\text{Zr}^{fc}\text{C}_{13}$ shows more prominent new features than that of $\text{Ti}_{13}\text{Zr}^{cor}\text{C}_{13}$. Because of its lower ground total-energy, $\text{Ti}_{13}\text{Zr}^{cor}\text{C}_{13}$ is expected to be substantially more abundant in experiments, and thus the IR spectrum of $\text{Ti}_{13}\text{ZrC}_{13}$ is predicted to be closer to that of $\text{Ti}_{13}\text{Zr}^{cor}\text{C}_{13}$.

INDEX WORDS: Clusters, Metal, Carbides, Nanocrystals, $\text{Ti}_{14}\text{C}_{13}$, M_8C_{12}

FIRST-PRINCIPLES COMPUTATIONAL INVESTIGATIONS OF
TITANIUM CARBIDE NANOCRYSTALS

by

QIN ZHANG

B.S., Shanghai Jiao Tong University, 1996

M.S., University of Georgia, 2004

A Dissertation Submitted to the Graduate Faculty
of The University of Georgia in Partial Fulfillment

of the

Requirements for the Degree

DOCTOR OF PHILOSOPHY

ATHENS, GEORGIA

2006

© 2006

Qin Zhang

All Rights Reserved

FIRST-PRINCIPLES COMPUTATIONAL INVESTIGATIONS OF
TITANIUM CARBIDE NANOCRYSTALS

by

QIN ZHANG

Approved:

Major Professor: Steven P. Lewis

Committee: Michael A. Duncan
David P. Landau
Heinz-Bernd Schüttler

Electronic Version Approved:

Maureen Grasso
Dean of the Graduate School
The University of Georgia
May 2006

DEDICATION

To my parents Chumin Zhang and Weihua Shen, and my beloved wife Yong.

ACKNOWLEDGMENTS

First and foremost, I wish to express my sincere appreciation to my mentor, professor Steven Lewis. His insightful suggestions are invaluable to my research. I cannot thank him enough for his excellent guidance, unlimited patience, and strong friendship.

I would like to thank all members in my advisory committee, Professor Steven Lewis, Michael Duncan, David Landau and Heinz-Bernd Schüttler. The final version of this dissertation has greatly benefitted from their proofreading. I feel extremely lucky to have had the opportunity to learn from such an impressive and supportive committee.

I appreciate greatly for the opportunity to collaborate with Professor Michael Duncan and his experimental group. My deep gratitude also goes to Professor Eileen Kraemer for her feedbacks and suggestions in my programming.

I enjoyed the warm and friendly atmosphere in the physics department of UGA. Especially, I am grateful to Dr. Craig Wiegert and Dr. Shan-Ho Tsai for the assistance in the visualization of wavefunctions. I wish to thank Scott Thompson, Alvin Shubert and Benjamin Joseph Cooley for doing research together in Dr. Lewis's research group.

Finally, I want to thank all those giving me a blessing. This research can never be completed without the continuous support, love, and encouragement of my family and my friends. This dissertation is entirely dedicated to them.

TABLE OF CONTENTS

	Page
ACKNOWLEDGMENTS	v
LIST OF FIGURES	ix
LIST OF TABLES	xii
CHAPTER	
1 INTRODUCTION	1
1.1 DISSERTATION OBJECTIVE	1
1.2 DISSERTATION ORGANIZATION	3
2 BACKGROUND	5
2.1 DISCOVERY OF METAL-CARBON NANOCCLUSERS	5
2.2 TRUNCATED CARBON DEFICIENT NANOCRYSTALS	7
2.3 VIBRATIONAL SPECTROSCOPY OF METAL-CARBIDE NANOCCLUSERS AND NANOCRYSTALS	9
3 FIRST-PRINCIPLES TOTAL-ENERGY METHODOLOGY	12
3.1 INTRODUCTION TO DENSITY FUNCTIONAL THEORY	12
3.2 APPROXIMATIONS FOR EXCHANGE-CORRELATION ENERGY	15
3.3 PLANE-WAVE BASIS SET AND K-POINT SAMPLING IN PERIODIC CELLS	17
3.4 PSEUDOPOTENTIALS	19
4 PRELIMINARY CONSIDERATIONS AND CALCULATIONS	21

4.1	CHOICES FOR CALCULATIONS ON Ti-C NANOCRYSTALS . . .	21
4.2	CONVERGENCE TESTING AND COMMON PARAMETERS . . .	22
4.3	BULK Ti-C CALCULATIONS	24
5	STRUCTURE AND ENERGETICS	27
5.1	RELAXED STRUCTURE	27
5.2	GROUND-STATE ENERGY	29
6	VIBRATIONAL ANALYSIS	31
6.1	HARMONIC FORCE-CONSTANT MODEL	31
6.2	NORMAL MODES OF VIBRATION	35
6.3	DENSITY OF STATES AND IR SPECTRUM	37
7	ELECTRONIC STRUCTURE ANALYSIS	47
7.1	ELECTRONIC ORBITALS	47
7.2	VISUALIZATION OF WAVE FUNCTIONS	48
7.3	ANALYSIS OF MOLECULAR ORBITAL ENERGY LEVEL DIA- GRAMS	51
7.4	MOLECULAR BONDING OF $Ti_{14}C_{13}$ AND $Ti_{13}C_{14}$	57
8	STABILITY OF CORNER CARBON ATOMS	62
8.1	NEAREST-NEIGHBOR Ti-C BONDING ENERGY	62
8.2	VIBRATIONAL MODES RELATED TO CORNER ATOMS . . .	63
8.3	DISPLACEMENT OF CORNER ATOM ALONG BODY DIAGONAL	66
8.4	CONNECTION TO THE ELECTRONIC STRUCTURE	68
9	ALLOYING EFFECTS ON THE Ti SITES	70
9.1	POSSIBILITIES OF $Ti_{14-x}Zr_xC_{13}$ NANOCRYSTALS	70
9.2	$Ti_{13}Zr^{cor}C_{13}$	71
9.3	$Ti_{13}Zr^{fc}C_{13}$	79

9.4	Ti ₁₃ ZrC ₁₃ AND Ti ₁₄ C ₁₃	89
10	CONCLUSIONS	93
APPENDIX		
A	A TOOL TO VISUALIZE NORMAL MODES OF VIBRATION	95
A.1	INTRODUCTION	95
A.2	USER INTERFACE	96
A.3	SYSTEM CONFIGURATION	98
A.4	VISUALIZING VIBRATIONAL MODES	103
A.5	SUMMARY	106
	BIBLIOGRAPHY	106

LIST OF FIGURES

2.1	Mass spectrum of titanium-carbon clusters	6
2.2	Two possibilities for $3 \times 3 \times 3$ Ti-C nanocrystal species	8
2.3	IR-REMPI spectrum of $\text{Ti}_{14}\text{C}_{13}$ nanocrystals	11
4.1	Titanium carbide nanocrystal species selected for calculations	23
4.2	Bulk TiC total energy vs. cell vector length	26
5.1	Four relaxed Ti-C nanocrystal species	28
6.1	Imaginary modes for Ti_6C_{13}	40
6.2	Vibrational density of states for $\text{Ti}_{14}\text{C}_{13}$	43
6.3	Vibrational density of states for $\text{Ti}_{13}\text{C}_{14}$	44
6.4	Comparison between the experimental spectrum and calculated IR spectrum for $\text{Ti}_{14}\text{C}_{13}$	45
6.5	Vibrations in IR-active modes of $\text{Ti}_{14}\text{C}_{13}$	46
7.1	Kohn-Sham energy level diagram of $\text{Ti}_{14}\text{C}_{13}$	52
7.2	Kohn-Sham energy level diagram of $\text{Ti}_{13}\text{C}_{14}$	53
7.3	Electron orbitals of $\text{Ti}_{14}\text{C}_{13}$	
	(a) Orbital 5, -55.937 eV, t_{2g} symmetry	
	(b) Orbital 8, -55.937 eV, a_{2u} symmetry	
	(c) Orbital 10, -55.850 eV, t_{1u} symmetry	
	(d) Orbital 13, -55.842 eV, e_g symmetry	55

7.4	Electron orbitals of $\text{Ti}_{14}\text{C}_{13}$	
	(a) Orbital 15, -33.380 eV, t_{2g} symmetry	
	(b) Orbital 23, -33.247 eV, a_{1g} symmetry	
	(c) Orbital 51, -32.760 eV, t_{2u} symmetry	
	(d) Orbital 54, -32.737 eV, t_{1g} symmetry	56
7.5	Electron orbitals of $\text{Ti}_{14}\text{C}_{13}$	
	(a) Orbital 59, -9.661 eV, t_{1u} symmetry	
	(b) Orbital 67, -8.819 eV, t_{2g} symmetry	57
7.6	Electron orbitals of $\text{Ti}_{14}\text{C}_{13}$	
	(a) HOMO-1, -1.258 eV, t_{2u} symmetry	
	(b) HOMO, 0 eV, t_{2g} symmetry	
	(c) LUMO, 0.094 eV, a_{1g} symmetry	
	(d) LUMO+1, 0.191 eV, a_{2u} symmetry	58
7.7	Electron orbitals of $\text{Ti}_{13}\text{C}_{14}$	
	(a) HOMO-1, -0.653 eV, t_{1g} symmetry	
	(b) HOMO, 0 eV, t_{1u} symmetry	
	(c) LUMO, 0.238 eV, t_{2g} symmetry	
	(d) LUMO+1, 0.827 eV, e_g symmetry	59
8.1	A_{2u} mode for $\text{Ti}_{14}\text{C}_{13}$ and for $\text{Ti}_{13}\text{C}_{14}$	65
8.2	Energy variations due to a displacement of one corner atom along the body diagonal of $\text{Ti}_{14}\text{C}_{13}$ and $\text{Ti}_{13}\text{C}_{14}$	67
9.1	Equilibrium structure of $\text{Ti}_{13}\text{Zr}^{cor}\text{C}_{13}$ and $\text{Ti}_{14}\text{C}_{13}$	73
9.2	IR density of states of $\text{Ti}_{13}\text{Zr}^{cor}\text{C}_{13}$	75
9.3	Computed IR spectrum for $\text{Ti}_{13}\text{Zr}^{cor}\text{C}_{13}$ compared to that of $\text{Ti}_{14}\text{C}_{13}$	78
9.4	Equilibrium structure of $\text{Ti}_{13}\text{Zr}^{fc}\text{C}_{13}$ and $\text{Ti}_{14}\text{C}_{13}$	79
9.5	IR density of states of $\text{Ti}_{13}\text{Zr}^{fc}\text{C}_{13}$	84

9.6	Vibrations mainly activating the body-center atom in $\text{Ti}_{13}\text{Zr}^{fc}\text{C}_{13}$. . .	87
9.7	Computed IR spectrum for $\text{Ti}_{13}\text{Zr}^{fc}\text{C}_{13}$ compared to that of $\text{Ti}_{14}\text{C}_{13}$.	88
9.8	IR spectrum of $\text{Ti}_{13}\text{ZrC}_{13}$ calculated using random substitution model	91
A.1	Main Layout of OSCILLATOR	96
A.2	Field of View in OSCILLATOR	97
A.3	Interactive dialog for adding or editing an atom	99
A.4	Visualization of a normal mode	105

LIST OF TABLES

4.1	Computational parameters for TiC nanosystems and single atoms . . .	25
5.1	Relaxed structure for $\text{Ti}_{14}\text{C}_{13}$, $\text{Ti}_{13}\text{C}_{14}$, Ti_6C_{13} and Ti_{13}C_6	29
5.2	Raw ground-state total energies of the individual titanium and carbon atoms and the nanocrystals	30
5.3	Average Ti-C bond energy	30
6.1	Vibrational modes for $\text{Ti}_{14}\text{C}_{13}$	38
6.2	Vibrational modes for $\text{Ti}_{13}\text{C}_{14}$	38
6.3	Vibrational modes for Ti_{13}C_6	39
6.4	Vibrational modes for Ti_6C_{13}	39
7.1	Kohn-Sham orbitals for $\text{Ti}_{14}\text{C}_{13}$	49
7.2	Kohn-Sham orbitals for $\text{Ti}_{13}\text{C}_{14}$	50
9.1	Positions of atoms in $\text{Ti}_{13}\text{Zr}^{cor}\text{C}_{13}$ and $\text{Ti}_{14}\text{C}_{13}$	72
9.2	Mode splitting from $\text{Ti}_{14}\text{C}_{13}$ (O_h) to $\text{Ti}_{13}\text{Zr}^{cor}\text{C}_{13}$ (C_{3v})	73
9.3	Normal-mode frequencies and symmetry labels for $\text{Ti}_{13}\text{Zr}^{cor}\text{C}_{13}$	74
9.4	Normal-mode frequencies and symmetry labels for $\text{Ti}_{13}\text{Zr}^{cor}\text{C}_{13}$, with force-constant matrix from $\text{Ti}_{14}\text{C}_{13}$	77
9.5	Positions of atoms in $\text{Ti}_{13}\text{Zr}^{fc}\text{C}_{13}$ and $\text{Ti}_{14}\text{C}_{13}$	80
9.6	Mode splitting from $\text{Ti}_{14}\text{C}_{13}$ (O_h) to $\text{Ti}_{13}\text{Zr}^{fc}\text{C}_{13}$ (C_{4v})	81
9.7	Normal-mode frequencies and symmetry labels for $\text{Ti}_{13}\text{Zr}^{fc}\text{C}_{13}$	82

9.8	Normal-mode frequencies and symmetry labels for $\text{Ti}_{13}\text{Zr}^{fc}\text{C}_{13}$, with force-constant matrix from $\text{Ti}_{14}\text{C}_{13}$	83
9.9	Shifts of normal-mode frequencies in going from $\text{Ti}_{14}\text{C}_{13}$ to $\text{Ti}_{13}\text{Zr}^{fc}\text{C}_{13}$	85
9.10	Ti-C and Zr-C bond-length comparison in bulk and $\text{Ti}_{13}\text{ZrC}_{13}$ nanocrystals	89

CHAPTER 1

INTRODUCTION

1.1 DISSERTATION OBJECTIVE

Stable transition-metal carbide clusters are an important class of nanoscale clusters. They were discovered in laser vaporization molecular-beam experiments in the early 1990s [1–5], where a series of ‘magic number’ peaks appeared in time-of-flight mass spectra, indicating cluster compositions that are relatively stable. There are two types of stable species: the metallocarbohedrene (met-car) M_8C_{12} , where M stands for one of many possible metal species, and the larger so called “nanocrystals” that exhibit $\sim 1:1$ metal/carbon stoichiometries characteristic of bulk metal carbides, thus suggesting $N_1 \times N_2 \times N_3$ lattice structures for this type of cluster. Numerous previous ab initio studies [6–22] have mostly investigated the properties of met-car clusters. In this dissertation, I focus on the nanocrystals, the other prominent class of metal-carbide nanoclusters, and in particular, Ti-C nanocrystals. These species can be viewed as fragments of bulk TiC, and exhibit a range of interesting properties that the bulk does not have. For example, not all ideal cubic fragments of bulk TiC are shown as stable nanocrystals in the experiments, and the stable nanocrystals are often carbon deficient. To give a theoretical explanation for the questions raised in the experiments, I perform first principle calculations on $3 \times 3 \times 3$ titanium carbide nanocrystals using density functional theory (DFT) [23, 24], one of the most prominent approaches offering the capability of efficiently computing the electronic structure, total energy and other properties of molecular and condensed

matter systems. The $3 \times 3 \times 3$ nanocrystals, the main topic of this dissertation, are in the smallest size of the nanocrystal class, but formed in the greatest abundance among the nanocrystals in experiments, by far. Viewed as truncations of bulk TiC, which has the same structure as NaCl, there are two possible structures that can form $3 \times 3 \times 3$ cubes. All metal atoms are either at the eight corner site and six face-center sites, or at the one body-center sites and twelve edge-center sites. The former yields $\text{Ti}_{14}\text{C}_{13}$ and the latter yields $\text{Ti}_{13}\text{C}_{14}$. However, only $\text{Ti}_{14}\text{C}_{13}$ is seen as stable in the experiments. From the ab initio investigation on their structural, energetic, vibrational and electronic properties, I try to give a physical explanation for the prominence of $3 \times 3 \times 3$ nanocrystal $\text{Ti}_{14}\text{C}_{13}$ and absence of the other possible $3 \times 3 \times 3$ nanocrystal $\text{Ti}_{13}\text{C}_{14}$. This sheds light on how carbon deficiency in nanocrystals is related to the strength of the bonds to the atoms at corners of the nanocrystals.

In addition to studying on the pure transition-metal carbide nanocrystals, I also report the zirconium-alloy effects in the $3 \times 3 \times 3$ nanocrystal. One metal atom of $\text{Ti}_{14}\text{C}_{13}$, which is observed abundant in the experiments, is replaced by a zirconium atom, resulting in $\text{Ti}_{13}\text{ZrC}_{13}$. By considering symmetries of the $3 \times 3 \times 3$ cubic structure, I divide $\text{Ti}_{13}\text{ZrC}_{13}$ nanocrystals into two possible categories, depending on the distribution of the zirconium atom on the metal sites in the $3 \times 3 \times 3$ structure. One has the zirconium atom at the corner of the nanocrystal, named $\text{Ti}_{13}\text{Zr}^{cor}\text{C}_{13}$, and the other has the zirconium atom at the face-center of the nanocrystal, named $\text{Ti}_{13}\text{Zr}^{fc}\text{C}_{13}$. By comparing these two isomers of $\text{Ti}_{13}\text{ZrC}_{13}$, and describing their similarities and differences to $\text{Ti}_{14}\text{C}_{13}$, I demonstrate the effect on structural and bonding properties due to the introduction of the zirconium atom. I calculate the IR spectrum of the nanocrystal $\text{Ti}_{13}\text{ZrC}_{13}$, using a random zirconium occupation model. After making a correction to this model, I predict that the IR spectrum of the alloy

carbide nanocrystal $\text{Ti}_{13}\text{ZrC}_{13}$ is dominated by the IR spectrum of $\text{Ti}_{13}\text{Zr}^{cor}\text{C}_{13}$, which is very similar to the IR spectrum of pure metal carbide nanocrystal $\text{Ti}_{14}\text{C}_{13}$.

1.2 DISSERTATION ORGANIZATION

The material in this dissertation is arranged in the following manner: The experimental background on the discovery of metal carbide clusters and nanocrystals is first introduced. Then the theoretical methods applying density functional theory are described, and the parameters used in the calculations are specified. Following a detailed investigation of the structural, energetic, vibrational and electronic properties of titanium carbide nanocrystals, the alloy effects of replacing one titanium atom with one zirconium atom are finally discussed.

The chapters are ordered as follows: Chapter 2 gives a review of the experimental development on the metal carbide nanocrystals. Chapter 3 provides an overview of density functional theory, the basis of my calculations. Chapter 4 describes the choices of Ti-C nanocrystals to study, the parameters for the DFT calculations, convergence tests and other preliminary considerations. The calculation for bulk TiC is also discussed in this chapter, as the nanocrystal structure will be given in comparison with the bulk structure in the later chapters. Chapter 5 gives the results and comparisons on structural and energetic properties of $\text{Ti}_{14}\text{C}_{13}$ and $\text{Ti}_{13}\text{C}_{14}$. Two auxiliary systems, Ti_6C_{13} and Ti_{13}C_6 , which are just the truncated nanocrystals obtained by removing the corner atoms of $\text{Ti}_{14}\text{C}_{13}$ and $\text{Ti}_{13}\text{C}_{14}$, are also included to prepare the discussion of the stability of corner atoms. Chapter 6 introduces a force-constant model for the vibrational analysis and presents the results of calculating the vibrational modes of the titanium carbide nanocrystals. The calculated infrared spectrum of $\text{Ti}_{14}\text{C}_{13}$ is compared here with the experimental data. Chapter 7 gives the detailed electronic structure analysis of $\text{Ti}_{14}\text{C}_{13}$ and $\text{Ti}_{13}\text{C}_{14}$. The Kohn-Sham

waves functions obtained in the DFT calculation are visualized, which help us understand the formation of bonds and their connection to electronic structure near the highest occupied molecular orbital (HOMO). Chapter 8 summarizes the structural, energetic and vibrational analysis of two types of $3 \times 3 \times 3$ titanium carbide nanocrystals and accumulates the evidence that the carbon atoms are weakly bonded when they occupy corner sites. How this analysis explains why we only see $\text{Ti}_{14}\text{C}_{13}$ and the reason for the carbon deficiency in nanocrystals is then discussed. Chapter 9 presents the computational results of $\text{Ti}_{13}\text{ZrC}_{13}$, which is similar to $\text{Ti}_{14}\text{C}_{13}$ except that one titanium atom is replaced by a zirconium atom. The alloying effects on the vibrational spectrum due to changes in the mass and bonding in the nanocrystals are shown. Finally, I summarize and give conclusions for this dissertation in chapter 10. In the appendix, I briefly introduce a 3D visualization tool that I developed to study normal modes of vibrations. Some figures in this dissertation are generated with this tool.

CHAPTER 2

BACKGROUND

2.1 DISCOVERY OF METAL-CARBON NANOCCLUSERS

In 1992 [3], Guo, Kerns, and Castleman discovered a stable and abundant cluster with mass 518 amu during the course of studying the dehydrogenation reactions of hydrocarbons. The new stable cluster was known to be composed of titanium atoms and carbon atoms. At first it was not possible to identify the specific stoichiometry based on the mass, because the mass of the main isotope of Ti is 48 amu, exactly four times the mass of ^{12}C . On repeating the experiment with ^{13}C instead, the experimentalists were able to deduce a stoichiometry of 8 metal atoms and 12 carbons.

Soon after the discovery of Ti_8C_{12} , it was shown that this species was not the only cluster form for metal-carbon nanoparticles. In the investigation of the titanium carbon and vanadium carbon clusters, a family of larger metal-carbon systems were observed by Pilgrim and Duncan [1, 2] in laser-induced photodissociation experiments in 1993. The data display a series magic number peaks in the mass spectrum.

A part of the mass spectrum reported by Pilgrim and Duncan [1, 25, 26] is shown in figure 2.1. Confirmed again by using ^{13}C later, one sharp peak with mass 528 amu was assigned to be the metallo-carbohedrenes or “met-cars” Ti_8C_{12} . The clusters corresponding to peaks at higher masses were indexed to be perfect or nearly perfect $N_1 \times N_2 \times N_3$ nanocrystals. These nanocrystals can be viewed as fragments of bulk TiC, which has the same structure as NaCl. For example, in the Ti_nC_m

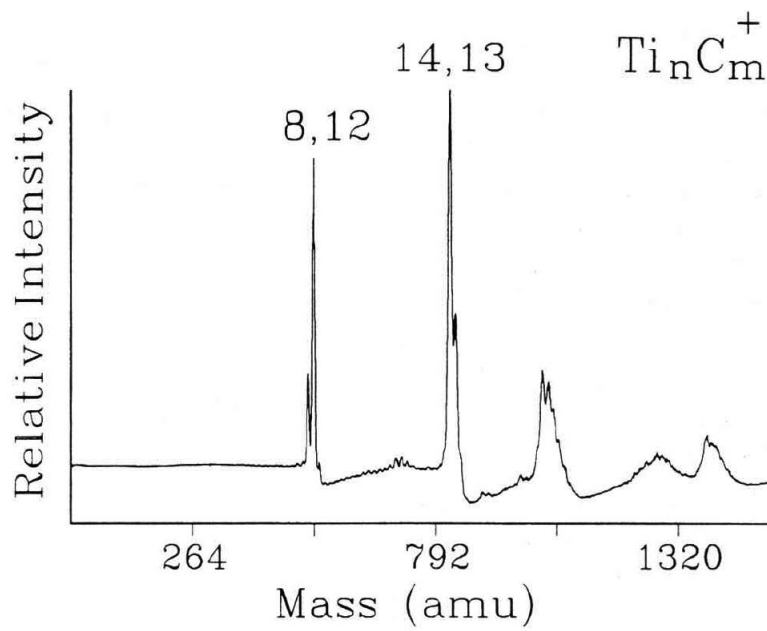


Figure 2.1: Mass spectrum of titanium-carbon clusters obtained by Pilgrim and Duncan (Reprinted from ref. [1]). The Ti_8C_{12} and $\text{Ti}_{14}\text{C}_{13}$ clusters are formed preferentially. A series of larger clusters are also observed.

spectrum in figure 2.1, the other prominent mass peak at mass 828 amu is assigned to the stoichiometry $\text{Ti}_{14}\text{C}_{13}$, which has the right composition to be a $3 \times 3 \times 3$ cubic nanocrystal.

The nanocrystals all exhibit $\sim 1:1$ metal carbon stoichiometries characteristic of bulk-like cubic lattice structures. The presence of the “met-car” nanoclusters and the metal-carbide nanocrystals has been confirmed by many experiments since their discovery. They have been obtained from photofragmentation, from metastable decay, and from other techniques as well [27]. Although transition-metal carbide nanoclusters and nanocrystals were first discovered for titanium as the metal, other transition metals like vanadium, zirconium, etc. have been observed to form similar nanoclusters and nanocrystals, as well [2, 28–31].

2.2 TRUNCATED CARBON DEFICIENT NANOCRYSTALS

The ideal titanium carbide nanocrystals are like the full cubic fragments of bulk TiC, which has the rock-salt structure. The metal atoms and carbon atoms in the ideal nanocrystals sit on alternating sites of the $N_1 \times N_2 \times N_3$ truncated lattice. In the ideal structure, the number of carbon atoms is either the same as the number of titanium atoms, or at most differs by one, if N_1 , N_2 and N_3 are all odd numbers. Some ideal nanocrystals, for example the $3 \times 3 \times 3$ $\text{Ti}_{14}\text{C}_{13}$ and $3 \times 3 \times 5$ $\text{Ti}_{23}\text{C}_{22}$, are produced in the gas phase in the laser vaporization molecular beam experiments [1, 2, 32].

But in these experiments, one interesting observation is that not all nanocrystals are observed as the ideal fragments of bulk TiC, and some are often carbon deficient. The phenomenon can be seen for the nanocrystals with different sizes. If all the edges of the nanocrystal have an odd number of atoms, like the $3 \times 3 \times 3$ nanocrystal, the atoms at all eight corners of the nanocrystal have to be of the same species. In other

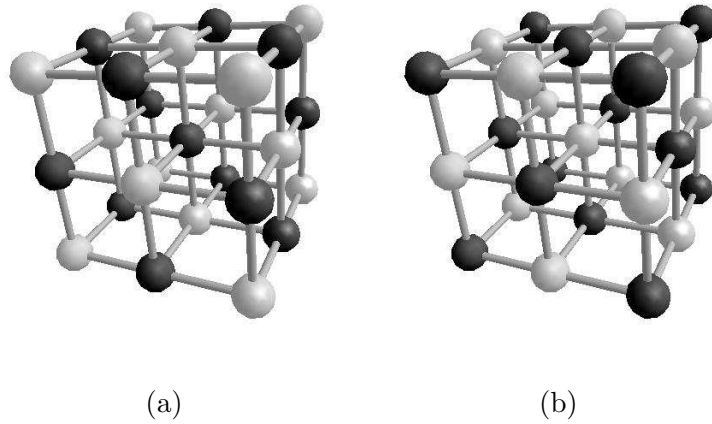


Figure 2.2: Two possibilities for $3 \times 3 \times 3$ Ti-C nanocrystal species.

(a) $\text{Ti}_{14}\text{C}_{13}$.

(b) $\text{Ti}_{13}\text{C}_{14}$.

Titanium atoms are indicated by white spheres and carbon atoms are indicated by black spheres. This same color scheme is used through this dissertation for ball-and-stick figures.

words, they have to be either all metal atoms or all carbon atoms. Although the perfect structure for nanocrystals with an odd number of atoms along each edges is observed, the number of metal atoms for these observed nanocrystals is always one more than the number of carbon atoms, indicating that the nanocrystals formed are of the type with metal atoms, not carbon atoms, at all corners. For example, the $3 \times 3 \times 3$ nanocrystal could have two possible types, as shown in figure 2.2. One possibility, $\text{Ti}_{14}\text{C}_{13}$, has titanium atoms on its six face-center sites and eight corner sites and carbon atoms on the body-center site and twelve edge-center sites. The other possibility, $\text{Ti}_{13}\text{C}_{14}$, has carbon atoms on its face-center and corner sites and titanium atoms on the body-center and edge-center sites. They both can be

viewed as fragments of the bulk TiC. However, $\text{Ti}_{14}\text{C}_{13}$ is observed abundance in the experiments, and its $3 \times 3 \times 3$ sibling, $\text{Ti}_{13}\text{C}_{14}$, which is also a possible fragment of bulk TiC, is not seen at all in the experiments [1, 2, 32, 33].

If at least one edge has an even number of atoms, the alternation of atoms along the edge requires that the corners at the two ends of the edge cannot be occupied by the same type of atom. For example, unlike the $3 \times 3 \times 3$ nanocrystal, there is only one ideal $3 \times 3 \times 4$ nanocrystal $\text{M}_{18}\text{C}_{18}$, where M is a metal like titanium or vanadium. For an ideal $3 \times 3 \times 4$ structure, four corners sites on one 3×3 face must be occupied by metal and the four remaining corners on the other 3×3 face, by carbon. However, the nanocrystals with an even number of atoms along one or more edges are never observed with the ideal stoichiometry, but always show missing carbon atoms. For example, vanadium-carbide nanocrystals exhibit a trend to have four fewer carbon atoms than the ideal structure for the $3 \times 3 \times 4$ and $3 \times 4 \times 4$ nanocrystals. This suggests that the four carbon atoms at corner sites of the ideal version of the nanocrystals are absent [32]. The situation is more complicated in the mass spectrum of larger titanium carbide nanocrystals, as titanium has multiple stable isotopes. But if isotopically pure titanium were used, a similar picture for titanium carbide nanocrystals would be observed in all likelihood.

2.3 VIBRATIONAL SPECTROSCOPY OF METAL-CARBIDE NANOCLUSTERS AND NANOCRYSTALS

The infrared absorption or emission spectrum can help us understand the rotational and vibrational motions of a molecule and thus understand the internal structure and properties [34]. Such experimental techniques, for example, have been used to measure the vibrational spectra of carbon nanoclusters in soot [27]. However, metal-carbide clusters, such as the M_8C_{12} met-car and $\text{M}_{14}\text{C}_{13}$ nanocrystals, are produced

by laser vaporization in pulsed-nozzle sources [1, 2]. In these experiments, they are produced at low density in the gas phase, and it is not possible to use standard techniques to obtain the IR absorption spectrum. In the late 1990s, the introduction of a new technique called the infrared resonance-enhanced multiphoton ionization (IR-REMPI) method made it possible to measure the infrared spectrum [35] for strongly bound clusters produced in the gas phase in laser vaporization molecular beam experiments. Infrared multiphoton excitation with a pulsed free-electron laser results in thermionic electron emission for neutral clusters and the resulting ions are detected in a time-of-flight mass spectrometer. Multiphoton ionization is strongly enhanced on an infrared-active vibrational resonance of the nanocluster. Although this IR-REMPI spectrum is not the same as the linear absorption spectrum, it can be quite similar and it yields valuable information on the IR optical properties [36]. The IR-REMPI method has been applied on titanium carbide nanoclusters and nanocrystals in molecular beams. As shown in figure 2.3, reprinted from the experimental work of ref. [35], the $3 \times 3 \times 3$ nanocrystal $\text{Ti}_{14}\text{C}_{13}$ has a strong IR resonance peak that appears at 485 cm^{-1} and the second IR band that appears at around 630 cm^{-1} .

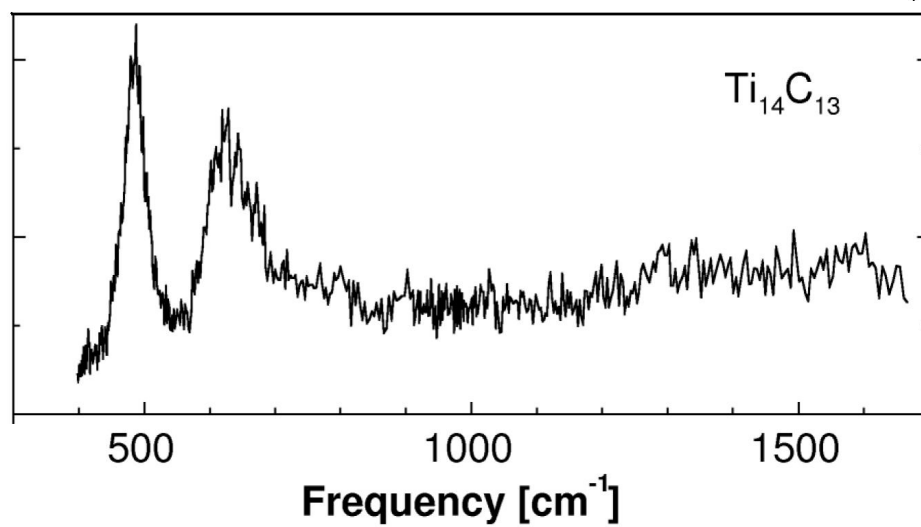


Figure 2.3: IR-REMPI spectrum of $\text{Ti}_{14}\text{C}_{13}$ nanocrystals (Reprinted from ref. [36]).

CHAPTER 3

FIRST-PRINCIPLES TOTAL-ENERGY METHODOLOGY

3.1 INTRODUCTION TO DENSITY FUNCTIONAL THEORY

Density Functional Theory (DFT) [23, 24] is arguably the most successful quantum mechanical approach to offer the capability of computing the electronic structure, total energy and other properties of molecular and condensed matter systems. The DFT method has undergone great progress in the past decades [37–40], and various approaches for solving the DFT equations have been implemented in many different computer codes [41]. In this chapter, I will introduce the basic theorems and approximations on which my calculations of metal-carbide nanocrystals are based. For simplicity, electron spins are not included in the discussion, as spin consideration will not be significant to the present research.

Real material and molecular systems, including the nanocrystal systems I have studied, are essentially many-body systems of interacting electrons and atomic nuclei. Because of the very large difference in mass between the electrons and nuclei for all atomic species except, perhaps, hydrogen, and the fact that the forces electrons and nuclei exert on each other are equal in magnitude, the electrons respond nearly instantaneously to the motion of the nuclei. Thus the nuclear motion can be treated adiabatically, or even ignored, leading to a separation of electronic and nuclear coordinates in the many-body wave function. This adiabatic approximation, also called the Born-Oppenheimer approximation [42], separates the full many-body problem to the problem of electrons and fixed nuclei. If nuclear dynamics are needed

for a given problem, the electronic contribution to the potential felt by the nuclei will be the ground-state electronic energy computed for the instantaneous configuration of the nuclei. So the Hamiltonian for the solution of the dynamics of the electrons in some frozen-in potential of the nuclei can be written as equation 3.1

$$\hat{H} = -\frac{1}{2} \sum_i \nabla_i^2 + \sum_i V_{ext}(\mathbf{r}_i) + \frac{1}{2} \sum_{i \neq j} \frac{1}{|\mathbf{r}_i - \mathbf{r}_j|} + \frac{1}{2} \sum_{I \neq J} \frac{1}{|\mathbf{R}_I - \mathbf{R}_J|}, \quad (3.1)$$

where Hartree atomic units are used ($\hbar = m_e = e = \frac{4\pi}{\epsilon_0} = 1$). The parameter \mathbf{r}_i is the coordinate of the i^{th} electron and \mathbf{R}_I is the coordinate of the I^{th} nucleus, or ion. There are four terms in the above Hamiltonian. The first term is the kinetic energy operator for the electrons. The second term is the potential energy of the electrons due to the fixed nuclei, and perhaps, other external fields that may be present. The third term is the repulsive electron-electron Coulomb interaction. And the last term is the classical Coulomb interaction energy of the nuclei, which is a constant for fixed nuclei. While this term, as a constant energy shift, does not affect the electrons, it is useful to include here so that the resulting total energy, viewed as parametrically depending on nuclear positions, can later be used as the potential energy for nuclear motion.

The traditional quantum mechanical approach to the system defined by the above Hamiltonian is based on solving for complicated many-electron wave functions. As each electron has 3 degrees of freedom, the many-body wave functions of an N -electron system includes $3N$ variables. The basic idea of DFT is to describe the multi-electron system via the electron density, rather than the many-body wave functions. The relatively low computational expense is the main advantage, as the density is only a function of \mathbf{r} , the basic variable of the system which is defined by only 3 spatial coordinates, much fewer than the $3N$ variables in the approach using many-electron wave functions.

The theorems established by Hohenberg and Kohn [23] in 1964 give DFT a firm base. The first Hohenberg-Kohn theorem asserts the existence of a one-to-one mapping between the ground-state electron density and the ground-state wave function of a many-electron system. In the approach of Hohenberg and Kohn [23, 43], the potential $V_{ext}(\mathbf{r})$ is determined uniquely, except for a constant, by the ground-state electron density $n(\mathbf{r})$. The Hamiltonian can be fully determined after $V_{ext}(\mathbf{r})$ is determined, and the many-body wave functions $\Psi_i(\mathbf{r}_1, \mathbf{r}_2, \dots, \mathbf{r}_N)$ are then theoretically determined. As a result, the ground-state energy of the system can be viewed as a functional of the electron density. This energy functional in Hohenberg and Kohn's approach is

$$E_{HK} = T[n] + V[n] + E_{int}[n] + U, \quad (3.2)$$

where $T[n]$ is the kinetic energy of the electrons, $V[n]$ is the electron-nuclear interaction energy, $E_{int}[n]$ is the electron-electron interaction and U is the nuclear-nuclear interaction. Thus, the ground-state electron density determines all properties of the system, and it can be checked self-consistently with $\Psi_0(\mathbf{r}_1, \mathbf{r}_2, \dots, \mathbf{r}_N)$. Moreover, the second Hohenberg-Kohn theorem proves that the ground-state density minimizes the total electronic energy of the system. In other words, if an electron density functional other than the *true* ground-state density is used in the energy functional, the resulting energy is higher than the true ground-state energy of the system.

In practice, the Hohenberg-Kohn theorems are not often used to directly make calculations, as the exact form for the density functional is unknown to us. Instead, the most common strategy employed is through the Kohn-Sham method. The ansatz of Kohn and Sham [24] assumes that the exact ground-state density of the original interacting system is equal to that of some chosen auxiliary non-interacting system. The Kohn-Sham equations,

$$\left[-\frac{1}{2}\nabla^2 + \hat{V}^{eff}(\mathbf{r})\right]\psi_i = \epsilon_i\psi_i, \quad (3.3)$$

are the Schrödinger equations for this auxiliary non-interacting system, where $\hat{V}^{eff}(\mathbf{r})$ is the effective potential in which the fictitious non-interacting particles are moving. In principle, Kohn and Sham map the many-body strongly interacting electrons in a static external potential onto that of a single particle moving in an effective potential. The density of the auxiliary system is given by sums of modulus squares of the orbitals which the non-interacting electrons occupy. For the ground-state of the system with N electrons, the electron density of the auxiliary system is

$$n(\mathbf{r}) = \sum_i |\psi_i(\mathbf{r})|^2, \quad (3.4)$$

where the sum is up to the highest occupied orbital. The effective potential includes the external potential and the effects of the Coulomb interactions between the electrons.

The Kohn-Sham equations 3.3 must be solved self-consistently so that the occupied electronic states generate a charge density that produces the electronic potential that was used to construct the equations. Usually one starts with an initial guess for the electron density $n(\mathbf{r})$, then one can calculate the corresponding V^{eff} and solve the Kohn-Sham equations for the ψ_i . From these one calculates a new density¹ and starts again. This procedure is then repeated until convergence is reached.

3.2 APPROXIMATIONS FOR EXCHANGE-CORRELATION ENERGY

The Kohn-Sham ground-state energy functional can be written as

$$E_{KS} = T_s[n] + E_{Hartree}[n] + V[n] + U + E_{xc}[n], \quad (3.5)$$

¹In practice, generating the input density for the $(i+1)^{th}$ iteration is more complicated than merely using the density produced from the orbitals calculated in the i^{th} iteration. Many so called “mixing schemes” have been used over the years. However, for brevity, I will not discuss their detailed background in this dissertation.

where the Hartree energy $E_{Hartree}$ is the classic mean-field Coulomb interaction energy, defined as

$$E_{Hartree}[n] = \frac{1}{2} \int d^3r d^3r' \frac{n(\mathbf{r})n(\mathbf{r}')}{|\mathbf{r} - \mathbf{r}'|}, \quad (3.6)$$

and comparing with the Hohenberg-Kohn functional 3.2, we have

$$E_{xc}[n] = E_{int}[n] - E_{Hartree}[n] + T[n] - T_s. \quad (3.7)$$

$E_{xc}[n]$, named exchange-correlation energy, is just the difference of the internal electronic interactions and the kinetic energies of the true interacting many-body system from those of the independent particles in the Kohn-Sham system. It describes the effects of the Pauli exclusion principle and the difference of the exact energy from the energy of uncorrelated states. The difficult many-body terms in equation 3.1 are incorporated into $E_{xc}[n]$.

Possessing the exact exchange-correlation potential means that we can solve the many-body problem exactly. However, the major shortcoming of DFT is that the exact functional for the exchange-correlation energy is not known except for rare cases. Good approximate expressions for the exchange-correlation energy are used to allow the calculation of certain physical quantities quite accurately. One approximate method of describing the exchange-correlation energy is the local-density approximation (LDA). The exchange-correlation energy can be written as:

$$E_{xc}[n] = \int d^3r n(\mathbf{r})\epsilon_{xc}[n(\mathbf{r})], \quad (3.8)$$

where ϵ_{xc} is the exchange-correlation energy per electron at a point \mathbf{r} . In the local-density approximation, the exchange-correlation energy per electron at a point \mathbf{r} in the inhomogeneous electron gas is equal to the exchange-correlation energy per electron in a homogeneous electron gas that has the same density as the inhomogeneous electron gas at point \mathbf{r} . The exchange-correlation energy of the homogeneous gas can be obtained with great accuracy using quantum Monte Carlo simulation [43–45]. The local-density approximation assumes that the exchange-correlation energy

functional is purely local. So the only information needed is the exchange-correlation energy of the homogeneous gas as a function of density.

Although the LDA is very successful for a large variety of problems, it ignores corrections to the exchange-correlation energy at a point \mathbf{r} due to nearby inhomogeneity in the electron density. Another method widely used is the generalized gradient approximation (GGA). The exchange-correlation energy is approximated by the form

$$E_{xc}[n] = \int d^3r n(r) \epsilon_{xc}[n(r), \nabla n(r), r], \quad (3.9)$$

thus including local density gradient information, as well. It has been demonstrated that GGA gives good atomic ground-state energies [46, 47]. In comparison with LDA, GGA, by including gradient corrections, tends to describe density inhomogeneity better than LDA. It improves the accuracy of the dissociation energies and bond-lengths of small molecules [48], often significantly. Although GGA corrects some deficiencies of the LDA, sometimes it overcorrects the LDA prediction [49].

3.3 PLANE-WAVE BASIS SET AND K-POINT SAMPLING IN PERIODIC CELLS

In principle, the Kohn-Sham single-particle wave functions [50] may be represented in terms of any complete basis set. In my calculations, I use a well-converged plane-wave basis set, as it facilitates evaluation of various terms in the Hamiltonian through fast Fourier transforms, allows for straightforward truncation and systematic convergence through the plane-wave cutoff energy, and permits the efficient calculation of Hellman-Feynman [51, 52] forces without a Pulay correction term [43].

In a periodic system, the Kohn-Sham eigenfunctions can be written using Bloch's Theorem [53]

$$\psi_{i,\mathbf{k}}(\mathbf{r}) = e^{i(\mathbf{k}\cdot\mathbf{r})} u_{i,\mathbf{k}}(\mathbf{r}), \quad (3.10)$$

where $u_{i,\mathbf{k}}(\mathbf{r})$ is a cell-periodic term, and the range of \mathbf{k} can be restricted to one primitive cell of the reciprocal lattice, which usually is chosen to be the Brillouin zone. As the periodic $u_{i,\mathbf{k}}(\mathbf{r})$ can be Fourier transformed to a sum using the plane-wave basis set with wave vectors that are reciprocal lattice vectors indexed by \mathbf{G} , the electronic wave functions at a \mathbf{k} -point in the Brillouin zone are written in the form as

$$\psi_{i,\mathbf{k}}(\mathbf{r}) = \sum_{\mathbf{G}} c_{i,\mathbf{k}}(\mathbf{G}) e^{i(\mathbf{G}+\mathbf{k})\cdot\mathbf{r}} \quad (3.11)$$

When a plane-wave basis set is used, the Kohn-Sham equation 3.3 is expressed as

$$\left[\frac{1}{2} |\mathbf{k} + \mathbf{G}|^2 \delta_{\mathbf{G}\mathbf{G}'} + V_{ext}(\mathbf{G} - \mathbf{G}') + V_{Hartree}(\mathbf{G} - \mathbf{G}') + V_{xc}(\mathbf{G} - \mathbf{G}') \right] c_{i,\mathbf{k}}(\mathbf{G}) = \epsilon_i c_{i,\mathbf{k}}(\mathbf{G}). \quad (3.12)$$

In this equation, the various potentials are described in their Fourier transforms and the kinetic energy is diagonal. Certain terms in equation 3.12, such as V_{xc} and the local part of V_{ext} , are more easily evaluated in real space, and this is accomplished using fast Fourier transforms. For non-periodic systems, like the nanocrystals that I have studied, a periodic simulation-box, named supercell, is used in order to apply Bloch's theorem and permit a plane-wave basis. In the supercell, the molecule is placed in the center, and the size of the unit cell is chosen to be large enough that the molecule and its nearest periodic image do not interact significantly. Periodic boundary conditions are applied to the supercell. Thus, we can test the convergence by increasing the volume of the supercell to isolate the molecule ever further until physical quantities of interest no longer change by a significant amount.

Using a plane-wave basis set, the solution of equation 3.12 is to diagonalize the Hamiltonian matrix which is indexed by $\mathbf{k} + \mathbf{G}$. In principle, an infinite number of plane wave functions indexed with \mathbf{G} on an infinite number of \mathbf{k} -points in the Brillouin zone should be calculated. But two efforts can be made to reduce the computational effort. First, for \mathbf{k} -points that are very close together, the wave functions

will be almost identical. So it is possible to represent the electronic wave functions over a region of \mathbf{k} -space by the wave functions at a single \mathbf{k} -point. We can choose only a finite grid of \mathbf{k} -points on the Brillouin zone. Second, for a given \mathbf{k} -point, the coefficient $c_{i,\mathbf{k}}(\mathbf{G})$ for the plane waves of high \mathbf{G} value, which corresponds to large kinetic energy $\frac{1}{2}(\mathbf{k} + \mathbf{G})^2$ and high resolution in real space, will be close to zero. So we can choose some particular cutoff energy to make a finite plane-wave basis set. The above two efforts change the problem of calculating an uncountably infinite number of continuous electronic wave functions to one of calculating a finite number of electronic plane-wave coefficients at a finite number of \mathbf{k} -points. It is always possible to reduce the magnitude of the resulting error by using denser \mathbf{k} -points and increasing the cutoff energy, until results are satisfactorily converged.

3.4 PSEUDOPOTENTIALS

Physically, the valence electrons interact more strongly between atoms than the core electrons, and the core electrons on different atoms are almost independent of the environment surrounding the atom. It therefore seems reasonable to freeze the core electrons in their atomic configuration and not have to re-compute the core states each time. This “frozen core” approximation is implemented by replacing the nucleus and core electrons with a so-called “pseudo-ion-core”, which interacts with the remaining valence electrons by a “pseudopotential” designed to mimic the correct core-valence interactions over a wide range of conditions. Thus, only the valence electrons are included explicitly in the calculations.

A good pseudopotential can further save the computational effort. In the full nuclear potential, the valence wave functions oscillate rapidly at the region of the core electrons and the nucleus, due to the strong potential and the orthogonality condition between different states. As a matter of fact, this will lead to a very large cutoff

energy and a large plane wave basis set, too large to do realistic calculations. The rapid oscillations of the wave functions near the cores of the atoms can be removed if we use a weaker pseudopotential. Then, the electronic wave functions can be expanded using far fewer plane-wave basis functions than would be needed otherwise. Outside the core radius, the norm-conserving condition, which extends the range of transferability of the pseudopotential, requires that each pseudowavefunction used to define the pseudopotential, must match the corresponding true wavefunction, so that the real and pseudo wavefunctions generate the same charge density outside the core.

The pseudopotential is generated through an *ab initio* procedure. First, the real wave functions in a full nuclear potential are calculated for an isolated atom using an all-electron DFT approach. The pseudo valence wave functions are then constructed by modifying the real wave functions in the core region by removing the oscillations, with the norm-conservation constraint enforced. Finally, the pseudopotential, which is the potential having the pseudowavefunctions defined above as its solution, is obtained by inverting the Schrödinger equation. This procedure makes the pseudopotential transferable among a variety of systems. In my calculation, the *ab initio*, norm-conserving pseudopotentials [47, 54, 55] employed maintain good total-energy convergence using a minimum number of plane waves.

CHAPTER 4

PRELIMINARY CONSIDERATIONS AND CALCULATIONS

4.1 CHOICES FOR CALCULATIONS ON Ti-C NANOCRYSTALS

There are two possible choices of $3 \times 3 \times 3$ titanium carbide nanocrystals, as discussed in section 2.2, which both can be viewed as fragments of bulk TiC. $\text{Ti}_{14}\text{C}_{13}$, one possibility of the $3 \times 3 \times 3$ structure, has titanium atoms on its face-center and corner sites and carbon atoms on the body-center and edge-center sites. $\text{Ti}_{13}\text{C}_{14}$, the other possibility, switches the occupation sites of titanium atoms and carbon atoms in $\text{Ti}_{14}\text{C}_{13}$. Interestingly, $\text{Ti}_{14}\text{C}_{13}$ is shown to be highly abundant in the experiments, while $\text{Ti}_{13}\text{C}_{14}$ is not seen at all [1, 26, 35]. One possibility for this disparity is that $\text{Ti}_{13}\text{C}_{14}$ could be mechanically unstable. Another possibility is that, if $\text{Ti}_{13}\text{C}_{14}$ is mechanically stable, it could be weakly metastable, and then competing factors in the experiments may cause $\text{Ti}_{13}\text{C}_{14}$ to dissociate before being detected, or perhaps never even form.

To understand the stability issue of transition-metal carbide nanocrystals, and specifically Ti-C nanocrystals, DFT calculations are performed on the following four systems: $\text{Ti}_{14}\text{C}_{13}$, $\text{Ti}_{13}\text{C}_{14}$, Ti_6C_{13} and Ti_{13}C_6 . As shown in figure 4.1, if we take away eight corner titanium atoms of $\text{Ti}_{14}\text{C}_{13}$ and eight carbon atoms of $\text{Ti}_{13}\text{C}_{14}$, we obtain the corresponding truncated nanocrystals Ti_6C_{13} and Ti_{13}C_6 , respectively. The choice of these systems in the preliminary considerations is based on the idea that a comparison of the truncated nanocrystals, Ti_6C_{13} and Ti_{13}C_6 , with the ideal nanocrystals, $\text{Ti}_{14}\text{C}_{13}$ and $\text{Ti}_{13}\text{C}_{14}$, gives us a picture of the role of the corner atoms

in these cubic nanocrystals. This can help us understand the stability of atoms at the corner sites, the strength of the corner bonds, and the reason that only one type of $3 \times 3 \times 3$ nanocrystal, $\text{Ti}_{14}\text{C}_{13}$, is seen in the experiments.

To calculate the atomization energy, the energy to fully dissociate a nanocrystal into individual atoms, DFT calculations for an isolated carbon atom and an isolated titanium atom are also performed. The theoretical work to understand the energetic properties of these titanium carbide nanocrystals will be presented in the next chapter.

4.2 CONVERGENCE TESTING AND COMMON PARAMETERS

As discussed in chapter 3, several approximations are made in the DFT calculations. Most of the approximations are controllable, as we can systematically vary the parameters of the computation to achieve convergence. Thus, convergence testing is essential for choosing suitable parameters and achieving a good balance between computation time and computational accuracy.

For all four nanocrystal species, many convergence parameters for the DFT calculations are set to be the same. We use ab initio, highly transferable, optimized norm-conserving pseudopotentials [55] to describe the ion-core interaction with valence electrons. The pseudopotentials are generated to be optimally convergent for a plane-wave basis with a 50 Ry cutoff energy. For the carbon atom, the $2s$ and $2p$ orbitals both participate in chemical bonding, whereas the $1s$ orbital is generally inert to the chemical environment. For the titanium atom, it has been shown that including $3p$ “semi-core” states in the valence manifold, in addition to the $3d$ and $4s$ states, is essential to avoid sizable errors. To be cautious, I also include $3s$ electrons as valence electrons. The inclusion of $3s$ and $3p$ as valence states increases the accuracy significantly with reasonable computational cost. Hence, the carbon atom is treated with

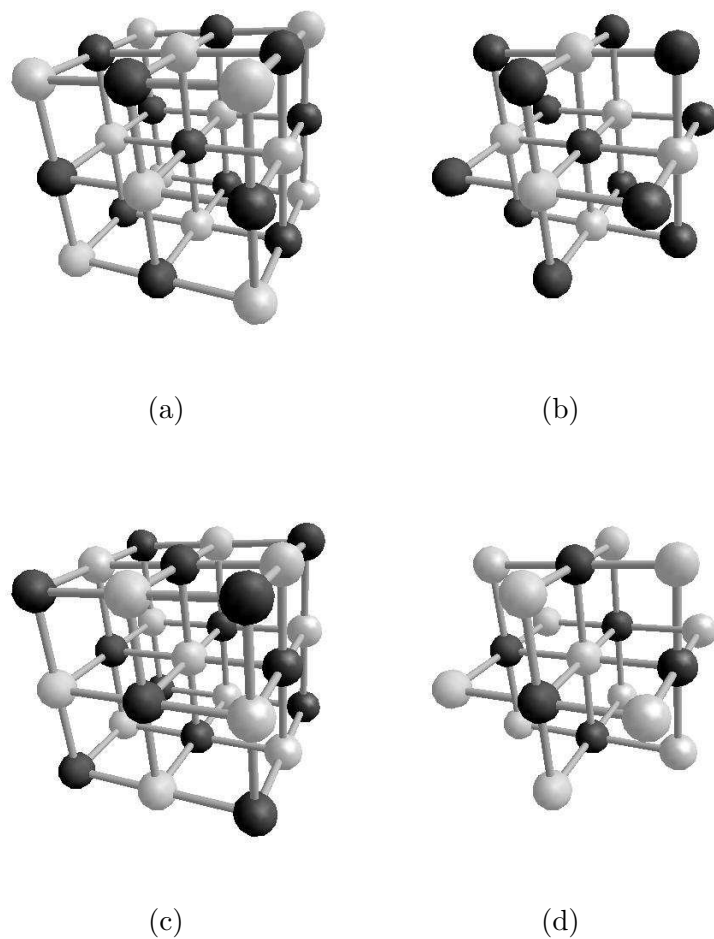


Figure 4.1: Titanium carbide nanocrystal species selected for calculations.

(a) $\text{Ti}_{14}\text{C}_{13}$.

(b) Ti_6C_{13} .

(c) $\text{Ti}_{13}\text{C}_{14}$.

(d) Ti_{13}C_6 .

4 valence electrons, and the titanium atom is treated with 12 valence electrons. The calculations are well converged for a 50 Ry plane-wave cutoff, resulting in a basis set of about 44,000 plane waves to represent the Kohn-Sham single-particle wave functions.

The size of the supercell for the nanocrystals is set big enough to be well converged, giving nearly zero interaction between a nanocrystal system and its nearest periodic images. As the periodic supercell is very large, the Brillouin zone is very small, and the wave functions at different points of the Brillouin zone are very similar. Thus, we achieve good convergence by sampling only the (0,0,0) \mathbf{k} -point (Γ point) in the Brillouin zone. Energy levels are broadened into Gaussians of 0.05 eV to speed up the numerical convergence. The detailed parameters for the DFT calculations of the TiC nanocrystals are shown in Table 4.1. These parameters are used for all four nanocrystal systems and the isolated titanium and carbon atoms. Furthermore, the DFT exchange and correlation energies for all calculations are treated with the generalized gradient approximation (GGA) of Perdew et al. [49].

As the nanocrystals can be viewed as fragments of bulk TiC, all four systems of nanocrystals are assumed to have O_h point symmetry, and the linear dimension is about 4 Å. (Calculations on bulk TiC are presented and discussed in the next section.) The convergence tests shows that a (10.28 Å)³ supercell is sufficiently large to make interactions between nearest periodic images negligible, as there is about 6 Å of intervening vacuum.

4.3 BULK Ti-C CALCULATIONS

There are several purposes for the DFT calculation of bulk TiC. First, as the experimental data for the bulk TiC structure is known, the comparison between experimental and calculated data helps confirm the accuracy of the pseudopotentials used

Table 4.1: Computational parameters for TiC nanosystems and single atoms.

Exchange and correlation energy	GGA [49]
k -point	(0,0,0)/(Γ point)
cutoff energy	50 Ry
Total energy tolerance	$1e^{-5}$ eV
Energy level broadening	0.05 eV
symmetries	O_h
supercell	$10.28 \times 10.28 \times 10.28$ (\AA) ³
Pseudopotentials	Optimized norm-conserving pseudopotentials [55]
Reciprocal lattice	$90 \times 90 \times 90$
Plane wave basis set	~ 44000 plane waves

in the DFT calculations. Second, the initial atomic configuration of the nanocrystal systems will be drawn from the bulk lattice and then relaxed to equilibrium. Third, the length of the Ti-C bonds in the nanocrystals will be compared to the bulk Ti-C bond length in later chapters.

As we know, TiC bulk has the same fcc crystal structure as rocksalt, NaCl. Titanium atoms and carbon atoms sit on alternating sites of a simple cubic lattice. The calculation for bulk TiC uses a **k**-point grid comprising 28 irreducible points, which is well converged, as tests show. We compute the dependence of the total energy of the system on the primitive cell vector length of the fcc lattice, as shown in Figure 4.2. Fitting with a third-order polynomial function, we find the total energy is minimized when the primitive cell vector is 3.077 \AA . The primitive cell vector is $\sqrt{2}L_{TiC}$, where L_{TiC} is the nearest-neighbor Ti-C distance. This distance is computed to be 2.176 \AA , which differs from the experimental value (2.16 \AA) [56] by 0.7%. This level of agreement in structural parameters is typical for GGA-based DFT calculations.

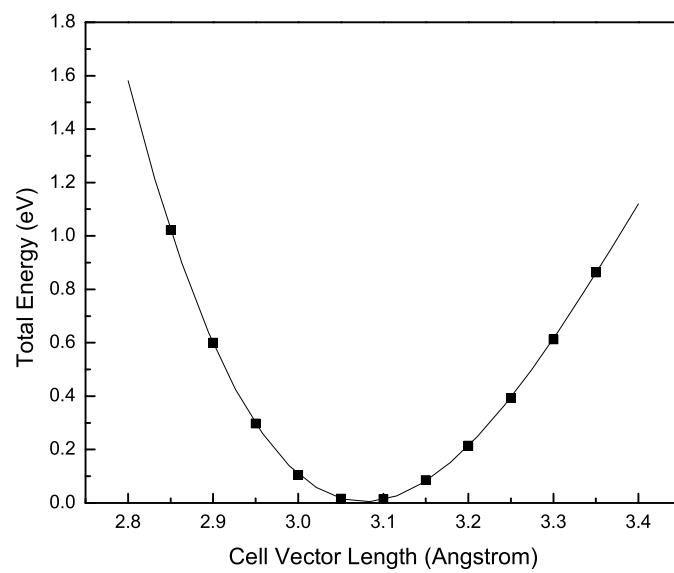


Figure 4.2: Bulk TiC total energy vs. cell vector length.

CHAPTER 5

STRUCTURE AND ENERGETICS

5.1 RELAXED STRUCTURE

In my DFT calculations, the $3 \times 3 \times 3$ nanocrystals $\text{Ti}_{14}\text{C}_{13}$ and $\text{Ti}_{13}\text{C}_{14}$ are set to have the symmetry of the O_h group, which contains 48 symmetry operations. Because of symmetry, there are only three distinct types of nearest-neighbor bonds, including 6 bonds (BF bonds) between the body-center atom and the face-center atoms, 24 bonds (FE bonds) between the face-center and the edge-center atoms, and 24 bonds (EC bonds) between the edge-center and the corner atoms. In the similar DFT calculations done for Ti_6C_{13} and Ti_{13}C_6 , as eight corner atoms are removed, only BF and FE bonds are present. The relaxed structures of the above four nano systems are shown in figure 5.1. Their bond-lengths are reported in Table 5.1, as percent changes relative to the Ti-C bond-length of bulk TiC. Given the overall structure and the O_h symmetry, specifying the BF, FE and EC bond-lengths uniquely determines the structure.

We can see that in $\text{Ti}_{14}\text{C}_{13}$ and $\text{Ti}_{13}\text{C}_{14}$, all bonds are shorter than the bond in TiC bulk, except for the bond from body-center to face-center in $\text{Ti}_{13}\text{C}_{14}$, which is only slightly longer. The change in bond-length is related to the environment in which the atoms reside. In bulk TiC, every atom is surrounded in every direction by neighbors, but in the nanocrystal, the removal of surrounding material causes the shortening of the bond-lengths. From the table, we can also see the role of the corner atoms. For both $\text{Ti}_{14}\text{C}_{13}$ and $\text{Ti}_{13}\text{C}_{14}$, if we remove the corner atoms, leaving Ti_6C_{13}

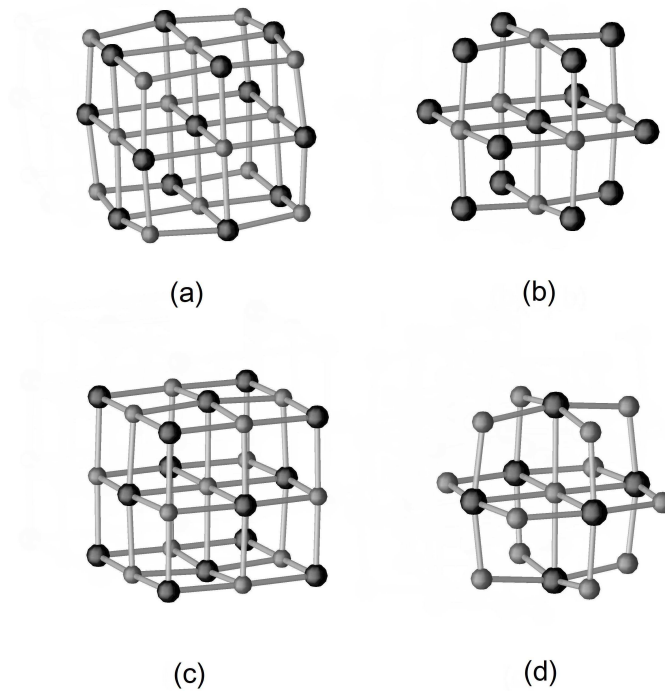


Figure 5.1: Four relaxed Ti-C nanocrystal species. Large dark-grey spheres indicate the positions of the carbon atoms and small light-grey spheres indicate the positions of titanium atoms.

- (a) $\text{Ti}_{14}\text{C}_{13}$.
- (b) Ti_6C_{13} .
- (c) $\text{Ti}_{13}\text{C}_{14}$.
- (d) Ti_{13}C_6 .

Table 5.1: Relaxed structure for $\text{Ti}_{14}\text{C}_{13}$, $\text{Ti}_{13}\text{C}_{14}$, Ti_6C_{13} and Ti_{13}C_6 . Bond-lengths are calculated as percentage differences to 2.176 \AA , the calculated Ti-C bond-length of TiC bulk:

Bond type	$\text{Ti}_{14}\text{C}_{13}$	$\text{Ti}_{13}\text{C}_{14}$	Ti_6C_{13}	Ti_{13}C_6
BF	-3.6%	+0.2%	-1.6%	+3.8%
FE	-1.8%	-4.7%	-6.3%	-6.6%
EC	-7.4%	-6.1%	-	-

and Ti_{13}C_6 , the bond-length between the body-center atom to face-center atom (BF bond) is enlarged and the bond-length from the edge-center to the face-center atom (FE bond) is reduced.

5.2 GROUND-STATE ENERGY

The total ground-state energies of $\text{Ti}_{14}\text{C}_{13}$, $\text{Ti}_{13}\text{C}_{14}$, Ti_6C_{13} and Ti_{13}C_6 are obtained at their equilibrium O_h structures. Table 5.2 gives the raw ground-state total energies of the individual titanium and carbon atoms and the nanocrystals. Because of the different stoichiometric compositions, the absolute total energies of the nanocrystals cannot be compared directly. But the atomization energy, which is the energy to break apart the entire system into individual atoms, can be obtained using these raw energies. As there are only Ti-C bonds as the nearest-neighbor bonds, the average energy of Ti-C bonds in each system can be calculated just by dividing its atomization energy by the total number of nearest-neighbor Ti-C bonds. As shown in table 5.3, the average Ti-C bond energies are very similar for $\text{Ti}_{14}\text{C}_{13}$, $\text{Ti}_{13}\text{C}_{14}$, Ti_6C_{13} , but significantly higher for Ti_{13}C_6 , which differs from the other three by $\sim 0.5 \text{ eV}$. In chapter 8.1, I will discuss how this comparison informs us about the relative stability of corner atoms in Ti-C nanocrystals.

Table 5.2: Raw ground-state total energies of the individual titanium and carbon atoms and the nanocrystals.

System	Raw Ground-state Energy (eV)
Ti	-1578.18
C	-145.91
Ti ₁₄ C ₁₃	-24190.07
Ti ₁₃ C ₁₄	-22756.04
Ti ₆ C ₁₃	-11474.78
Ti ₁₃ C ₆	-21516.50

Table 5.3: Average Ti-C bond energy.

	Ti ₁₄ C ₁₃	Ti ₁₃ C ₁₄	Ti ₆ C ₁₃	Ti ₁₃ C ₆
Atomization Energy (eV)	198.68	196.92	108.83	124.68
Number of Ti-C Bonds	54	54	30	30
E_{bond} (eV/bond)	3.68	3.65	3.63	4.16

CHAPTER 6

VIBRATIONAL ANALYSIS

6.1 HARMONIC FORCE-CONSTANT MODEL

A harmonic force-constant model is used in my analysis of the vibrational states of the nanocrystals. In this model, I assume that the forces on the atoms are linearly proportional to the displacement of each atom away from its equilibrium position. In the real system, the interatomic forces are not exactly linearly proportional to the displacements in the atomic degrees of freedom. But as the displacements are small, the error caused by ignoring anharmonicity is also fairly small. Of course, anharmonicities become physically important at high temperatures, but we can still learn a lot by focusing on the harmonic regime.

To obtain the vibrational modes, I first need to calculate a force-constant matrix. For cubic nanocrystals such as $\text{Ti}_{14}\text{C}_{13}$ and $\text{Ti}_{13}\text{C}_{14}$, Cartesian coordinates are the most convenient to use, with the x , y , and z directions parallel to the three body-to-face-center axes. In the following discussion, I number each atom in the nanocrystal, and by convention set the generalized coordinates q_1, q_2, q_3 to be the x, y, z displacement of atom 1 from its equilibrium position; q_4, q_5, q_6 to be the x, y, z displacement of atom 2 from its equilibrium position; and so on. Correspondingly, the forces on atom 1 in the x, y, z direction are F_1, F_2, F_3 , respectively; the forces on atom 2 in the x, y, z direction are F_4, F_5, F_6 , respectively; and so on. Then in the harmonic

force-constant model, we have

$$\begin{pmatrix} F_1 \\ F_2 \\ \vdots \\ F_{3N} \end{pmatrix} = - \begin{pmatrix} K_{11} & K_{12} & \cdots & K_{1,3N} \\ K_{21} & K_{22} & \cdots & K_{2,3N} \\ \vdots & \vdots & \cdots & \vdots \\ K_{3N,1} & K_{3N,2} & \cdots & K_{3N,3N} \end{pmatrix} \begin{pmatrix} \Delta q_1 \\ \Delta q_2 \\ \vdots \\ \Delta q_{3N} \end{pmatrix}, \quad (6.1)$$

where the matrix $\{K_{i,j}\}$ is a $3N \times 3N$ force-constant matrix for a system with N atoms, as each atom has three degrees of freedom.

The values of the force-constant matrix elements can be obtained through a series of DFT calculations. Using the Hellman-Feynman theorem, we can compute the forces on all atoms due to the perturbation of each atom in turn from its equilibrium position. Each column in the force-constant matrix represents the force on each atomic degree of freedom due to one unit displacement of the atomic degree of freedom corresponding to the given column. So for an ideal system within the harmonic limit, the entire force-constant matrix can be obtained column-by-column by doing DFT calculations on a series of perturbations of different amplitude for each atom in turn, and then computing the best linear fit of the resulting forces on each atomic degree of freedom. Thus, if there are N atoms in the system, $3N$ displacements may be required to obtain the entire force-constant matrix, if only one perturbation amplitude per degree of freedom is used. In general, several amplitudes are used for fitting. However, we can take advantage of the symmetry of the system to reduce the number of displacements. For example, for the $3 \times 3 \times 3$ nanocrystals like $\text{Ti}_{14}\text{C}_{13}$ or $\text{Ti}_{13}\text{C}_{14}$, there are only four groups of atoms, including 1 body-center atom, 6 face-center atoms, 12 edge-center atoms and 8 corner atoms. The columns of the force-constant matrix corresponding to the atoms in the same group are equivalent if point-group rotational operations are applied. In practice, for the $3 \times 3 \times 3$ nanocrystals with O_h symmetry, I only perturb four atoms in the Cartesian directions: the center atom (0,0,0); the face-center atom in the positive x direction (1,0,0);

the edge-center atom (1,1,0); and the corner atom (1,1,1). In addition, the x, y, z displacements of one atom may also be equivalent under a symmetry operation. For example, if we know the forces due to displacing the body-center atom in the +x direction, under symmetry operations, we also know the forces if that atom is displaced in the -x direction, the $\pm y$ direction, and the $\pm z$ direction. Note that positive displacements and negative displacements along a coordinate axis for other atoms are not necessarily equivalent by symmetry. In my calculation of the $3 \times 3 \times 3$ systems, 9 atomic degrees of freedom need to be perturbed to obtain enough information to complete the force-constant matrix. They are the body-center atoms (0,0,0) in the +x direction, the face-center atom (1,0,0) in the $\pm x$ direction and the +y direction, the edge-center atom (1,1,0) in the $\pm x$ direction and the +z direction, and the corner atom (1,1,1) in the $\pm x$ direction.

The force-constant matrix must preserve several important properties. First, it is a symmetric matrix, because

$$K_{ij} = \frac{\partial^2 E}{\partial q_i \partial q_j} = \frac{\partial^2 E}{\partial q_j \partial q_i} = K_{ji},$$

where E is the total energy. Second, because of the point-group symmetry, we have the commutation relationship

$$K \hat{R}_s = \hat{R}_s K,$$

where \hat{R}_s is the $3N \times 3N$ matrix representation of a symmetry operation of the point group. The O_h group, to which $\text{Ti}_{14}\text{C}_{13}$ and $\text{Ti}_{13}\text{C}_{14}$ belongs, has 48 symmetry operations, including rotations, inversion and reflections. Each symmetry matrix \hat{R}_s is constructed in such a way that if it multiplies a unit displacement of one atomic degree of freedom, it results in a unit displacement on another atomic degree of freedom according to the corresponding symmetry operation. So in each $3N \times 3N$ matrix \hat{R}_s for the O_h symmetry operations, each column and row contains exactly one "1", and all other entries are zero. After we apply the above constraints, we find

that among $6,561(=81^2)$ force-constant matrix elements for $\text{Ti}_{14}\text{C}_{13}$ or $\text{Ti}_{13}\text{C}_{14}$, only 95 are independent.

In this form of force-constant matrix, three translation modes and three rotation modes are explicitly included and should come out to have zero frequency on solving for the normal modes. Thus, we can further reduce the independent matrix elements by considering the so-called acoustic sum rules. If the columns for the $3N \times 3N$ force-constant matrix $\{K_{i,j}\}$ are ordered as in equation 6.1, the equations for the acoustic sum rules are

$$\sum_{j=0}^{N-1} K_{i,3j+1} = 0$$

$$\sum_{j=0}^{N-1} K_{i,3j+2} = 0$$

$$\sum_{j=0}^{N-1} K_{i,3j+3} = 0$$

for $i = 0..3N$.

The above three set of equations, along with equation 6.1, actually state that, if all atoms have the same displacement along the x, y, or z direction (or any direction, in fact), the total force on the system should be zero. If we use these equations as constraints, there will be no forces on the atoms if the system is in pure translation. In other words, the acoustic sum rules guarantee that the frequencies for the three linearly independent translation modes are zero. We can further extend the sum rules to account for pure rotations and thus get three linearly independent rotational modes with zero frequency. If all atoms rigidly rotate about any axis, the force-constant matrix should have the property that the total torque on the system is zero. If we do not constrain the force-constant matrix to account for the translational and rotational acoustic sum rules, there will be 6 frequencies that are not exactly zero, but close to zero for translation and rotation. After adding these constraints to the force-constant fitting procedure, the six lowest frequencies are exactly zero. The

acoustic sum rules for the force-constant matrix are also a check on the precision of the harmonic force-constant model and the importance of numerical errors. The effects on the force-constant matrix should be very small, and they are on the order of 1% of the largest force constant in my calculation.

In summary, the system is perturbed on the limited number of independent atomic degrees of freedom, and DFT calculations are performed for each in turn to get the Hellman-Feynman forces due to the perturbation. Then several constraints, such as the symmetry of the force-constant matrix, its commutation with the symmetry operation matrices, and the acoustic sum rules, are enforced as constraints to obtain the entire force-constant matrix K .

6.2 NORMAL MODES OF VIBRATION

After we obtain the $3N \times 3N$ force-constant matrix K , the $3N$ normal modes $|\mathbf{x}_i\rangle$ with frequencies ω_i can be obtained by solving the problem of small oscillations [57]. This involves solving a generalized eigenvalue problem in the matrix form

$$(K - M\omega^2)|\mathbf{x}\rangle = 0,$$

where M is a diagonal $3N \times 3N$ mass matrix. If the columns of the force-constant matrix K are ordered as in equation 6.1, the first three diagonal elements of M are the mass of the first atom, followed by the mass of the second in the next three diagonal positions, and so on. As the force-constant matrix has been fitted using the constraints discussed in the last section, the resulting $3N$ eigenmodes contain 6 translation and rotation modes with zero frequency and $3N - 6$ vibrational modes. If the system is mechanically stable, the $3N - 6$ vibrational modes all have real frequencies, i.e., $\omega^2 > 0$. Otherwise, some of the vibrations will have imaginary frequency. With the calculated normal-mode frequencies, we can plot the vibrational

density of states, where the relative intensity is proportional to the degeneracy of the corresponding vibrational frequency.

Using the method stated in the last section, the normal modes for $\text{Ti}_{14}\text{C}_{13}$ and $\text{Ti}_{13}\text{C}_{14}$ and the truncated Ti_{13}C_6 and Ti_6C_{13} are calculated, and the ordered frequencies are listed in tables 6.1– 6.4, respectively. The results show that the frequencies are all real for $\text{Ti}_{14}\text{C}_{13}$, $\text{Ti}_{13}\text{C}_{14}$ and Ti_{13}C_6 . But there are a few imaginary frequencies in Ti_6C_{13} . This indicates that Ti_6C_{13} is not mechanically stable. This is perhaps not surprising as this species is not observed at all in the experiments. In these tables, I also list the symmetry labels for the corresponding vibrations. From group theory, we know that the calculated eigenmodes must belong to one of the specific irreducible representations of the symmetry group to which the system belongs [58]. The four nanocrystals we calculated are all assumed to have O_h symmetry, as stated previously. Thus, the vibrational modes all belong to one of the irreducible representations of the O_h group. To obtain the symmetry label, or equivalently the irreducible representation, for a given non-degenerate mode or set of degenerate modes, the character numbers for the symmetry operation \hat{R}_s of the O_h group are calculated for that mode or set of modes and then compared with the corresponding value in the group character table. The character number for the symmetry operations in the subspace spanned by modes $\{|\mathbf{x}_j \rangle\}$, with degeneracy d , is given by:

$$\chi(\hat{R}_s) = \sum_{j=1}^d \langle \mathbf{x}_j | M \hat{R}_s | \mathbf{x}_j \rangle,$$

where M is the mass matrix. In the symmetry labels shown in the tables, A represents a nondegenerate mode, E represents a two-fold degenerate mode, and T represents a three-fold degenerate mode.

Atomic-displacement patterns for the normal modes are visualized using a special tool I developed using Java3D. The tool is introduced in Appendix A. Different atoms can be assigned different colors for spheres with different diameters. For example,

in the following figures, large dark grey spheres represent the carbon atoms, and small light grey spheres represent the titanium atoms. To visualize the vibration in the static image, an arrow through a sphere is used to point in the direction of the corresponding atomic displacement. The length of the arrow is proportional to the relative magnitude of the atomic displacement in the vibrations. In multimedia presentations, the modes can be shown in real-time animations, instead of being represented by static arrows.

The visualization of the atomic-displacement patterns can help us understand the nature of the vibrations and give us useful information on the properties of the system. For example, by visualizing the imaginary modes of Ti_6C_{13} , as shown in figure 6.1, we find that the imaginary modes always involve motion of edge atoms. This indicates that the carbon atom is not stable at the edge-center sites for Ti_6C_{13} . More discussion on the stability of corner atoms of $\text{Ti}_{14}\text{C}_{13}$ and $\text{Ti}_{13}\text{C}_{14}$, with the aid of the visualization tool, will be presented in section 8.2.

6.3 DENSITY OF STATES AND IR SPECTRUM

We can plot the vibrational density of states with the calculated $3N - 6$ vibrational frequencies. In order to facilitate comparisons with finite-resolution experimental data, the lines of vibrational levels are broadened by convoluting with a Gaussian. Thus, the broadened vibrational density of states at frequency f is given by:

$$I(f) = \frac{1}{\sigma\sqrt{2\pi}} \sum_{j=1}^{3N-6} e^{-\frac{(f-f_j)^2}{2\sigma^2}},$$

where σ is the broadening width in the convolution. Figures 6.2 and 6.3 show the vibrational density of states for $\text{Ti}_{14}\text{C}_{13}$ and $\text{Ti}_{13}\text{C}_{14}$, respectively. In these figures, the lower panel shows separate vibrational densities of states for infrared-active modes, Raman-active modes and other modes. Infrared-active modes dynamically generate oscillating dipole moments that couple to light. For the O_h symmetry group,

Table 6.1: Vibrational modes for $\text{Ti}_{14}\text{C}_{13}$.

Frequency (cm^{-1})	Symmetry	Frequency (cm^{-1})	Symmetry	Frequency (cm^{-1})	Symmetry
155	E_u	326	A_{1g}	489	T_{1u}
194	T_{2g}	340	T_{2u}	509	E_g
200	T_{1u}	365	A_{2g}	526	A_{1g}
204	T_{2u}	368	T_{2g}	563	T_{1g}
232	T_{2g}	383	A_{1g}	574	E_u
246	E_g	399	T_{2u}	667	T_{1u}
254	A_{2u}	415	T_{1g}	680	T_{1u}
267	E_g	417	T_{1u}	745	T_{2g}
290	T_{1g}	424	E_g	789	A_{2u}
297	T_{1u}	483	T_{2g}		
326	T_{1u}	483	T_{2u}		

Table 6.2: Vibrational modes for $\text{Ti}_{13}\text{C}_{14}$.

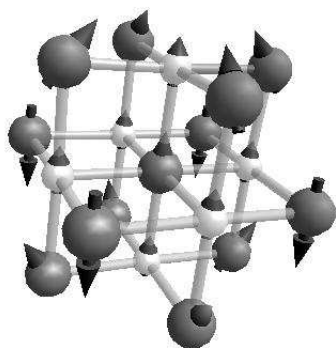
Frequency (cm^{-1})	Symmetry	Frequency (cm^{-1})	Symmetry	Frequency (cm^{-1})	Symmetry
168	E_u	340	A_{1g}	554	E_g
193	T_{2u}	356	E_g	560	T_{2g}
195	T_{2g}	390	T_{1u}	574	A_{2u}
209	A_{2g}	420	T_{1u}	576	T_{1u}
221	E_g	427	E_g	619	A_{1g}
239	T_{1u}	455	T_{2g}	646	T_{1g}
276	T_{2u}	457	E_u	698	T_{2u}
280	T_{1g}	471	T_{1g}	702	T_{1u}
294	A_{2u}	481	T_{2u}	729	T_{2g}
298	T_{2g}	484	T_{1u}		
303	T_{1u}	508	A_{1g}		

Table 6.3: Vibrational modes for Ti_{13}C_6 .

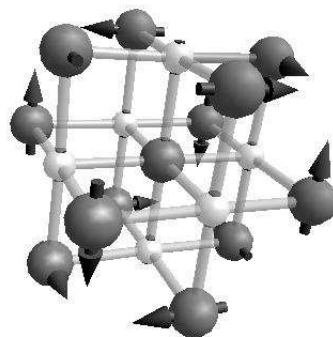
Frequency (cm^{-1})	Symmetry	Frequency (cm^{-1})	Symmetry	Frequency (cm^{-1})	Symmetry
54	E_u	198	E_g	392	E_g
113	T_{1g}	217	A_{2g}	440	T_{1u}
118	T_{2u}	233	T_{2u}	448	A_{1g}
134	T_{2g}	249	T_{1u}	647	T_{1g}
142	T_{1u}	288	A_{1g}	682	T_{2u}
172	T_{2g}	301	E_g	696	T_{1u}
184	A_{2u}	303	T_{1u}	708	T_{2g}

Table 6.4: Vibrational modes for Ti_6C_{13} .

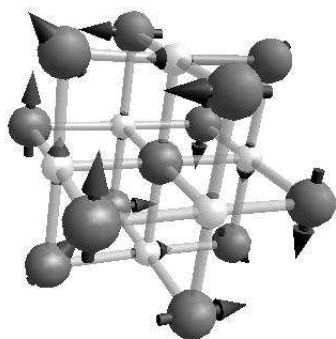
Frequency (cm^{-1})	Symmetry	Frequency (cm^{-1})	Symmetry	Frequency (cm^{-1})	Symmetry
381i	T_{1u}	110	T_{2g}	461	T_{1u}
363i	A_{2u}	125	T_{1u}	485	A_{2g}
354i	T_{2g}	356	A_{1g}	525	E_g
212i	E_u	371	T_{2u}	560	T_{2g}
181i	T_{1g}	417	T_{1u}	560	T_{1g}
159i	T_{2u}	426	T_{2u}	589	T_{1u}
92	E_g	456	E_g	613	A_{1g}



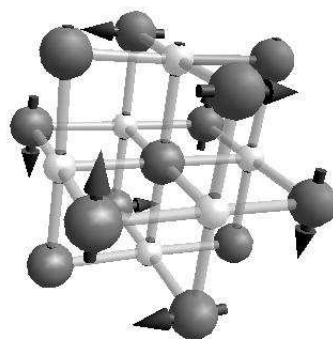
(a)



(b)



(c)



(d)

Figure 6.1: First four imaginary vibrational levels for Ti_6C_{13} (Refer to table 6.4).

(a) T_{1u} symmetry.

(b) A_{2u} symmetry.

(c) T_{2g} symmetry.

(d) E_u symmetry.

dynamic dipole moments can only be generated by vibrations with T_{1u} symmetry. So after assigning symmetry labels, one can deduce which modes are infrared-active. Similarly, the Raman-active modes belong to either T_{2g} , A_{1g} or E_g symmetry.

The infrared-active modes are experimentally observable. The induced dipole in a molecule can act as a radiator [34], and the intensity of infrared absorption for a given mode is proportional to the magnitude of the derivative of the dipole moment with respect to the vibration amplitude of the normal modes. The overall infrared spectrum is obtained, then, by including the dipole derivative magnitude as a weighting factor for each infrared-active mode in the expression for the infrared vibrational density of states. After figuring out which modes are dipole active, we can displace the atoms from their equilibrium position according to the pattern of the vibrational mode and perform a DFT calculation to obtain the new total charge distribution, including electronic and core charges. Since the unperturbed nanocrystals in this study have no dipole moment, the dipole moment of the distorted structure, divided by the distortion amplitude, is the finite-difference approximation to the dipole derivative.

The convoluted IR spectrum of $Ti_{14}C_{13}$ is shown in figure 6.4. The vibrational patterns of the atoms for the modes corresponding to the two major peaks in the IR spectrum are visualized in figure 6.5. For each case, I only show one of the three degenerate modes in T_{1u} symmetry, and omit the other two rotational versions to save space. The mode at frequency 489 cm^{-1} , corresponding to the highest peak in the IR spectrum, is shown in figure 6.5(a). In this mode, the carbon atoms on the top layer and the bottom layer vibrate in the same direction mainly perpendicular to the surface, but with slight in-plane “breathing” motion. Also, one can see that the four carbon atoms surrounding the middle layer move in the opposite direction to the motion of the carbon atoms on the top and bottom layers, and their vibrations are perfectly perpendicular to the middle layer because of the symmetry required

by the T_{1u} mode. The vibrations of other atoms are relatively weaker in this mode. The mode, corresponding to the second highest peak of the IR spectrum, is shown in figure 6.5(b). In this mode, the relative vibration of the carbon atoms in the middle plane, excluding the body-center carbon atom, are much stronger than that of other atoms. In comparison with those in the vibrational mode of the first peak, the relative vibrational amplitude of carbon atoms on the top and bottom layers are much smaller in this higher frequency mode.

The calculated IR spectrum can be compared with the experimental data [35, 36], as shown in figure 6.4. The overall agreement with experiment on frequencies and relative intensities is quite good. Several small peaks at low frequency are out of the experimental range. The peak at frequency 489 cm^{-1} matches the more intense IR peak in the experimental data, 485 cm^{-1} . The second strong peak in the calculations is at 667 cm^{-1} , and the experimental frequency for the second peak is 630 cm^{-1} . This small deviation from experiment results in part from approximations in the calculations, such as finite differences in estimating force constants, excluding anharmonic effects, etc. In addition, differences between theory and experiment arise from the fact that the experimental spectra result from multi-phonon processes, and thus may not accurately reflect the linear vibrational spectrum. Therefore, the overall agreement in peak frequencies is quite good. The relative intensities of the two major peaks are quite comparable with the experimental data, as well.

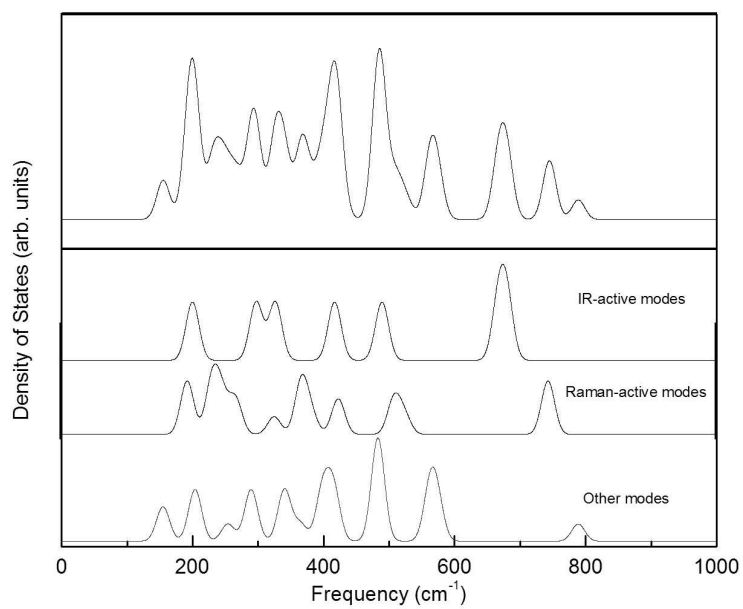


Figure 6.2: Vibrational density of states for Ti₁₄C₁₃ (upper panel), and the separation into different types of modes (lower panel). Gaussian convolution broadening width is 10 cm⁻¹.

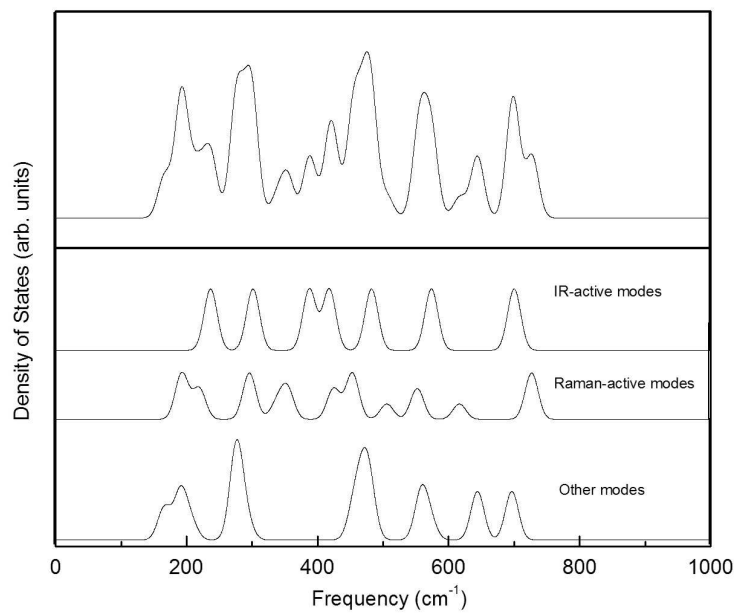


Figure 6.3: Vibrational density of states for Ti₁₃C₁₄ (upper panel), and the separation into different types of modes (lower panel). Gaussian convolution broadening width is 10 cm⁻¹.

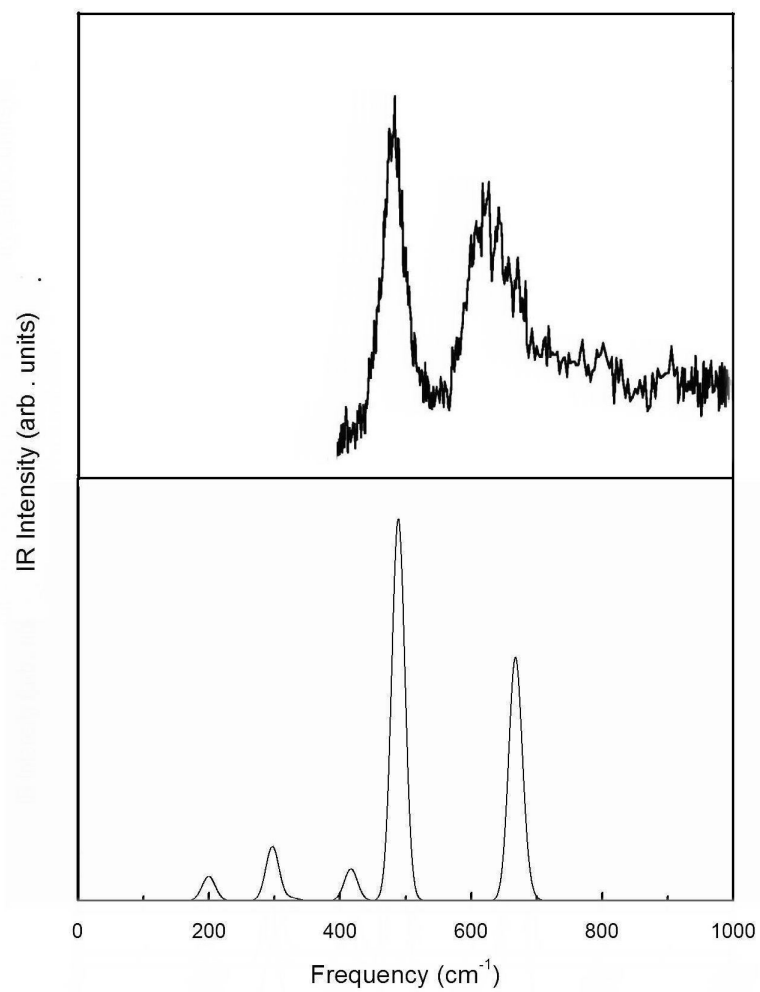


Figure 6.4: Comparison between the experimental spectrum and calculated IR spectrum for $\text{Ti}_{14}\text{C}_{13}$. The upper panel shows the experimental spectrum from ref. [35]. The lower panel shows the calculated spectrum with a Gaussian convolution width 10 cm^{-1} .

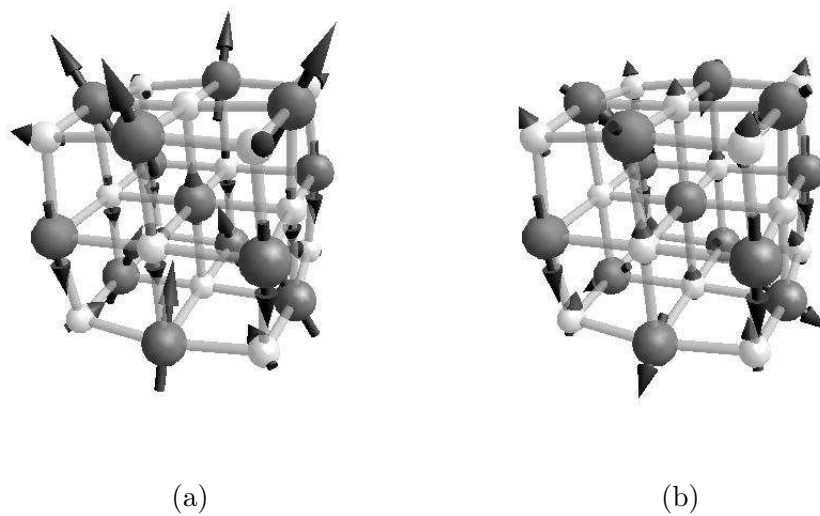


Figure 6.5: Vibrations in IR-active modes of $\text{Ti}_{14}\text{C}_{13}$.
(a) Generating the highest peak (489 cm^{-1}) in the IR spectrum.
(b) Generating the second highest peak (667 cm^{-1}) in the IR spectrum.

CHAPTER 7

ELECTRONIC STRUCTURE ANALYSIS

7.1 ELECTRONIC ORBITALS

As discussed in chapter 3, pseudopotentials are chosen to use because the core electrons do not experience substantial modification relative to isolated atoms. In my calculations, four electrons in the $2s$ and $2p$ atomic orbitals of carbon and twelve electrons in the $3s$, $3p$, $3d$ and $4s$ atomic orbitals of titanium are treated as valence electrons and considered as participating in the chemical bonding. So in total, $\text{Ti}_{14}\text{C}_{13}$ contains 220 valence electrons occupying ~ 110 molecular orbitals, and $\text{Ti}_{13}\text{C}_{14}$ contains 8 electrons fewer than $\text{Ti}_{14}\text{C}_{13}$ occupying ~ 106 molecular orbitals.

Just like the vibrational modes, the molecular orbitals of $\text{Ti}_{14}\text{C}_{13}$ and $\text{Ti}_{13}\text{C}_{14}$ also transform according to irreducible representations of the O_h symmetry group. The symmetry label of each orbital, or, more precisely, each degenerate orbital manifold, is determined using a similar method to that used to obtain the symmetry labels for vibrational modes. For symmetry operation \hat{R}_i , the $\alpha\beta$ element of its matrix representation in the degenerate subspace expanded by $\{\psi_1, \psi_2, \dots, \psi_n\}$ is calculated as

$$\int \psi_\alpha^*(\mathbf{r}) \hat{R}_i \psi_\beta(\mathbf{r}) d\mathbf{r}^3. \quad (7.1)$$

We only need to calculate the trace of this matrix,

$$\sum_{\alpha=1}^n \int \psi_\alpha^*(\mathbf{r}) \hat{R}_i \psi_\alpha(\mathbf{r}) d\mathbf{r}^3, \quad (7.2)$$

as this is just the character number χ_i for \hat{R}_i in this subspace. Then we can compare the results with the character table of the O_h group, and determine the symmetries for all orbitals. Table 7.1 shows the symmetry labels and energies for all the occupied orbitals and a few unoccupied orbitals for $\text{Ti}_{14}\text{C}_{13}$. The energies are relative the highest occupied molecular orbital (HOMO). Thus the energy of the HOMO is set to zero, and the next higher energy level is the lowest unoccupied molecular orbital (LUMO). Table 7.2 shows the results for its sibling species, $\text{Ti}_{13}\text{C}_{14}$, for comparison.

7.2 VISUALIZATION OF WAVE FUNCTIONS

Although the symmetries of the wave functions are obtained in the last section, visualization of the wave function can help us better understand the formation of molecular bonds. The electronic wave functions generated by the electronic structure codes are generally complex, but because of time reversal invariance, it is always possible to perform a unitary transformation on the wave functions to make them real, for easier visualization.

For a non-degenerate wave function, it is possible simply to multiply by an overall complex phase coefficient to make it real [59]. For degenerate complex wave functions, we obtain a basis of real wave functions in the degenerate subspace by the following procedure. Suppose the original degenerate complex wave functions are $\psi_i(r)$ with $i=1..n$, and the real wave functions are $\phi_j(r)$ with $j=1..n$. We would like to find a unitary matrix $C = \{c_{ij}\}$ such that

$$\phi_j(r) = \sum_i \psi_i(r)c_{ij}. \quad (7.3)$$

In the spin unpolarized multielectronic system, we have time reversal symmetry, such that

$$\psi_j^*(r) = \hat{T}\psi_j(r) = \sum_i \psi_i(r)t_{ij}, \quad (7.4)$$

Table 7.1: Kohn-Sham orbitals for $\text{Ti}_{14}\text{C}_{13}$.

Index	Symmetry	Energy (eV)	Index	Symmetry	Energy (eV)
1	a_{1g}	-55.976	59–61	t_{1u}	-9.661
2–4	t_{1u}	-55.948	62–63	e_g	-9.329
5–7	t_{2g}	-55.937	64–66	t_{2u}	-8.882
8	a_{2u}	-55.937	67–69	t_{2g}	-8.819
9	a_{1g}	-55.862	70–72	t_{1u}	-4.198
10–12	t_{1u}	-55.850	73	a_{2u}	-3.823
13–14	e_g	-55.842	74–75	e_g	-3.135
15–17	t_{2g}	-33.380	76	a_{1g}	-3.112
18–20	t_{1u}	-33.375	77–79	t_{2g}	-3.086
21	a_{1g}	-33.328	80–82	t_{1u}	-2.826
22	a_{2u}	-33.267	83–84	e_u	-2.285
23	a_{1g}	-33.247	85–87	t_{2g}	-2.254
24–26	t_{1u}	-33.099	88–90	t_{1u}	-2.079
27–29	t_{2u}	-33.076	91–93	t_{1g}	-2.067
30–32	t_{2g}	-33.021	94–96	t_{2u}	-2.065
33–35	t_{1g}	-33.007	97–98	e_g	-1.867
36–37	e_g	-32.992	99–101	t_{1g}	-1.743
38–40	t_{1u}	-32.955	102–104	t_{1u}	-1.581
41–42	e_u	-32.950	105–105	a_{2g}	-1.317
43–44	e_g	-32.948	106–108	t_{2u}	-1.258
45–47	t_{2g}	-32.819	109–111(HOMO)	t_{2g}	0.000
48–50	t_{1u}	-32.793	112(LUMO)	a_{1g}	0.094
51–53	t_{2u}	-32.760	113	a_{2u}	0.191
54–56	t_{1g}	-32.737	114–115	e_u	0.244
57	a_{1g}	-10.977	116–118	t_{1u}	0.750
58	a_{1g}	-9.708	119–120	e_g	0.820

Table 7.2: Kohn-Sham orbitals for $\text{Ti}_{13}\text{C}_{14}$.

Index	Symmetry	Energy (eV)	Index	Symmetry	Energy (eV)
1	a_{1g}	-56.369	57–58	e_g	-9.743
2	a_{1g}	-55.934	59	a_{1g}	-9.315
3–5	t_{1u}	-55.915	60–62	t_{1u}	-8.909
6–8	t_{2g}	-55.891	63–65	t_{2g}	-8.664
9–10	e_g	-55.869	66	a_{2u}	-7.928
11–13	t_{2u}	-55.869	67	a_{1g}	-4.198
14–16	t_{1u}	-33.585	68–70	t_{2g}	-4.020
17	a_{1g}	-33.330	71–73	t_{1u}	-3.427
18–20	t_{2g}	-33.208	74–76	t_{2u}	-3.291
21–22	e_g	-33.199	77–78	e_g	-2.798
23–25	t_{1u}	-33.153	79–81	t_{1g}	-2.720
26–28	t_{2u}	-33.132	82	a_{2u}	-2.278
29–31	t_{1u}	-33.116	83–85	t_{1u}	-2.227
32–34	t_{1g}	-33.049	86–88	t_{2g}	-2.201
35–36	e_g	-33.029	89–91	t_{2u}	-1.812
37	a_{2u}	-33.006	92–93	e_g	-1.778
38–40	t_{2u}	-32.952	94–96	t_{1u}	-1.702
41	a_{2g}	-32.899	97–98	e_u	-1.572
42–44	t_{2g}	-32.864	99–101	t_{2g}	-1.499
45–47	t_{1u}	-32.728	102	a_{1g}	-1.099
48–49	e_u	-32.643	103–105	t_{1g}	-0.653
50–52	t_{1g}	-32.625	106–108(HOMO)	t_{1u}	0.000
53–53	a_{1g}	-11.084	109–111(LUMO)	t_{2g}	0.238
54–56	t_{1u}	-9.996	112–113	e_g	0.827

where the matrix of $\hat{T}, \{t_{ij}\}$, is symmetric and unitary. As $\phi_j(r)$ is a real wave function, we have

$$\phi_j(r) = \phi_j^*(r). \quad (7.5)$$

With equation 7.3-7.5, we can derive that

$$\sum_k \psi_k(r) c_{kj} = \sum_{ik} \psi_k(r) t_{ki} c_{ij}^*, \quad (7.6)$$

and we can get

$$c_{kj} = \sum_i t_{ki} c_{ij}^*, \quad (7.7)$$

or in matrix form

$$C = TC^*. \quad (7.8)$$

Using $CC^\dagger = 1$, we have

$$CC^T = T. \quad (7.9)$$

As T is unitary and symmetric, we can always find matrix P and D such that

$$T = PDP^T, \quad (7.10)$$

where D is a diagonal matrix. Finally we get the matrix

$$C = PD^{\frac{1}{2}} \quad (7.11)$$

to transform the degenerate basis from complex wave functions to real wave functions.

After we get the real wave functions, we can plot their isosurfaces. In this dissertation, black and white colors are just used to give the phase information, indicating whether the isosurface of the real wave function is positive or negative.

7.3 ANALYSIS OF MOLECULAR ORBITAL ENERGY LEVEL DIAGRAMS

The Kohn-Sham orbital energy diagrams of $\text{Ti}_{14}\text{C}_{13}$ and $\text{Ti}_{13}\text{C}_{14}$ are shown in figure 7.1– 7.2. There are four energy regions for the molecular orbitals. Region I is around

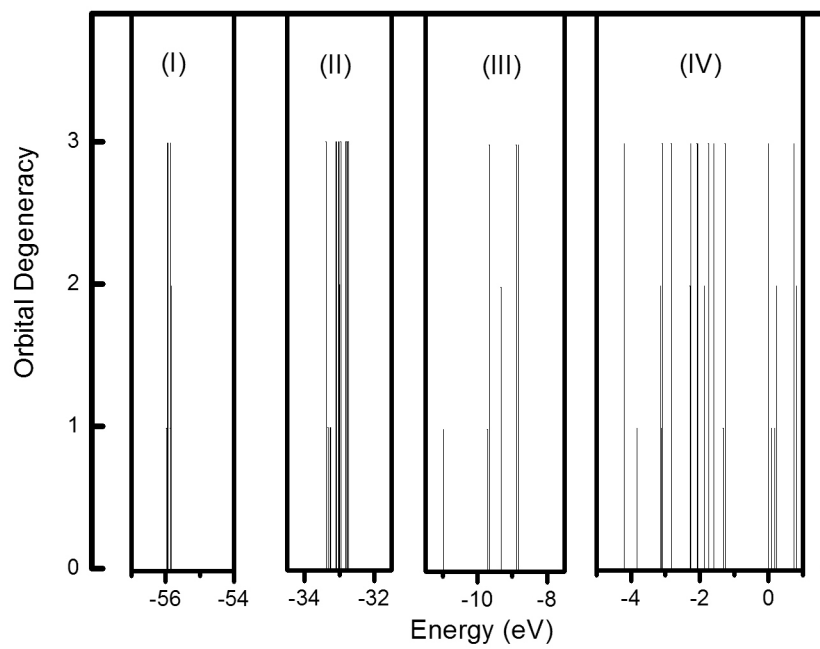


Figure 7.1: Kohn-Sham energy level diagram of $\text{Ti}_{14}\text{C}_{13}$.

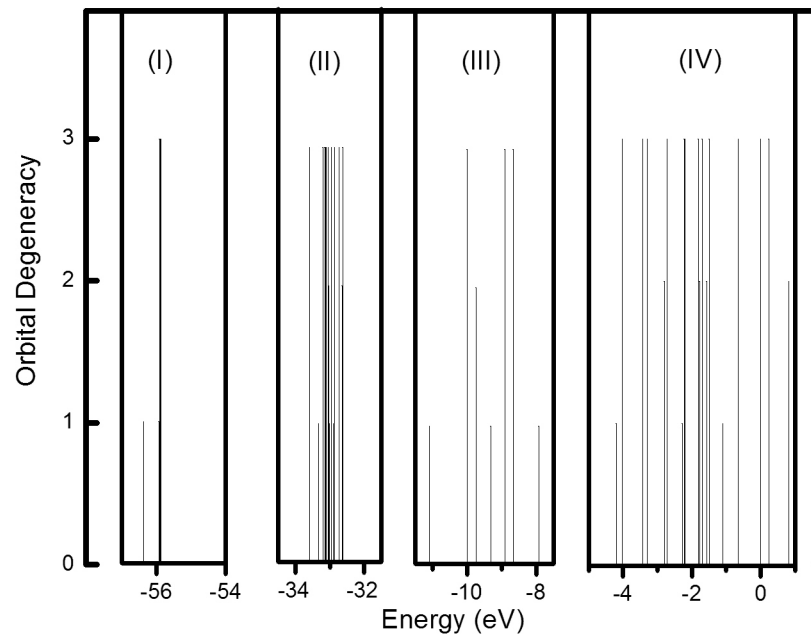


Figure 7.2: Kohn-Sham energy level diagram of $\text{Ti}_{13}\text{C}_{14}$.

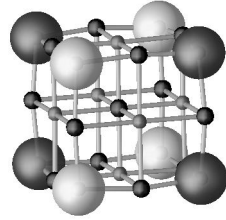
-56 eV; region II is around 33 eV; Region III is about -11~8 eV; and region IV is higher than -5 eV. By visualizing these molecular orbitals, one finds that large gaps among the energy bands are mainly due to their relationship with the atomic orbitals from which they arise.

To give a better illustration, some example molecular orbitals of $\text{Ti}_{14}\text{C}_{13}$ in different regions are shown in figure 7.3–7.6. To save space, only one representative orbital from each degenerate set is shown in these figures. For example, we will only show orbital 5 and not its degenerate partners, orbital 6 and orbital 7.

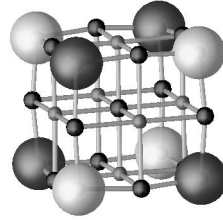
The molecular orbitals of $\text{Ti}_{14}\text{C}_{13}$ in region I, as shown in figure 7.3, are formed primarily by $3s$ atomic orbitals of titanium. The $3s$ orbitals of face-center and corner titanium atoms may have different contributions. For example, orbitals 5~8 are primarily formed by $3s$ orbitals of the corner titanium atom and orbitals 10~13 are primarily formed by $3s$ orbitals of the face-center titanium atoms.

Some molecular orbitals of $\text{Ti}_{14}\text{C}_{13}$ in region II, as shown in figure 7.4, are formed primarily by $3p$ atomic orbitals of titanium. The different directions of these p orbitals reflect the symmetry of the corresponding molecular orbitals. In region III, as shown in figure 7.5, the orbitals are formed primarily by $2s$ atomic orbitals of carbon. In this energy region, we can also see a small contribution from atomic p orbitals of titanium.

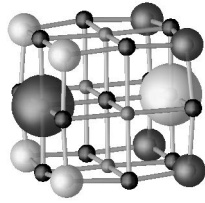
Hybridization of the atomic orbitals in region IV is much stronger than in the lower energy regions. The molecular orbitals in this region are formed primarily by hybridization of carbon $2p$ atomic orbitals and titanium $3d$ atomic orbitals. This region includes the highest occupied molecular orbital (HOMO) and lowest unoccupied molecular orbital (LUMO). The molecular orbitals in region IV are the ones that mainly contribute to the molecular bonding, which we are most interested in. This is further discussed in the next section.



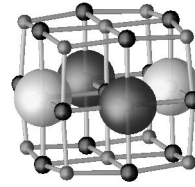
(a) Orbital 5



(b) Orbital 8



(c) Orbital 10



(d) Orbital 13

Figure 7.3: Electron orbitals of $\text{Ti}_{14}\text{C}_{13}$ in region I of orbital energy diagram in figure 7.1. The isosurfaces are plotted for the wave function equals $\pm 0.091 \text{ (\AA)}^{-\frac{3}{2}}$.

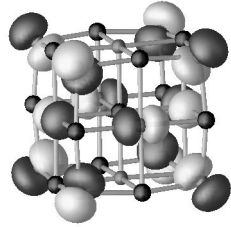
(a) Orbital 5, -55.937 eV, t_{2g} symmetry.

(b) Orbital 8, -55.937 eV, a_{2u} symmetry.

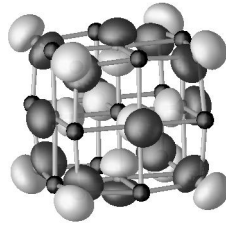
(c) Orbital 10, -55.850 eV, t_{1u} symmetry.

(d) Orbital 13, -55.842 eV, e_g symmetry.

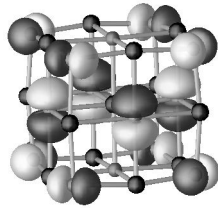
Titanium atoms are indicated by light grey spheres, and carbon atoms are indicated by dark grey spheres. They may not be seen if they are enclosed by the visualized isosurface of the Kohn-Sham orbitals. The black or white color on the isosurface is just used to indicate whether the *real* wave function is positive or negative. This visualization scheme for orbitals is used throughout this dissertation.



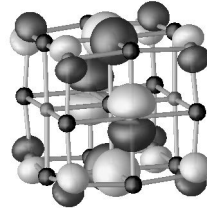
(a) Orbital 15



(b) Orbital 23



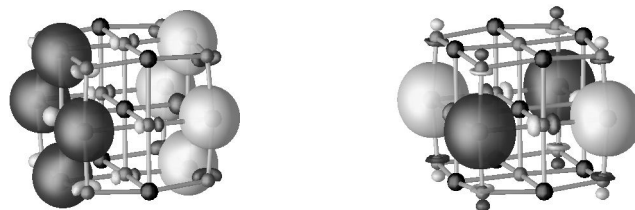
(c) Orbital 51



(d) Orbital 54

Figure 7.4: Electron orbitals of $\text{Ti}_{14}\text{C}_{13}$ in region II of orbital energy diagram in figure 7.2. The isosurfaces are plotted for the wave function equals $\pm 0.091 (\text{\AA})^{-\frac{3}{2}}$.

- (a) Orbital 15, -33.380 eV, t_{2g} symmetry.
- (b) Orbital 23, -33.247 eV, a_{1g} symmetry.
- (c) Orbital 51, -32.760 eV, t_{2u} symmetry.
- (d) Orbital 54, -32.737 eV, t_{1g} symmetry.



(a) Orbital 59

(b) Orbital 67

Figure 7.5: Some orbitals of $\text{Ti}_{14}\text{C}_{13}$ in region III of orbital energy diagram in figure 7.2. The isosurfaces are plotted for the wave function equals $\pm 0.091 \text{ (\AA)}^{-\frac{3}{2}}$.

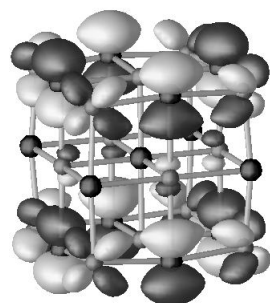
(a) Orbital 59, -9.661 eV, t_{1u} symmetry.

(b) Orbital 67, -8.819 eV, t_{2g} symmetry.

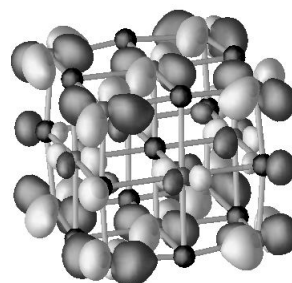
7.4 MOLECULAR BONDING OF $\text{Ti}_{14}\text{C}_{13}$ AND $\text{Ti}_{13}\text{C}_{14}$

To better understand molecular bonding in $\text{Ti}_{14}\text{C}_{13}$ and $\text{Ti}_{13}\text{C}_{14}$, I plot the Kohn-Sham orbitals near in energy to the HOMOs for each species. The rotational versions of degenerate orbitals are omitted to save space. Orbitals near the HOMO and LUMO are labelled with reference to the HOMO and LUMO. For example, in $\text{Ti}_{14}\text{C}_{13}$, orbitals 109–111 are the degenerate HOMOs and orbital 112 is the LUMO. Then the degenerate orbitals 106–108 are named HOMO-1 and the non-degenerate orbital 113 is named LUMO+1.

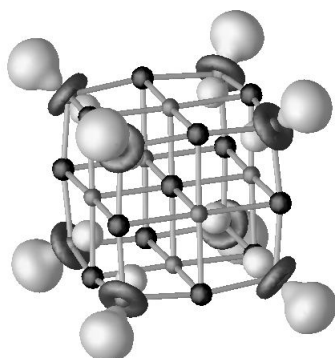
The HOMO, LUMO, HOMO-1 and LUMO+1 of $\text{Ti}_{14}\text{C}_{13}$ are shown in figure 7.6. The HOMO-1, (7.6(a)), has t_{2u} symmetry. It exhibits π -bonding between d_{xy} -like atomic orbitals on the corner titanium atoms and p-like atomic orbitals on the



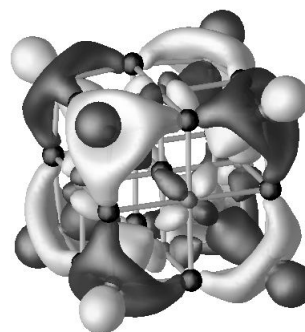
(a) HOMO-1



(b) HOMO



(c) LUMO



(d) LUMO+1

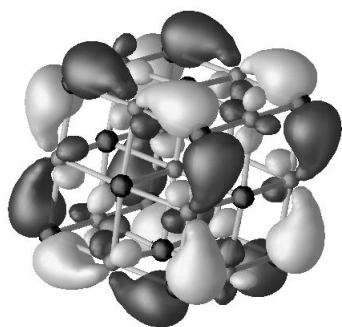
Figure 7.6: HOMO-1, HOMO, LUMO and LUMO+1 of $\text{Ti}_{14}\text{C}_{13}$

(a) HOMO-1, -1.258 eV, t_{2u} symmetry.

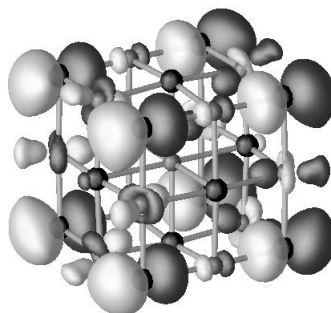
(b) HOMO, 0 eV, t_{2g} symmetry.

(c) LUMO, 0.094 eV, a_{1g} symmetry.

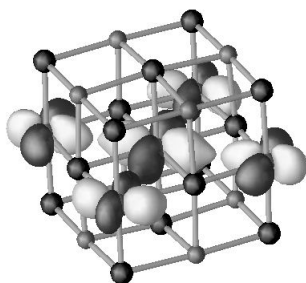
(d) LUMO+1, 0.191 eV, a_{2u} symmetry.



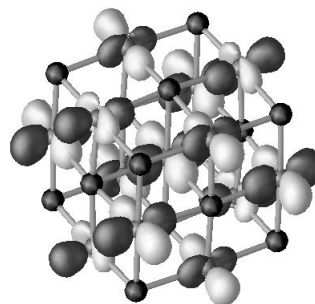
(a) HOMO-1



(b) HOMO



(c) LUMO



(d) LUMO+1

Figure 7.7: HOMO-1, HOMO, LUMO and LUMO+1 of $\text{Ti}_{13}\text{C}_{14}$
(a) HOMO-1, -0.653 eV, t_{1g} symmetry.
(b) HOMO, 0 eV, t_{1u} symmetry.
(c) LUMO, 0.238 eV, t_{2g} symmetry.
(d) LUMO+1, 0.827 eV, e_g symmetry.

edge-center carbon. The HOMO of $\text{Ti}_{14}\text{C}_{13}$, which has t_{2g} symmetry, is primarily constructed from a σ -bonding arrangement of d_{xy} -like atomic orbitals of titanium in the three atomic planes parallel to a given face of the cube. In figure 7.6(b), $dd\sigma$ bonds form between the face-center and corner titanium atoms on the upper and lower faces, and a weaker $dd\sigma$ bonding arrangement is seen in the central plane for face-center titanium atoms. There are also non-bonding atomic p orbitals shown on some edge-center carbon atoms in the middle layer. The LUMO of $\text{Ti}_{14}\text{C}_{13}$ has a_{1g} symmetry. As seen in 7.6(c), it is formed from a non-bonding arrangement of d_{z^2} -like orbitals on the corner titanium atoms, where the local z -axis for each atom is taken to lie along the body diagonal. There is essentially no overlap. The LUMO+1, shown in 7.6(d), is mostly constructed from atomic d_{z^2} -like orbitals on the corner titanium atoms and d_{xy} -like atomic orbitals on the face-center titanium atoms. There is a slight bonding character between the corner atomic orbitals and p -like orbitals at the edge-center carbon atoms.

By comparison, we can see in figure 7.7 that the HOMO-1 of $\text{Ti}_{13}\text{C}_{14}$, with t_{2g} symmetry, only has weak σ -like bonds between atomic p -orbitals of corner carbon and atomic d_{xy} orbitals of edge-center titanium. Moreover, this bonding arrangement appears to be highly strained. The HOMO of $\text{Ti}_{13}\text{C}_{14}$, with t_{1u} symmetry, comprises primarily corner carbon atomic p -orbitals, which are oriented along an edge. Along the same edge appears a small contribution from the atomic p -orbital of the edge-center titanium atom. The corner carbon p -orbitals and edge-center titanium p -orbital are arranged in an anti-bonding σ configuration. A slight contribution from the non-bonding d -like orbitals is seen on the other edge-center titanium atoms. The LUMO of $\text{Ti}_{13}\text{C}_{14}$ has t_{2g} symmetry. The central plane looks similar to the surface layer in the HOMO of $\text{Ti}_{14}\text{C}_{13}$. The d_{xy} atomic orbitals on the edge-center titanium atoms in the central plane form σ bonds with the d_{xy} atomic orbital of the

central titanium atom. The HOMO+1 of $\text{Ti}_{13}\text{C}_{14}$, with T_{2g} symmetry, only shows non-bonded $d_{x^2-y^2}$ atomic orbitals on all titanium atoms.

The nature of the HOMOs, LUMOs, and nearby molecular orbitals of $\text{Ti}_{14}\text{C}_{13}$ and $\text{Ti}_{13}\text{C}_{14}$ has a great impact on the stability of the corner atoms in these two nanocrystals. We will discuss this effect in detail in section 8.4 of the next chapter.

CHAPTER 8

STABILITY OF CORNER CARBON ATOMS

8.1 NEAREST-NEIGHBOR Ti-C BONDING ENERGY

We come back to an issue first mentioned in section 4.1. A large abundance of the nanocrystal $\text{Ti}_{14}\text{C}_{13}$ is seen in the experiments, but its sibling nanocrystal $\text{Ti}_{13}\text{C}_{14}$ is not seen at all. One question this raises is whether $\text{Ti}_{13}\text{C}_{14}$ is intrinsically mechanically stable or not? In the previous vibrational analysis, all vibrational normal-mode frequencies for $\text{Ti}_{13}\text{C}_{14}$ are real. This indicates that $\text{Ti}_{13}\text{C}_{14}$ is mechanically stable in the ground-state. If there are small perturbations of the atoms of $\text{Ti}_{13}\text{C}_{14}$, the atoms will return to their equilibrium positions. So there must be competing factors in the molecular beam, as the clusters are condensing and equilibrating, that favor $\text{Ti}_{14}\text{C}_{13}$ and prefer to take carbon atoms from corner sites if they land there. One signature validating this hypothesis would be if carbon atoms bond only relatively weakly (compared to titanium) to corner sites of the nanocrystal. In this section, we show an analysis of the energetic properties which lead us to conclude that carbon atoms at corner sites form much weaker bonds to the other atoms of the nanocrystal than when titanium atoms occupy the corner sites. The vibrational and electronic analysis in the subsequent two sections will further confirm this picture.

In chapter 5, we calculated the total energy of the abundant $\text{Ti}_{14}\text{C}_{13}$, the non-existent $\text{Ti}_{13}\text{C}_{14}$, and the corresponding truncated fragments obtained by removing the corner atoms. In all of these four systems, the only nearest-neighbor bonds are Ti-C bonds. So we count the total number of Ti-C bonds for each species and divide its

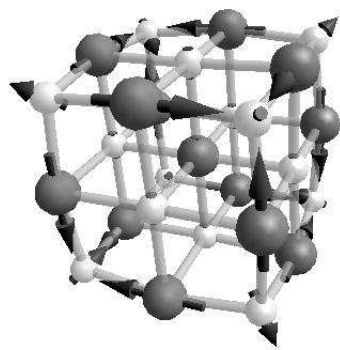
molecular binding energy by this number, to give an average Ti-C bond energy. As shown in table 5.3, if we go from $\text{Ti}_{14}\text{C}_{13}$ to Ti_6C_{13} by removing the corner titanium atoms, the corner Ti-C bonds are all broken, but the average Ti-C bond energy is barely changed. This indicates that the energy of the corner Ti-C bonds of $\text{Ti}_{14}\text{C}_{13}$ is roughly equal to the average Ti-C bond energy of $\text{Ti}_{14}\text{C}_{13}$. For the same analysis for $\text{Ti}_{13}\text{C}_{14}$, if we remove the corner carbon atoms, and thus break all corner Ti-C bonds, the average Ti-C bond energies of Ti_{13}C_6 and $\text{Ti}_{13}\text{C}_{14}$ differ by ~ 0.5 eV *per bond*. This difference is huge given that each Ti-C bond in the full nanocrystal has an average energy of about 3.6 eV. As we know, if we take bonds away from $\text{Ti}_{13}\text{C}_{14}$ and the average bond energy goes up a lot, it suggests that bond energy of the removed bonds must be much lower than the average. This is a somewhat indirect conclusion that the Ti-C bonds to corner carbon atoms in $\text{Ti}_{13}\text{C}_{14}$ are weaker than other Ti-C bonds, which have nearly the same average energy as in $\text{Ti}_{14}\text{C}_{13}$, $\text{Ti}_{13}\text{C}_{14}$ and Ti_6C_{13} . In other words, the corner carbon atoms are weakly bonded in $\text{Ti}_{13}\text{C}_{14}$. Although this is only a comparison in average Ti-C bond energy, and the nearest Ti-C bond in the truncated species should not be considered identical to the corresponding Ti-C bond in the full nanocrystal, the difference is unlikely to be as large as 0.5 eV per bond. So we conclude that the significant increase of average bond energy by removing the corner carbon atoms indicates that the energy of the bonds to these atoms is much lower than average.

8.2 VIBRATIONAL MODES RELATED TO CORNER ATOMS

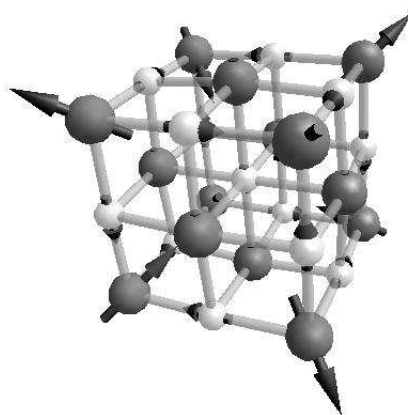
The picture that the bond to the corner carbon atoms is comparatively weak is further strengthened in our vibrational analysis. Just as the vibrational frequency of a ball attached to a soft spring is lower than that of a ball attached to a stiff spring, the vibrational frequency of atoms connected by soft bonds is lower than

that of atoms connected by stiffer bonds. The nanocrystals $\text{Ti}_{14}\text{C}_{13}$ and $\text{Ti}_{13}\text{C}_{14}$ all have 27 atoms and 75 vibrational modes. Because they have similar structures and the same symmetry, the vibrational modes of $\text{Ti}_{14}\text{C}_{13}$ and $\text{Ti}_{13}\text{C}_{14}$ have a one-to-one correspondence, with the same symmetry labels. For example, the highest frequency mode of $\text{Ti}_{14}\text{C}_{13}$ is an A_{2u} mode with frequency 789 cm^{-1} . As shown in figure 8.1(a), this mode mainly activates bonds to corner atoms, and the involvement of other Ti-C bonds is negligible. The corresponding A_{2u} mode in $\text{Ti}_{13}\text{C}_{14}$, shown in figure 8.1(b), has frequency 574 cm^{-1} . This huge red-shift demonstrates the significant softening of the corner bonds in going from $\text{Ti}_{14}\text{C}_{13}$ to $\text{Ti}_{13}\text{C}_{14}$. One may argue that the vibrational frequency is determined by two factors, the bond stiffness and the atomic masses. Indeed, the mass distribution is different in these two systems. But this could not result in such a huge red shift effect. To eliminate the mass effect, we can just artificially switch the mass of titanium atoms and carbon atoms in $\text{Ti}_{14}\text{C}_{13}$ and make the same mass distribution as $\text{Ti}_{13}\text{C}_{14}$. However, even if this mass adjustment is made, a big red-shift of more than 150 cm^{-1} can still be observed for the A_{2u} mode in going from $\text{Ti}_{14}\text{C}_{13}$ to $\text{Ti}_{13}\text{C}_{14}$. So from comparison of the A_{2u} mode of $\text{Ti}_{14}\text{C}_{13}$ and $\text{Ti}_{13}\text{C}_{14}$, we know that the corner bonds of $\text{Ti}_{14}\text{C}_{13}$ are stiffer than those of $\text{Ti}_{13}\text{C}_{14}$.

The stiffness of a bond only reflects the strength of the restoring force on the atoms due to a small perturbation. While the stiffness of a bond does not have to correlate with the strength of the bond, which is the energy to break the bond and take away the connected atoms, there is a general trend in chemical bonds that a stiffer bond is usually a stronger bond. Thus, our vibrational results provide corroborating evidence that the bonds to corner carbon atoms in $\text{Ti}_{13}\text{C}_{14}$ are weaker than the bonds to corner titanium atoms in $\text{Ti}_{14}\text{C}_{13}$.



(a) $\text{Ti}_{14}\text{C}_{13}$



(b) $\text{Ti}_{13}\text{C}_{14}$

Figure 8.1:

(a) A_{2u} mode for $\text{Ti}_{14}\text{C}_{13}$, frequency 789 cm^{-1}

(b) A_{2u} mode for $\text{Ti}_{13}\text{C}_{14}$, frequency 574 cm^{-1}

These A_{2u} modes mainly activate bonds to corner atoms.

8.3 DISPLACEMENT OF CORNER ATOM ALONG BODY DIAGONAL

To follow up on the assertion that a stiffer bond is a stronger bond, DFT total-energy calculations are done for a series of displacements of a corner atom away from its equilibrium position. Figure 8.2 shows the variation of the total energy, relative to that of the equilibrium configuration, as one corner atom is displaced from its equilibrium position along the body diagonal of the cube. In the figure, a positive displacement refers to moving a corner atom outward from the center of the $3 \times 3 \times 3$ cube, and a negative displacement refers to moving a corner atom inward. We can see that near the equilibrium position, the curvature for $\text{Ti}_{14}\text{C}_{13}$ is smaller than that for $\text{Ti}_{13}\text{C}_{14}$. This also indicates that the bonds to the corner carbon atom in $\text{Ti}_{13}\text{C}_{14}$ are softer than those to the corner titanium atom in $\text{Ti}_{14}\text{C}_{13}$, which is the conclusion made in the last section. In the limit of large displacement, each energy curve should asymptote to the dissociation limit for removing the corner atom. If the energy of the equilibrium structure is set to zero for both nanocrystal species, then the difference in corner-atom dissociation energies for $\text{Ti}_{14}\text{C}_{13}$ and $\text{Ti}_{13}\text{C}_{14}$ is just the difference in the two asymptotic limits. In fact, we are more interested in comparing the difference between $\text{Ti}_{14}\text{C}_{13}$ and $\text{Ti}_{13}\text{C}_{14}$ than in obtaining the absolute dissociation energy for each system separately. From the graph, we can see that it requires more energy to remove one corner titanium atom from $\text{Ti}_{14}\text{C}_{13}$ than to remove one corner carbon atom in $\text{Ti}_{13}\text{C}_{14}$. The energy difference is approximately 2 eV. Thus, the analysis of figure 8.2 confirms the trend mentioned in the last section: that the softer corner carbon bond in $\text{Ti}_{13}\text{C}_{14}$ (compared to the corner titanium bond in $\text{Ti}_{14}\text{C}_{13}$) implies a weaker bond, as well.

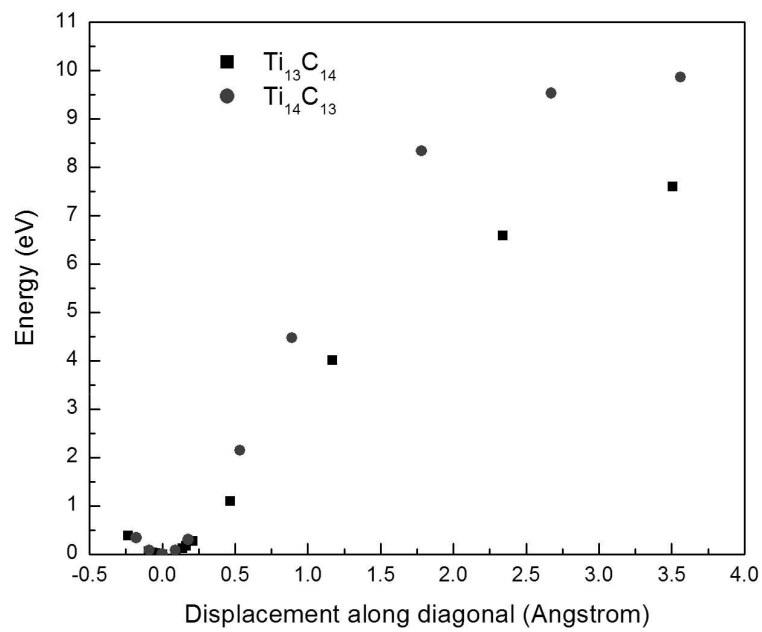


Figure 8.2: Energy variations due to a displacement of one corner atom along the body diagonal of $\text{Ti}_{14}\text{C}_{13}$ and $\text{Ti}_{13}\text{C}_{14}$. The ground-state total energy at the equilibrium structure is set to zero.

8.4 CONNECTION TO THE ELECTRONIC STRUCTURE

To gain a better understanding of the reasons for the differences in bonds to corner carbon atoms in $\text{Ti}_{13}\text{C}_{14}$, from bonds to corner titanium atoms in $\text{Ti}_{14}\text{C}_{13}$, I examine and compare the high-lying filled electronic orbitals for these two systems. Isosurfaces for some of these electronic orbitals of $\text{Ti}_{14}\text{C}_{13}$ and $\text{Ti}_{13}\text{C}_{14}$ were shown in chapter 7. As seen in figure 7.6 and figure 7.7, visualizing the orbitals near the HOMO can give us a clearer picture of the nature of corner-atom bonding. The fact that the molecular orbitals involved most substantially in corner-atom bonding are among the highest in energy of filled orbitals suggests that these atoms are the most susceptible to detachment by any process that causes electronic excitation.

Comparing the HOMOs for $\text{Ti}_{14}\text{C}_{13}$ and $\text{Ti}_{13}\text{C}_{14}$ reveals very distinct bonding interactions. In the former, the HOMO arises primarily from a σ bonding arrangement of atomic d orbitals linking four corner titanium atoms to the face-center titanium of their common face. In contrast, the HOMO of $\text{Ti}_{13}\text{C}_{14}$ emerges from a weak *anti*-bonding interaction of atomic p orbitals on two adjacent corner carbon atoms and an atomic p orbitals on the edge-center titanium atom of their common edge. Thus, analysis of the HOMOs alone already shows the disparity in corner-atom bonding between these two nanocrystal species.

A similar disparity is seen in the HOMO-1 of the two $3 \times 3 \times 3$ nanocrystals. As figure 7.6 shows, the HOMO-1 for $\text{Ti}_{14}\text{C}_{13}$ involves π -like bonding between corner titanium d orbitals and adjacent edge-center carbon p orbitals. The orientational flexibility of the atomic d orbitals permits the formation of this comparatively strong π -like bonding interaction when titanium atoms sit at corner sites. In contrast, the carbon atoms at the corners of $\text{Ti}_{13}\text{C}_{14}$ have no d orbitals. The HOMO-1 in this case, as figure 7.7 shows, is formed primarily from p orbitals on the corner carbons interacting comparatively weakly with d orbitals of adjacent edge-center titanium

atoms. The problem here is that the manifold of p orbitals at the corner site lacks the orientational flexibility to form strong bonds with the neighboring edge-center atoms. Indeed, in most cases when carbon forms covalent bonds to three nearest neighbors, it does so using sp^2 hybrid orbitals which are planar, with 120° bond angles. The corner sites of this cubic nanocrystal are inhospitable to this type of bonding interaction, because the geometry is far from planar and the bond angles are nearly 90° . No electronic arrangement is quite suitable for corner bonds with carbon atoms in the corner sites. As figure 7.7 illustrates, the bonds that *do* form are highly strained electronically, and thus tend to be weak, compared to the corner-titanium case.

CHAPTER 9

ALLOYING EFFECTS ON THE Ti SITES

9.1 POSSIBILITIES OF $\text{Ti}_{14-x}\text{Zr}_x\text{C}_{13}$ NANOCRYSTALS

Up to now, all the experiments related with the transition-metal carbide nanocrystals were done with pure transition metals, like titanium, vanadium, zirconium, etc. I am interested to know what will be the effects if an alloy of transition metals, such as titanium-zirconium, is used in producing the nanocrystal. Starting from $\text{Ti}_{14}\text{C}_{13}$, up to 14 titanium atoms in the $3 \times 3 \times 3$ nanocrystal can be replaced by zirconium atoms. For each alloy concentration x , yielding $\text{Ti}_{14-x}\text{Zr}_x\text{C}_{13}$, there are multiple isomers depending on the distribution of zirconium atoms among the metal sites. For example, there are 14 possible ways to replace one titanium atom with one zirconium atom in $\text{Ti}_{14}\text{C}_{13}$. However, due to symmetry, these 14 possible forms belongs to two distinct categories. Eight of the 14 forms, designated $\text{Ti}_{13}\text{Zr}^{cor}\text{C}_{13}$, has a zirconium atom substituting the titanium atom of $\text{Ti}_{14}\text{C}_{13}$ at a corner cite. The other six of the 14 forms, designated $\text{Ti}_{13}\text{Zr}^{fc}\text{C}_{13}$, replace a titanium atom on a face-center. In this chapter, I will use these two categories of the $x=1$ case of $\text{Ti}_{14-x}\text{Zr}_x\text{C}_{13}$ to study the effects of metal-atom alloying on the properties of cubic metal-carbide nanocrystals. In the analysis, I will highlight both similarities to pure $\text{Ti}_{14}\text{C}_{13}$, and the new features arising from the zirconium alloying as well.

9.2 $\text{Ti}_{13}\text{Zr}^{cor}\text{C}_{13}$

I have treated zirconium with 12 valence electrons per atom, just as we did for titanium. Other DFT computational parameters have also been chosen to be the same as for the $\text{Ti}_{14}\text{C}_{13}$, so I am able to compare the structure of $\text{Ti}_{13}\text{Zr}^{cor}\text{C}_{13}$, with that of $\text{Ti}_{14}\text{C}_{13}$ on an equal footing. The equilibrium positions of the atoms obtained from DFT total energy minimizations are compared to each other in table 9.1. In figure 9.1, it can be seen that the structures of the two nanocrystals are hard to distinguish. Only the Zr-C bonds at the zirconium corner of $\text{Ti}_{13}\text{Zr}^{cor}\text{C}_{13}$ are slightly longer than the corresponding corner Ti-C bonds in $\text{Ti}_{14}\text{C}_{13}$. Other than that, the lengths of the Ti-C bonds are not significantly changed due to the substitution of zirconium for titanium at a corner site.

In order to examine the effect of alloying on the vibrational spectrum, I have used the technique described in chapter 6 to compute the force constant matrix. Using the force constant matrix, I have then calculated the vibrational modes and frequencies. Because one titanium atom in $\text{Ti}_{14}\text{C}_{13}$ is replaced by a zirconium atom, the perfect O_h symmetry of $\text{Ti}_{14}\text{C}_{13}$ is broken. As a result, $\text{Ti}_{13}\text{Zr}^{cor}\text{C}_{13}$ has C_{3v} symmetry. As the C_{3v} point group is a subgroup of the O_h point group, some degenerate levels of $\text{Ti}_{14}\text{C}_{13}$, which is in higher symmetry, will split in $\text{Ti}_{13}\text{Zr}^{cor}\text{C}_{13}$. Thus, there will be more distinct lines in the vibrational spectrum for $\text{Ti}_{13}\text{Zr}^{cor}\text{C}_{13}$ than for $\text{Ti}_{14}\text{C}_{13}$. The decomposition of O_h irreducible representations into direct sums of C_{3v} irreducible representations is shown in table 9.2. This shows how the normal-mode symmetries changed and degenerate levels split as the nanocrystal symmetry is reduced from O_h to C_{3v} . I find that there are 54 vibrational levels for $\text{Ti}_{13}\text{Zr}^{cor}\text{C}_{13}$, including 18 labelled A_1 , 9 labelled A_2 , and 27 labelled E.

Table 9.3 shows the calculated frequencies and corresponding symmetry labels for $\text{Ti}_{13}\text{Zr}^{cor}\text{C}_{13}$ vibrational levels. The vibrational modes transforming like the A_1 or

Table 9.1: Positions of atoms in $\text{Ti}_{13}\text{Zr}^{cor}\text{C}_{13}$ and $\text{Ti}_{14}\text{C}_{13}$. Coordinates are in units of Angstroms.

$\text{Ti}_{13}\text{Zr}^{cor}\text{C}_{13}$				$\text{Ti}_{14}\text{C}_{13}$			
	x	y	z		x	y	z
Zr	2.11	2.11	2.11	Ti	2.01	2.01	2.01
Ti	2.10	0.00	0.00	Ti	2.10	0.00	0.00
	-2.10	-0.01	-0.01		-2.10	0.00	0.00
	0.00	2.10	0.00		0.00	2.10	0.00
	-0.01	-2.10	-0.01		0.00	-2.10	0.00
	0.00	0.00	2.10		0.00	0.00	2.10
	-0.01	-0.01	-2.10		0.00	0.00	-2.10
	-2.03	2.00	2.00		-2.01	2.01	2.01
	2.00	-2.03	2.00		2.01	-2.01	2.01
	2.00	2.00	-2.03		2.01	2.01	-2.01
	-2.01	-2.01	2.00		-2.01	-2.01	2.01
	2.00	-2.01	-2.01		2.01	-2.01	-2.01
	-2.01	2.00	-2.01		-2.01	2.01	-2.01
	-2.01	-2.01	-2.01		-2.01	-2.01	-2.01
C	0.00	0.00	0.00	C	0.00	0.00	0.00
	2.14	2.14	-0.02		2.14	2.14	0.00
	-2.13	2.14	0.00		-2.14	2.14	0.00
	2.14	-2.13	0.00		2.14	-2.14	0.00
	-2.14	-2.14	0.00		-2.14	-2.14	0.00
	-0.02	2.14	2.14		0.00	2.14	2.14
	0.00	-2.13	2.14		0.00	-2.14	2.14
	0.00	2.14	-2.13		0.00	2.14	-2.14
	0.00	-2.14	-2.14		0.00	-2.14	-2.14
	2.14	-0.02	2.14		2.14	0.00	2.14
	-2.13	0.00	2.14		-2.14	0.00	2.14
	2.14	0.00	-2.13		2.14	0.00	-2.14
	-2.14	0.00	-2.14		-2.14	0.00	-2.14

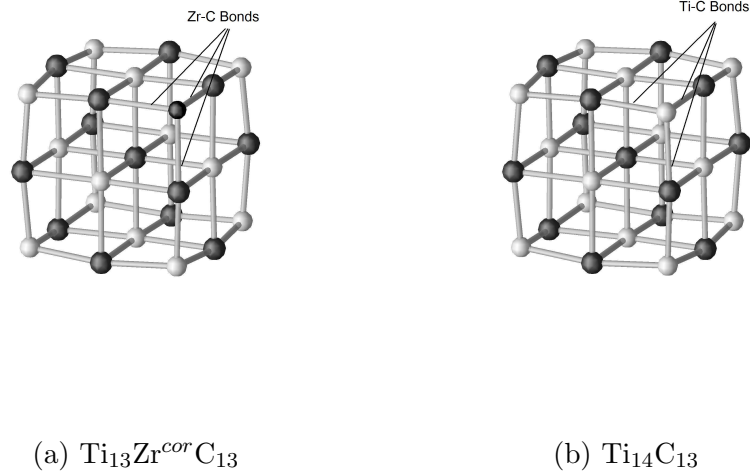


Figure 9.1: Equilibrium structure of $\text{Ti}_{13}\text{Zr}^{cor}\text{C}_{13}$ and $\text{Ti}_{14}\text{C}_{13}$. Zr-C bond in $\text{Ti}_{13}\text{Zr}^{cor}\text{C}_{13}$ is about 6% longer than the corresponding Ti-C bond in $\text{Ti}_{14}\text{C}_{13}$. All ball-and-stick figures in this chapter use the following visualization scheme: The zirconium atom is indicated by a *smaller* and *darker* sphere to distinguish with titanium atoms which are indicated by white spheres and carbon atoms which are indicated by grey spheres.

Table 9.2: Mode splitting from $\text{Ti}_{14}\text{C}_{13}$ (O_h) to $\text{Ti}_{13}\text{Zr}^{cor}\text{C}_{13}$ (C_{3v}). The first column gives the number of the vibrational levels in $\text{Ti}_{14}\text{C}_{13}$ belonging to the corresponding symmetry label.

	$\text{Ti}_{14}\text{C}_{13}$ O_h irreducible representation		splitting for C_{3v} symmetry
3	A_{1g}	→	A_1
0	A_{1u}	→	A_2
1	A_{2g}	→	A_2
2	A_{2u}	→	A_1
4	E_g	→	E
2	E_u	→	E
3	T_{1g}	→	A_2+E
7	T_{1u}	→	A_1+E
5	T_{2g}	→	A_1+E
4	T_{2u}	→	A_2+E

Table 9.3: Normal-mode frequencies and symmetry labels for $\text{Ti}_{13}\text{Zr}^{cor}\text{C}_{13}$.

Frequency (cm^{-1})	Symmetry	Frequency (cm^{-1})	Symmetry	Frequency (cm^{-1})	Symmetry
141	E	329	E	485	A_2
181	A_1	334	A_1	485	E
181	E	339	E	490	A_1
199	E	341	A_2	492	E
202	A_2	363	A_2	510	E
206	E	365	A_1	532	A_1
208	A_1	370	E	562	E
230	A_1	387	A_1	564	A_2
230	E	395	E	573	E
245	E	396	A_2	668	E
247	A_1	409	E	674	A_1
269	E	412	E	682	E
289	A_2	416	A_2	683	A_1
290	E	427	A_1	746	E
295	A_1	439	E	751	A_1
299	E	474	E	793	A_1
323	A_1	481	A_1		

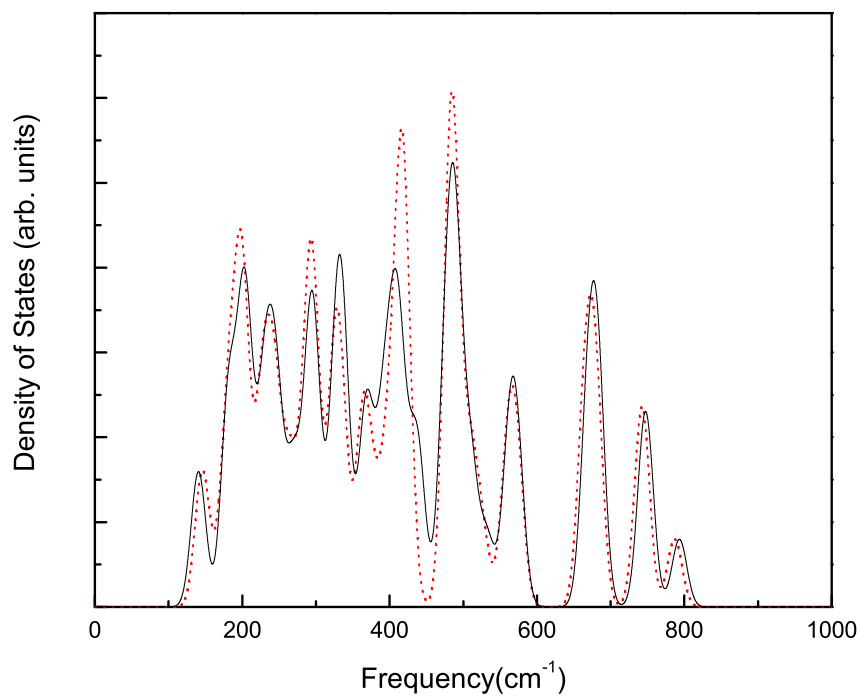


Figure 9.2: IR density of states of $\text{Ti}_{13}\text{Zr}^{cor}\text{C}_{13}$. The solid line is computed with the force constant matrix of $\text{Ti}_{13}\text{Zr}^{cor}\text{C}_{13}$. The dotted line is computed with the force constant matrix of $\text{Ti}_{14}\text{C}_{13}$. Vibrational lines have been convoluted with a Gaussian of width 10 cm^{-1} to produce the curves.

E irreducible representations are infrared-active. Because of the symmetry lowering, due to alloying, there are more IR-active modes of $\text{Ti}_{13}\text{Zr}^{cor}\text{C}_{13}$ than of $\text{Ti}_{14}\text{C}_{13}$. Some vibrational levels in $\text{Ti}_{14}\text{C}_{13}$, such as those of A_{1g} , A_{2u} , E_g , E_u , T_{1g} , T_{2g} , T_{2g} and T_{2u} symmetry, which are not infrared-active, become infrared-active in the reduced symmetry of $\text{Ti}_{13}\text{Zr}^{cor}\text{C}_{13}$.

Changes in the vibrational spectrum due to alloying arise from two effects: force-constant modifications and differences between masses of titanium and zirconium atoms. It is useful to isolate the mass effect to see the extent to which it accounts for the change in the vibrational spectrum in going from $\text{Ti}_{14}\text{C}_{13}$ to $\text{Ti}_{13}\text{Zr}^{cor}\text{C}_{13}$. This is accomplished by computing the normal modes and frequencies with the force constants of pure $\text{Ti}_{14}\text{C}_{13}$, but with the mass of one corner titanium atom changed to that of zirconium. The normal-mode frequencies of $\text{Ti}_{13}\text{Zr}^{cor}\text{C}_{13}$ obtained using the force-constant matrix of $\text{Ti}_{14}\text{C}_{13}$ are shown in table 9.4, and the vibrational density of states of the IR-active modes computed with each of the two force-constant matrices are compared in figure 9.2. We can see that the densities of states computed with the force constant matrix of $\text{Ti}_{13}\text{Zr}^{cor}\text{C}_{13}$ and the force constant matrix of $\text{Ti}_{14}\text{C}_{13}$ are almost the same. This shows that changes in the IR vibrational spectrum on going from $\text{Ti}_{14}\text{C}_{13}$ to $\text{Ti}_{13}\text{Zr}^{cor}\text{C}_{13}$ are very much dominated by mass substitutions. In this case, alloying has very little effect on the force constants, and thus very little effect on the bonding properties.

Figure 9.3 Shows the IR spectrum, including the dipole oscillator strength of the IR-active modes, for both $\text{Ti}_{14}\text{C}_{13}$ and $\text{Ti}_{13}\text{Zr}^{cor}\text{C}_{13}$. As we see, even though $\text{Ti}_{13}\text{Zr}^{cor}\text{C}_{13}$ has a much richer IR density of states than $\text{Ti}_{14}\text{C}_{13}$, due to its reduced symmetry, its IR spectrum is nearly identical to that of $\text{Ti}_{14}\text{C}_{13}$. The geometric and electronic structure of the two nanocrystals are sufficiently similar that the new IR-active modes in $\text{Ti}_{13}\text{Zr}^{cor}\text{C}_{13}$ resulting from the reduced symmetry have very small dipole derivatives and are thus very weak.

Table 9.4: Normal-mode frequencies and symmetry labels for $\text{Ti}_{13}\text{Zr}^{cor}\text{C}_{13}$, with force-constant matrix from $\text{Ti}_{14}\text{C}_{13}$.

Frequency (cm^{-1})	Symmetry	Frequency (cm^{-1})	Symmetry	Frequency (cm^{-1})	Symmetry
146	E	324	E	483	E
176	A ₁	326	A ₁	483	A ₂
183	E	335	E	489	A ₁
197	E	340	A ₂	489	E
200	A ₁	361	A ₁	509	E
202	E	365	A ₂	526	A ₁
204	A ₂	366	E	560	E
227	A ₁	382	A ₁	563	A ₂
227	E	399	E	573	E
243	E	399	A ₂	663	A ₁
244	A ₁	415	E	666	E
265	E	415	A ₂	680	A ₁
286	E	416	A ₁	680	E
290	A ₂	416	E	740	A ₁
295	A ₁	422	E	744	E
296	E	481	E	787	A ₁
298	A ₁	481	A ₁		

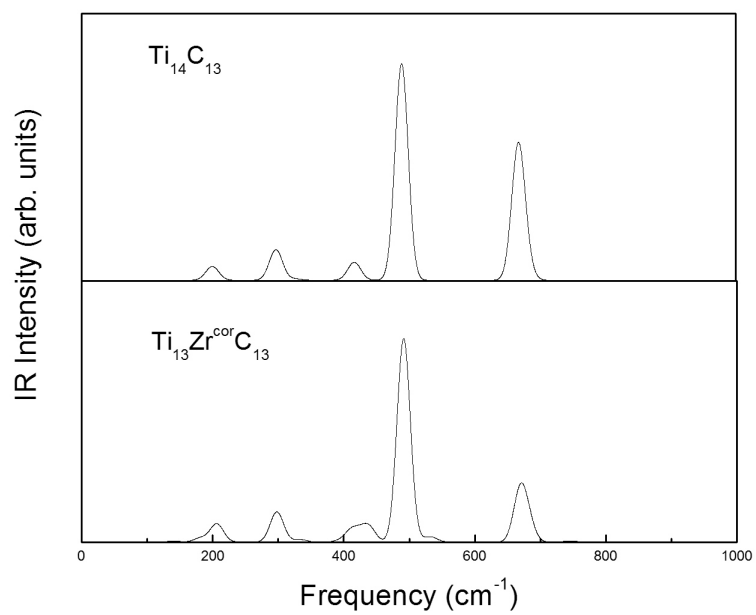


Figure 9.3: Computed IR spectrum for $\text{Ti}_{13}\text{Zr}^{cor}\text{C}_{13}$ compared to that of $\text{Ti}_{14}\text{C}_{13}$. Gaussian convolution width is 10 cm^{-1} .

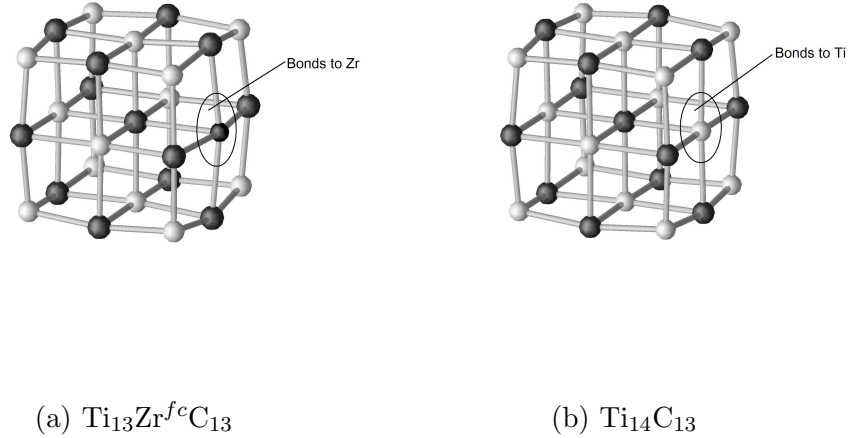


Figure 9.4: Equilibrium structure of $\text{Ti}_{13}\text{Zr}^{fc}\text{C}_{13}$ and $\text{Ti}_{14}\text{C}_{13}$. Significant lengthening of Zr-C bonds can be visualized.

9.3 $\text{Ti}_{13}\text{Zr}^{fc}\text{C}_{13}$

To study the properties of $\text{Ti}_{13}\text{Zr}^{fc}\text{C}_{13}$, I perform the same types calculations as I did for $\text{Ti}_{13}\text{Zr}^{cor}\text{C}_{13}$ and described in section 9.2. As shown in table 9.5 and visualized in figure 9.4, the lengths of the corresponding Ti-C bonds between $\text{Ti}_{13}\text{Zr}^{fc}\text{C}_{13}$ and in $\text{Ti}_{14}\text{C}_{13}$ are very similar, and the Zr-C in bonds $\text{Ti}_{13}\text{Zr}^{fc}\text{C}_{13}$ are longer than the corresponding Ti-C bonds in $\text{Ti}_{14}\text{C}_{13}$. The most significant change in $\text{Ti}_{13}\text{Zr}^{fc}\text{C}_{13}$ is the bond between the face-center zirconium atom to the body-center carbon atom, which is about 12% longer than the corresponding Ti-C bond in $\text{Ti}_{14}\text{C}_{13}$.

The $\text{Ti}_{13}\text{Zr}^{fc}\text{C}_{13}$ nanocrystal has C_{4v} symmetry. This reduction of symmetry from the O_h group of pure $\text{Ti}_{14}\text{C}_{13}$ will cause degenerate modes to split. Using standard group theoretical techniques, I find the splitting rules as shown in table 9.6.

Table 9.5: Positions of atoms in $\text{Ti}_{13}\text{Zr}^f\text{C}_{13}$ and $\text{Ti}_{14}\text{C}_{13}$. Coordinates are in units of Angstroms.

$\text{Ti}_{13}\text{Zr}^f\text{C}_{13}$				$\text{Ti}_{14}\text{C}_{13}$			
	x	y	z		x	y	z
Zr	2.36	0.00	0.00	Ti	2.10	0.00	0.00
Ti	-2.04	0.00	0.00	Ti	-2.10	0.00	0.00
Ti	0.04	2.10	0.00	Ti	0.00	2.10	0.00
Ti	0.04	-2.10	0.00	Ti	0.00	-2.10	0.00
Ti	0.04	0.00	2.10	Ti	0.00	0.00	2.10
Ti	0.04	0.00	-2.10	Ti	0.00	0.00	-2.10
Ti	2.00	2.05	2.05	Ti	2.01	2.01	2.01
Ti	-1.99	2.01	2.01	Ti	-2.01	2.01	2.01
Ti	2.00	-2.05	2.05	Ti	2.01	-2.01	2.01
Ti	2.00	2.05	-2.05	Ti	2.01	2.01	-2.01
Ti	-1.99	-2.01	2.01	Ti	-2.01	-2.01	2.01
Ti	2.00	-2.05	-2.05	Ti	2.01	-2.01	-2.01
Ti	-1.99	2.01	-2.01	Ti	-2.01	2.01	-2.01
Ti	-1.99	-2.01	-2.01	Ti	-2.01	-2.01	-2.01
C	0.06	0.00	0.00	C	0.00	0.00	0.00
C	2.12	2.27	0.00	C	2.14	2.14	0.00
C	-2.10	2.13	0.00	C	-2.14	2.14	0.00
C	2.12	-2.27	0.00	C	2.14	-2.14	0.00
C	-2.10	-2.13	0.00	C	-2.14	-2.14	0.00
C	0.00	2.14	2.14	C	0.00	2.14	2.14
C	0.00	-2.14	2.14	C	0.00	-2.14	2.14
C	0.00	2.14	-2.14	C	0.00	2.14	-2.14
C	0.00	-2.14	-2.14	C	0.00	-2.14	-2.14
C	2.12	0.00	2.27	C	2.14	0.00	2.14
C	-2.10	0.00	2.13	C	-2.14	0.00	2.14
C	2.12	0.00	-2.27	C	2.14	0.00	-2.14
C	-2.10	0.00	-2.13	C	-2.14	0.00	-2.14

Table 9.6: Mode splitting from $\text{Ti}_{14}\text{C}_{13}$ (O_h) to $\text{Ti}_{13}\text{Zr}^{fc}\text{C}_{13}$ (C_{4v}). The first column gives the number of the vibrational levels in $\text{Ti}_{14}\text{C}_{13}$ belonging to the corresponding symmetry label.

	$\text{Ti}_{14}\text{C}_{13}$ O_h irreducible representation		Splitting for C_{4v} symmetry
3	A_{1g}	\longrightarrow	A_1
0	A_{1u}	\longrightarrow	A_2
1	A_{2g}	\longrightarrow	B_1
2	A_{2u}	\longrightarrow	B_2
4	E_g	\longrightarrow	A_1+B_1
2	E_u	\longrightarrow	A_2+B_2
3	T_{1g}	\longrightarrow	A_2+E
7	T_{1u}	\longrightarrow	A_1+E
5	T_{2g}	\longrightarrow	B_2+E
4	T_{2u}	\longrightarrow	B_1+E

I expect there to be 60 vibrational levels for $\text{Ti}_{13}\text{Zr}^{fc}\text{C}_{13}$, including 15 labelled A_1 , 6 labelled A_2 , 9 labelled B_1 , 9 labelled B_2 , and 21 labelled E . Just as for $\text{Ti}_{13}\text{Zr}^{cor}\text{C}_{13}$, I also compare the vibrational modes calculated two different ways: one using the force constants specifically calculated for $\text{Ti}_{13}\text{Zr}^{cor}\text{C}_{13}$ and the other using the force constants of $\text{Ti}_{14}\text{C}_{13}$, where the effect of alloying on the modes only enters in the atomic masses. The results are shown in tables 9.7 and 9.8.

Among these modes, those of A_1 and E symmetry are IR-active. The vibrational density of states of the IR-active modes computed with these two methods are compared in figure 9.5. In contrast with the case for $\text{Ti}_{13}\text{Zr}^{cor}\text{C}_{13}$, it can be seen from figure 9.5 that changing the masses alone is not sufficient to account for the differences of the IR densities of states between $\text{Ti}_{14}\text{C}_{13}$ and $\text{Ti}_{13}\text{Zr}^{fc}\text{C}_{13}$. This suggests a difference in bonding characteristics between the Ti-C bond and Zr-C bond in this alloy nanocrystal. Table 9.9 compares vibrational levels of $\text{Ti}_{14}\text{C}_{13}$ and $\text{Ti}_{13}\text{Zr}^{fc}\text{C}_{13}$

Table 9.7: Normal-mode frequencies and symmetry labels for $\text{Ti}_{13}\text{Zr}^f\text{C}_{13}$.

Frequency (cm^{-1})	Symmetry	Frequency (cm^{-1})	Symmetry	Frequency (cm^{-1})	Symmetry
149	A ₂	319	E	485	B ₂
151	B ₂	324	A ₁	488	B ₁
167	A ₁	334	A ₁	491	A ₁
186	E	343	B ₁	501	E
189	B ₂	348	E	506	A ₂
192	E	366	A ₁	507	A ₁
205	B ₁	370	E	530	A ₁
208	E	374	B ₁	530	B ₁
213	A ₁	381	B ₂	534	E
233	E	397	E	547	B ₂
243	B ₂	412	A ₂	571	A ₂
253	B ₁	415	A ₁	638	E
253	B ₂	427	E	655	A ₁
254	A ₁	436	B ₁	688	A ₁
267	B ₁	453	E	695	B ₂
272	E	464	B ₁	695	E
282	A ₁	468	A ₁	749	E
299	A ₂	474	E	790	B ₂
303	E	485	E		

Table 9.8: Normal-mode frequencies and symmetry labels for $\text{Ti}_{13}\text{Zr}^{fc}\text{C}_{13}$, with force-constant matrix from $\text{Ti}_{14}\text{C}_{13}$.

Frequency (cm^{-1})	Symmetry	Frequency (cm^{-1})	Symmetry	Frequency (cm^{-1})	Symmetry
155	A ₂	324	A ₁	483	E
155	B ₂	325	E	483	B ₁
173	A ₁	326	A ₁	488	E
186	E	335	E	489	A ₁
194	B ₂	340	B ₁	509	A ₁
195	E	365	E	509	B ₁
200	E	365	B ₁	525	A ₁
204	B ₁	368	B ₂	563	E
223	E	374	A ₁	563	A ₂
232	B ₂	396	E	574	A ₂
236	A ₁	399	B ₁	574	B ₂
246	B ₁	412	E	667	E
254	B ₂	415	A ₂	667	A ₁
255	A ₁	416	A ₁	675	A ₁
267	B ₁	417	E	680	E
268	E	423	A ₁	744	E
290	A ₂	424	B ₁	745	B ₂
291	A ₁	472	E	789	B ₂
294	E	483	B ₂		

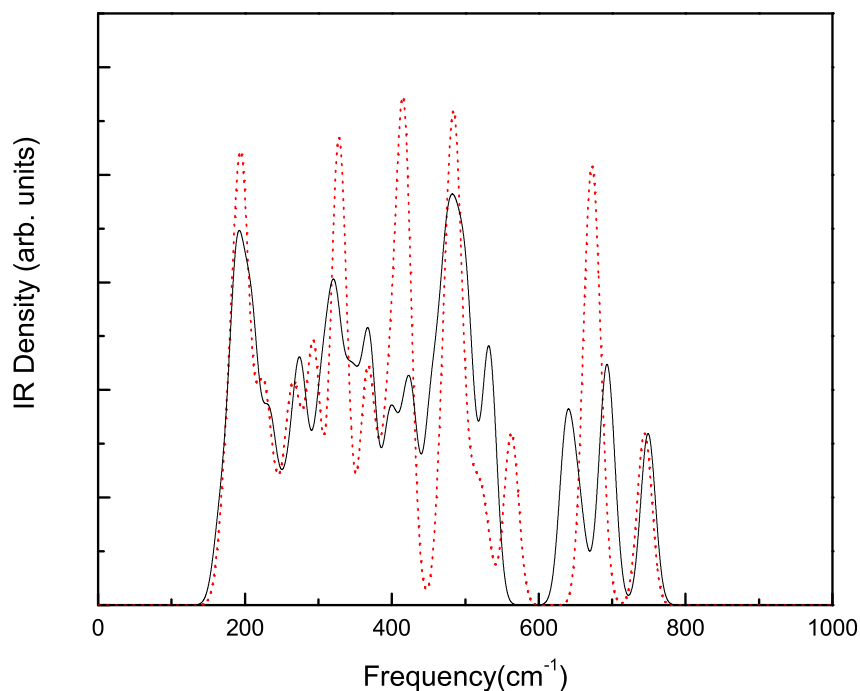


Figure 9.5: IR density of states of $\text{Ti}_{13}\text{Zr}^{fc}\text{C}_{13}$. The solid line is computed with the force constant matrix of $\text{Ti}_{13}\text{Zr}^{fc}\text{C}_{13}$. The dotted line is computed with the force constant matrix of $\text{Ti}_{14}\text{C}_{13}$. Vibrational lines have been convoluted with a Gaussian of width 10 cm^{-1} .

with frequencies greater than 600 cm^{-1} . The modes of $\text{Ti}_{13}\text{Zr}^{fc}\text{C}_{13}$ are computed two ways. One uses the same force-constants and masses as $\text{Ti}_{14}\text{C}_{13}$, except the mass of one face-center titanium atom is replaced with the mass of the zirconium atom. This allows us to see the effect of the pure mass change on the frequencies. The other way uses both correct force constants and masses of $\text{Ti}_{13}\text{Zr}^{fc}\text{C}_{13}$. In comparison with the frequencies calculated in the first way, the frequency splitting calculated in the second way can additionally show the effects on changes in bonding.

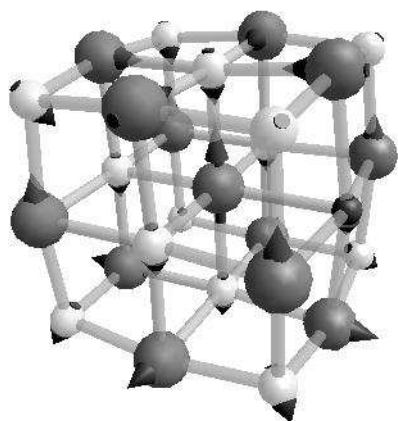
Table 9.9: Shifts of normal-mode frequencies in going from $\text{Ti}_{14}\text{C}_{13}$ (O_h) to $\text{Ti}_{13}\text{Zr}^{fc}\text{C}_{13}$ (C_{4v}). The frequencies are in units of cm^{-1} .

$\text{Ti}_{14}\text{C}_{13}$		$\text{Ti}_{13}\text{Zr}^{fc}\text{C}_{13}$			
		Using $K_{\text{Ti}_{13}\text{C}_{13}\text{Zr}^{fc}}$		Using $K_{\text{Ti}_{13}\text{Zr}^{fc}\text{C}_{13}}$	
frequency	symmetry	frequency	symmetry	frequency	symmetry
789	A_{2u}	789	B_2	790	B_2
745	T_{2g}	745	B_2	749	E
		744	E	695	B_2
679	T_{1u}	680	E	695	E
		675	A_1	655	A_1
667	T_{1u}	667	A_1	638	E
		667	E	688	A_1

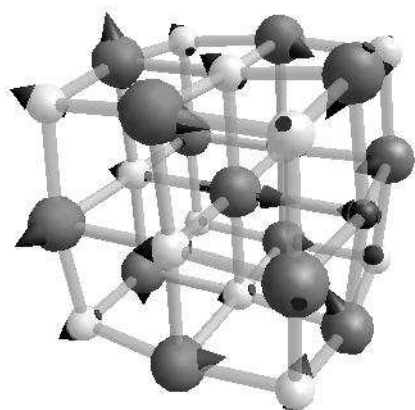
The comparisons in table 9.9 show that the change in bond stiffness due to replacing a face-center titanium atom with zirconium plays a significant role. The Zr-C bond and Ti-C bond in $\text{Ti}_{13}\text{Zr}^{fc}\text{C}_{13}$ are quite different. For example, consider the 679 cm^{-1} T_{1u} mode of $\text{Ti}_{14}\text{C}_{13}$. In $\text{Ti}_{13}\text{Zr}^{fc}\text{C}_{13}$, using the correct force constants, this mode splits into a 695 cm^{-1} E mode and a 655 cm^{-1} A_1 mode. The large 40 cm^{-1} splitting can be understood by comparing the normal-mode displacement patterns, as shown in figure 9.6. It shows that the largest amplitude of vibration is on the central carbon atom in both cases. For the A_1 mode, this vibration stretches and compresses the bond to the zirconium atom, whereas for the E modes, the central carbon vibrates perpendicular to this bond. Thus, the much lower frequency of the A_1 mode compared to the E mode indicates that bonding of the central carbon to the zirconium atom at the face-center is weaker than to the titanium atoms at the other faces in $\text{Ti}_{13}\text{Zr}^{fc}\text{C}_{13}$. One may argue that the highest frequency modes, labelled A_{2u} for $\text{Ti}_{14}\text{C}_{13}$ and B_2 for $\text{Ti}_{13}\text{Zr}^{fc}\text{C}_{13}$, are essentially the same, indicating that this

mode does not probe changes in bonding due to the Zr substitution. Actually, the mode with the highest frequency in B_2 symmetry does not activate the Zr-C bonds in $Ti_{13}Zr^{fc}C_{13}$. But this indicates that Ti-C bonds in $Ti_{13}Zr^{fc}C_{13}$ and $Ti_{14}C_{13}$ are very similar. I also examine the difference between the Zr-C bond in $Ti_{13}Zr^{fc}C_{13}$ and the corresponding Ti-C bond in $Ti_{14}C_{13}$. As shown in the table 9.9, if we use the force-constant matrix of $Ti_{14}C_{13}$ but the correct masses of the $Ti_{13}Zr^{fc}C_{13}$, the 679 cm^{-1} mode of $Ti_{14}C_{13}$ split into an E mode at frequency 680 cm^{-1} and an A_1 mode at frequency of 675 cm^{-1} . Similar to the splitting calculated with the correct force constants and masses of $Ti_{13}Zr^{fc}C_{13}$, as stated above, only the A_1 mode involves stretching and compressing of the Zr-C bond. For this mode, however, there is a red-shift from 675 cm^{-1} using the force constants of $Ti_{14}C_{13}$ to 655 cm^{-1} using the force constants of $Ti_{13}Zr^{fc}C_{13}$. This indicates that the Zr-C bond between the central carbon to the face-center in $Ti_{13}Zr^{fc}C_{13}$ is softer than the corresponding Ti-C bond in $Ti_{14}C_{13}$. Similar analysis shows the Zr-C bonds between the face-center zirconium atom and the edge-center carbon atoms in $Ti_{13}Zr^{fc}C_{13}$ are also softer than the corresponding Ti-C bonds in $Ti_{14}C_{13}$.

The splitting of vibrational frequencies associated with the Zr-C bond in $Ti_{13}Zr^{fc}C_{13}$ also affects the IR spectrum, with intensities calculated from the dipole derivatives as before. As shown in figure 9.7, the large mode splittings discussed above result in new features in the IR spectrum of $Ti_{13}Zr^{fc}C_{13}$, compared with the IR spectrum of $Ti_{14}C_{13}$. These new features are sufficiently widely separated that they should be clearly detectable experimentally, if $Ti_{13}Zr^{fc}C_{13}$ could ever be formed in abundance.



(a)



(b)

Figure 9.6: Vibrations mainly activating the body-center atom in $\text{Ti}_{13}\text{Zr}^f\text{C}_{13}$.
(a) $\text{Ti}_{13}\text{Zr}^f\text{C}_{13}$ E mode 695 cm^{-1}
(b) $\text{Ti}_{13}\text{Zr}^f\text{C}_{13}$ A_1 mode 655 cm^{-1}

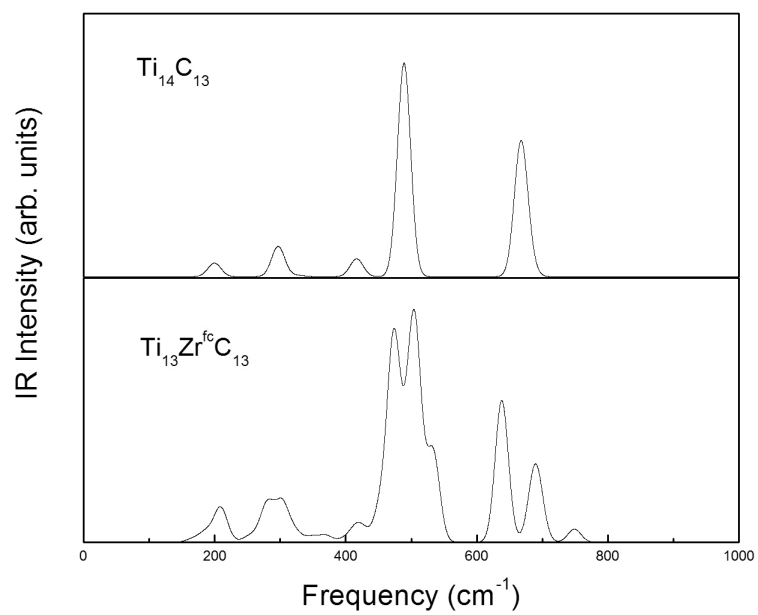


Figure 9.7: Computed IR spectrum for $\text{Ti}_{13}\text{Zr}^{fc}\text{C}_{13}$ compared to that of $\text{Ti}_{14}\text{C}_{13}$. Gaussian convolution width is 10 cm^{-1} .

Table 9.10: Ti-C and Zr-C bond-length comparison in bulk and $\text{Ti}_{13}\text{ZrC}_{13}$ nanocrystals. The table compares the Zr-C bond and Ti-C bond for bulk pure crystal, the Zr-C bond of $\text{Ti}_{13}\text{Zr}^{cor}\text{C}_{13}$ and Ti-C bond of $\text{Ti}_{14}\text{C}_{13}$ between edge-center and corner (EC), the Zr-C bond of $\text{Ti}_{13}\text{Zr}^{fc}\text{C}_{13}$ and Ti-C bond of $\text{Ti}_{14}\text{C}_{13}$ between the body-center and face-center (BF), and between the face-center and edge-center (FE).

Bond type	Zr-C bond-length(Å)	Ti-C bond-length (Å)
Bulk	2.35	2.17
EC	2.13	2.02
BF	2.36	2.10
FE	2.28	2.14

9.4 $\text{Ti}_{13}\text{ZrC}_{13}$ AND $\text{Ti}_{14}\text{C}_{13}$

As discussed in the last two sections, the Zr-C bond in the $\text{Ti}_{13}\text{ZrC}_{13}$ nanocrystal is longer than the Ti-C bond. This is not unexpected, as we know that the zirconium atom is larger than the titanium atom, and the Zr-C bond in the bulk ZrC crystal is also longer than the Ti-C bond in the bulk TiC crystal. Table 9.10 compares the lengths of the bonds directly connected to the zirconium atom in the two forms of $\text{Ti}_{13}\text{ZrC}_{13}$ and the corresponding bonds in $\text{Ti}_{14}\text{C}_{13}$. In the nanocrystals, the bond-length trends for Zr-C bonds track those for Ti-C bonds quite well, including the significant bond shortening relative to bulk and the shortening of bonds to atoms at corner sites.

Having calculated the vibrational spectra of $\text{Ti}_{13}\text{Zr}^{cor}\text{C}_{13}$ and $\text{Ti}_{13}\text{Zr}^{fc}\text{C}_{13}$. we would like to predict the vibrational spectrum of $\text{Ti}_{13}\text{ZrC}_{13}$ that would be seen experimentally. The relative weights of each species that go into computing the total spectrum depend on the relative abundances of each $\text{Ti}_{13}\text{ZrC}_{13}$ species. A simple model, which could easily be applied to the general $\text{Ti}_{14-x}\text{Zr}_x\text{C}_{13}$ alloy, assumes zirconium

atoms go randomly on the metal sites. Then the contribution of each distinct isomer would be proportional to the number of configurations that are equivalent to each other by symmetry for this isomer. For example, in $\text{Ti}_{13}\text{ZrC}_{13}$, there are 6 possible ways for the zirconium atom to occupy at a face-center site and 8 possible ways to occupy a corner site. Thus, if it is a completely random occupation, the predicted $\text{Ti}_{13}\text{ZrC}_{13}$ IR spectrum, $I_{\text{Ti}_{13}\text{ZrC}_{13}}$, would be given by

$$I_{\text{Ti}_{13}\text{ZrC}_{13}} \propto 8I_{\text{Ti}_{13}\text{Zr}^{cor}\text{C}_{13}} + 6I_{\text{Ti}_{13}\text{Zr}^{fc}\text{C}_{13}}.$$

The IR spectrum for $\text{Ti}_{13}\text{ZrC}_{13}$, assuming random substitution, is shown in figure 9.8. The IR spectrum for $\text{Ti}_{14}\text{C}_{13}$ is reproduced in the upper panel for comparison. It shows that the IR peak of frequency $\sim 680 \text{ cm}^{-1}$ splits into two distinct intense peaks for $\text{Ti}_{13}\text{ZrC}_{13}$, one still at $\sim 680 \text{ cm}^{-1}$ and the other red-shifted to $\sim 630 \text{ cm}^{-1}$. The splitting is primarily due to $\text{Ti}_{13}\text{Zr}^{fc}\text{C}_{13}$, as discussed in the previous section.

The random zirconium occupation model is overly simplistic. Different distributions of the same number of zirconium atoms on different metal sites may result in alloy nanocrystals of very different total energy. Indeed, we find for $\text{Ti}_{13}\text{ZrC}_{13}$ that $\text{Ti}_{13}\text{Zr}^{cor}\text{C}_{13}$ is 0.64 eV lower in energy than $\text{Ti}_{13}\text{Zr}^{fc}\text{C}_{13}$. As we have seen, this difference in energy is related to the relative weakening of bonds to zirconium in $\text{Ti}_{13}\text{Zr}^{fc}\text{C}_{13}$, as compared to $\text{Ti}_{13}\text{Zr}^{cor}\text{C}_{13}$. Assuming that the difference in free energy between various configurations of a given nanocrystal alloy composition is dominated by difference in total energy, i.e. $\Delta E \approx \Delta F$, then we would expect the relative abundance of two such configuration to be proportional to $e^{-\frac{\Delta E}{kT}}$, where k is the Boltzmann constant and T is the temperature. Based on these considerations, at a temperature of 3,000K, which is probably in the range of experimental conditions for the laser vaporization experiments, $\text{Ti}_{13}\text{Zr}^{cor}\text{C}_{13}$ would be about 12 times more abundant than $\text{Ti}_{13}\text{Zr}^{fc}\text{C}_{13}$. In fact, the approach using the random

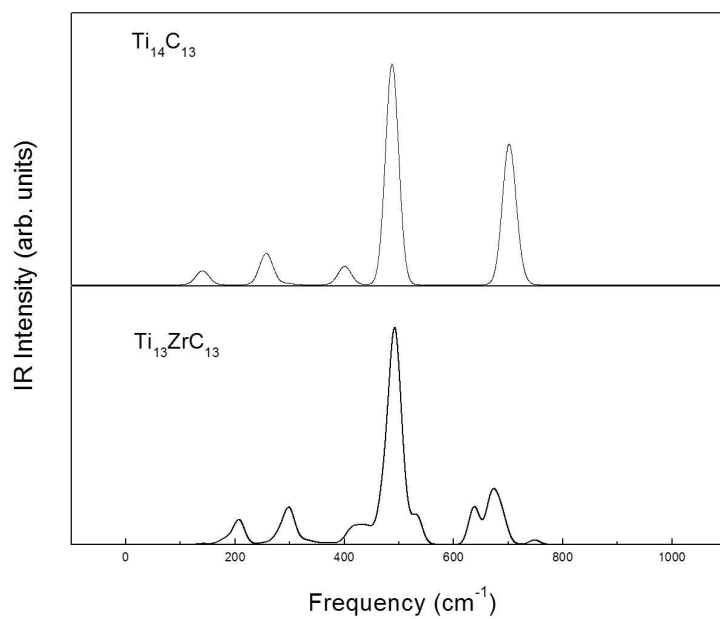


Figure 9.8: IR spectrum of $\text{Ti}_{13}\text{ZrC}_{13}$ calculated using random substitution model. It is compared with the calculated IR spectrum of $\text{Ti}_{14}\text{C}_{13}$.

zirconium occupation model is equivalent to considering $T = \infty$, where any anharmonic temperature effects, including thermal dissociation, are ignored. As a result of the different relative abundances of $\text{Ti}_{13}\text{Zr}^{cor}\text{C}_{13}$ and $\text{Ti}_{13}\text{Zr}^{fc}\text{C}_{13}$ at finite temperature, the IR spectrum of $\text{Ti}_{13}\text{ZrC}_{13}$ will be dominated by $\text{Ti}_{13}\text{Zr}^{cor}\text{C}_{13}$. Because $\text{Ti}_{13}\text{Zr}^{cor}\text{C}_{13}$ has a very similar IR spectrum to $\text{Ti}_{14}\text{C}_{13}$, as described in section 9.2, the prominent new IR features coming from $\text{Ti}_{13}\text{Zr}^{fc}\text{C}_{13}$ are predicted to be very weak in the IR spectrum of $\text{Ti}_{13}\text{ZrC}_{13}$.

CHAPTER 10

CONCLUSIONS

Inspired by experimental observations of the sizable abundance of stable transition-metal carbide nanocrystals, observed in laser-vaporization molecular beam experiments, I performed first-principles calculations, using density functional theory, to analyze the structural, energetic, vibrational, and electronic properties of the $3 \times 3 \times 3$ titanium carbide nanocrystals $\text{Ti}_{14}\text{C}_{13}$ and absence of $\text{Ti}_{13}\text{C}_{14}$, which both can be viewed as fragments of bulk TiC. The analysis presented in my dissertation reveals a physical explanation for the prominence of $\text{Ti}_{14}\text{C}_{13}$ and absence of $\text{Ti}_{13}\text{C}_{14}$ in the molecular beam experiments. Using two auxiliary systems, Ti_6C_{13} and Ti_{13}C_6 , the effects of taking corner atoms away from the two sibling $3 \times 3 \times 3$ nanocrystals are examined. The analysis leads me to conclude that carbon atoms at corner sites form much weaker bonds to the other atoms of the nanocrystal than when metal atoms occupy the corner sites. Vibrational analysis further strengthens the above picture and reproduces the infrared spectrum of $\text{Ti}_{14}\text{C}_{13}$, in comparison with experimental data. An electronic explanation is given as well. In $\text{Ti}_{14}\text{C}_{13}$, which is observed abundant in the experiments, the d orbitals of titanium atoms are well adapted to the right geometrical arrangement for corner sites and form strong bonds with adjacent edge-center carbon atoms, as well as adjacent face-center titanium atoms. In contrast, in the hypothetical nanocrystal $\text{Ti}_{13}\text{C}_{14}$, the s and p orbitals accessible to corner carbon atoms for forming bonds lack the orientational flexibility needed to form strong bonds with the three adjacent edge-center titanium atoms, and thus

the corner bonds that do form in this species are highly strained and consequently weakened.

The effect of alloying in titanium carbide nanocrystals is also examined in my research. Two categories of $\text{Ti}_{13}\text{ZrC}_{13}$ isomers, $\text{Ti}_{13}\text{Zr}^{cor}\text{C}_{13}$ and $\text{Ti}_{13}\text{Zr}^{fc}\text{C}_{13}$, are compared to each other and to pure $\text{Ti}_{14}\text{C}_{13}$. In the analysis of the vibrational spectrum, the alloy effects are separated into the change of mass and the modifications of the force constants. It is found that the force constants in $\text{Ti}_{13}\text{Zr}^{cor}\text{C}_{13}$ are almost identical to those of $\text{Ti}_{14}\text{C}_{13}$, and the peaks in its IR spectrum are only slightly broadened relative to those in $\text{Ti}_{14}\text{C}_{13}$. But in $\text{Ti}_{13}\text{Zr}^{fc}\text{C}_{13}$, the Zr-C bonds are longer and weaker than the other Ti-C bonds. This difference leads to new peaks in the IR spectrum of $\text{Ti}_{13}\text{Zr}^{fc}\text{C}_{13}$, which may be observable in the experiments if it could ever be formed in sufficient abundance. As the DFT calculation shows, the total energy of $\text{Ti}_{13}\text{Zr}^{cor}\text{C}_{13}$ is significantly lower than that of $\text{Ti}_{13}\text{Zr}^{fc}\text{C}_{13}$. Thus, the abundance of $\text{Ti}_{13}\text{Zr}^{cor}\text{C}_{13}$ is predicated to be considerably higher than that of $\text{Ti}_{13}\text{Zr}^{fc}\text{C}_{13}$ in an equilibrium ensemble of $\text{Ti}_{13}\text{ZrC}_{13}$ nanocrystals. Hence, the new feature of the IR spectrum predicted for $\text{Ti}_{13}\text{Zr}^{fc}\text{C}_{13}$ is not expected to be prominent in the overall $\text{Ti}_{13}\text{ZrC}_{13}$ IR spectrum.

APPENDIX A

A TOOL TO VISUALIZE NORMAL MODES OF VIBRATION

A.1 INTRODUCTION

Among various approaches employed to gain insight into interactions that occur at the atomic level in the field of nanoscience, one useful method is to perform vibrational analysis, from which we can obtain information about structure and bonding properties, and then compare to experiments of infrared and Raman spectra. However, the quantity of data provided for the vibrational normal modes is very large. Looking at the results in their numeric form is cumbersome and impractical, even for simple molecules with only a few atoms. A valuable alternative is to use a visualization tool to generate a 3D animation of each normal mode to gain a better understanding of the physical implications of the modes. With the help of advanced Java technologies including Java 3D and Java Advanced Imaging [60–64], I have created a software tool, named OSCILLATOR, to construct the molecular system and visualize the normal modes of vibration in three dimensions. This tool has been used in my research on transition-metal carbide nanocrystals.

OSCILLATOR includes many useful features that are required to visualize the vibrational modes of coupled oscillators. The tool can visualize each normal mode of vibration either by animating the atomic motions for that mode or by drawing arrows to show the vibrational pattern in a static 3D image. The following sections do not go into details of my Java3D programming [63, 64], but rather give an overview of the major elements used in this tool.

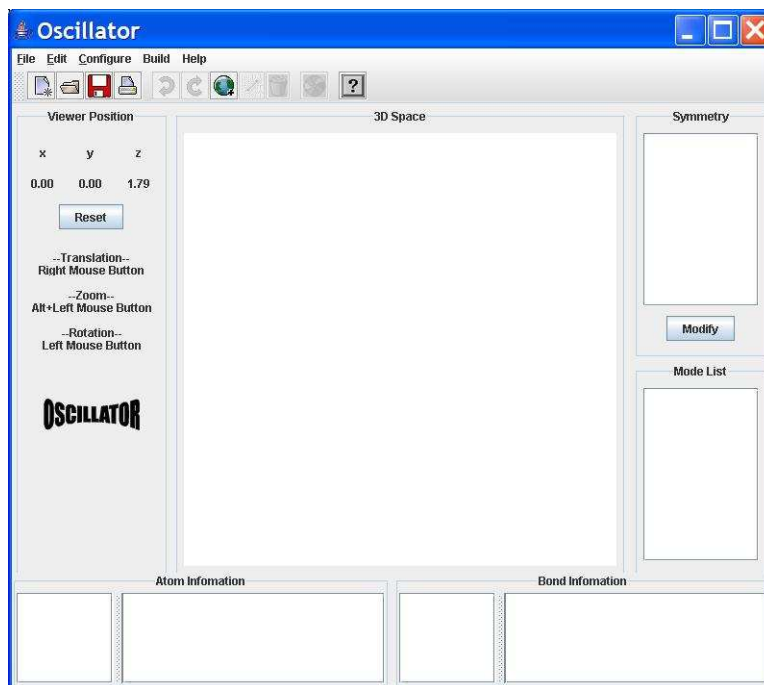


Figure A.1: Main Layout of OSCILLATOR.

A.2 USER INTERFACE

Programmed in Java, OSCILLATOR is a cross-platform application. The prerequisite is to install the J2SE [65] and Java3D packages. As of the writing of this dissertation, the latest versions of J2SE and Java3D can be downloaded from Sun’s website [66]. The tool has been archived in a Jar file and can be run with the command “java -jar ”. When the program is open, the main layout of OSCILLATOR is as shown in figure A.1. The topmost part of the window is the main Menu, which controls all functions of this tool. The toolbar, which gives a collection of the most frequently used functions, is under the main menu and is separated into several groups according to their functions, including file input/output, system configuration, appearance

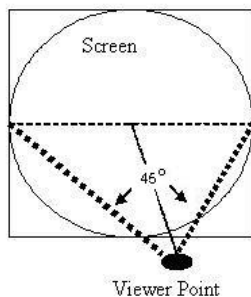


Figure A.2: Field of View in OSCILLATOR.

modification, and help. The the middle panel is the “canvas” where the 3D image resides. When exporting images or movies, the content in this panel is saved. The 3D images on the canvas are drawn in one-point perspective [67, 68], as shown in figure A.2. If we treat the vanishing point in this perspective as the user’s eye position, or the viewer point, the user’s view field is set to be fixed as 45° . By default, or if the user clicks the reset button on the left panel, the z axis points out the canvas perpendicularly, and the center of the canvas is at the origin of the coordinate system. Thus, the viewer point is at $z \approx 1.79$, and objects with x and y range of -1.0 to $+1.0$ at the $z = 0$ plane can be fully viewed across. The user can navigate through the 3D space using the mouse. Brief instructions on how to navigate through the 3D space are shown on the left panel of the main layout, along with the reset button. On the left panel, the x, y, z position of the viewer, indicating the vanishing point, is also updated when the user navigates through the 3D space. On the bottom of the main layout, the labels of the atoms and bonds and their properties are to be listed. The 3D objects in the canvas and their labels in the list panel are maintained concurrently. When atoms or bonds are added by the user and shown in the canvas, their labels will

be listed in the panels below. If a 3D object is selected by clicking, no matter whether in the 3D canvas or in the list panel containing labels, the selected object will blink in the canvas and will be highlighted in the list panel. When objects are selected, their detailed properties will also be shown in the property panels to the right of the label panels at the bottom. On the right of the main layout is the symmetry list panel, where the user can read the currently specified symmetry information for the system. If the “Modify” button in this panel is clicked, a dialog box will open for the user to modify the symmetry constraints for the molecular system. The list of normal modes of vibration is shown on the panel below the symmetry list panel. After loading information about the modes, the labels for the modes, usually indicated by their frequencies, will be shown in order. The user can visualize any vibrational mode by selecting a mode label in this panel. The overall vibrational amplitude in a mode animation is exaggerated to make the atomic motions clearly visible.

A.3 SYSTEM CONFIGURATION

In this tool, atoms are represented by spheres. When the user clicks the menu item Edit/Add Atom, a dialog box will open as in Figure A.3. The user then sets the atom position, sphere radius and appearance, followed by clicking the “Add” button. For a specific system, the size of the 3D objects on the canvas can be zoomed using the mouse. Rotations about the origin can be made via a mouse drag motion with the left mouse key pressed. Translation parallel to the screen can be made via a mouse drag motion with the right mouse button pressed. Zooming perpendicular to the viewer screen can be made via a mouse drag motion with either the middle mouse button pressed or the Alt-key plus left mouse button simultaneously pressed.

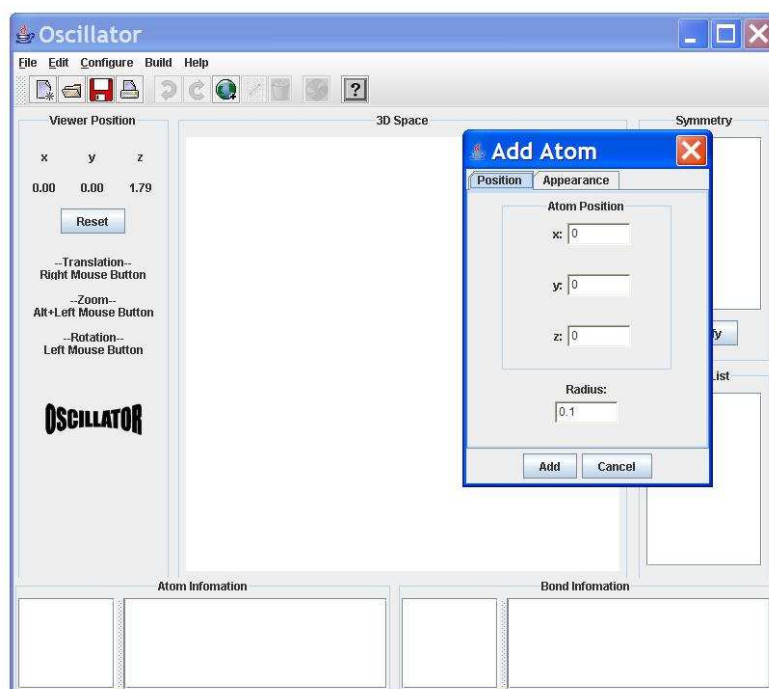


Figure A.3: Interactive dialog for adding or editing an atom.

The geometry of the system is easy to interpret if interatomic bonds are also visualized. In this tool, bonds are represented by cylinders connecting the atoms. The user first chooses the atoms that are to be bonded either by selecting from the atom list or by picking directly from the 3D canvas. When the atoms are blinking, indicating that they are selected, the user can click the menu item Edit/Add Bond. After selecting the bond color in the pop up dialog window, bonds will be added connecting the nearest neighbors among selected atoms.

If the system size is large, it can be very tedious to adding atoms and bonds one-by-one. This tool allows the user to use the symmetry of the system to make building the configuration faster. Each symmetry operation is realized by a 3×3 transformation matrix that transforms all the atom positions. The tool has pre-defined several basic symmetry operations, such as inversion, reflection and n-fold rotations. A list of symmetry operations, specified by the user, is always maintained in the program. When the user adds atoms or bonds, the symmetry operations in the symmetry list are checked one-by-one to see if any more atoms or bonds should be added to maintain the symmetry. If so, the program will ask the user either to add the new objects or to remove the broken symmetry operations from the list. Note that adding new atoms and bonds could introduce more unmapped atoms or bonds. Therefore, this procedure is recursive, and if the user cancels in the middle of the procedure, no atoms or bonds will be added.

It is very simple to delete atoms or bonds when the user wants to modify the system. The user only needs to choose the atoms or bonds to be deleted either by selecting them from the list panel or by picking them directly from the 3D canvas, and then press the delete button in the toolbar. Similar to adding atoms or bonds, when the user removes atoms or bonds, the symmetry operations in the symmetry list are also checked one-by-one to see if any symmetries are broken. If so, the program will find the unmapped atoms or bonds and ask whether they should also be deleted.

Note that deleting the mapped object could cause a third object to be unmapped by some symmetry. In this case, a set of all deleted objects is maintained. If the user cancels in the middle of the procedure, the atoms or bonds in the set will be put back onto the canvas. The OSCILLATOR tool also supports “Undo” and “Redo” functions, in case the user modifies the system erroneously.

To simplify the initial system configuration of the molecule, the tool also supports the import of a system-configuration file. The following is an example of such an input file, drawn from my research on $\text{Ti}_{13}\text{ZrC}_{13}$:

```
*****
```

```
OSCILLATOR - - - Research-0.0.1
```

```
Ti13C13Zr
```

```
3 // # of species
```

```
Zr
```

```
1 0.024 0 0 0 // # of Zr atoms, radius, r g b color
```

```
0.2055304626 0.2055304626 0.2055304626
```

```
Ti
```

```
13 0.03 0.6 0.6 0.6 // # of Ti atoms, radius, r g b color
```

```
0.2039474879 -0.0004336492 -0.0004336492
```

```
-0.2042850431 -0.0005424017 -0.0005424017
```

```
-0.0004336492 0.2039474879 -0.0004336492
```

```
-0.0005424017 -0.2042850431 -0.0005424017
```

```
-0.0004336492 -0.0004336492 0.2039474879
```

```
-0.0005424017 -0.0005424017 -0.2042850431
```

```
-0.1970392410 0.1949460653 0.1949460653
```

```
0.1949460653 -0.1970392410 0.1949460653
```

```
0.1949460653 0.1949460653 -0.1970392410
```

```
-0.1959264718 -0.1959264718 0.1947540635
```

```

0.1947540635 -0.1959264718 -0.1959264718
-0.1959264718 0.1947540635 -0.1959264718
-0.1955860334 -0.1955860334 -0.1955860334
C
13 0.045 0.2 0.2 0.2 // # of C atoms, radius, r g b color
0.0000148717 0.0000148717 0.0000148717
0.2078266148 0.2078266148 -0.0019371636
-0.2076161319 0.2077690036 -0.0002206789
0.2077690036 -0.2076161319 -0.0002206789
-0.2083253840 -0.2083253840 -0.0000402928
-0.0019371636 0.2078266148 0.2078266148
-0.0002206789 -0.2076161319 0.2077690036
-0.0002206789 0.2077690036 -0.2076161319
-0.0000402928 -0.2083253840 -0.2083253840
0.2078266148 -0.0019371636 0.2078266148
-0.2076161319 -0.0002206789 0.2077690036
0.2077690036 -0.0002206789 -0.2076161319
-0.2083253840 -0.0000402928 -0.2083253840
bond
0.01 // bond radius

```

```

*****end of file*****

```

The file is in a specific format. The version is named “Research-0.0.1” in the first line and cannot be changed if this format is used. The user can specify a brief, descriptive comment in the second line, which will be skipped when read in. The following lines described the atoms and bonds. If the user wants to include comments, he or she can put them at the end of each line following a “//” designator.

The third line of the file gives the number of species of atoms. This file contains three species of atoms, including Zr, Ti, and C, details of which are described in the next three sections. Each section gives the name of the element first. Then the number of atoms of that type, the radius for the spheres that represent the atoms, and the color of these spheres are given in the next line. The color is given as red, green, and blue, at the range [0..1]. The Cartesian coordinates of each atom of the same species are then given line-by-line. After the atoms are configured in each section, bonds are then configured. For this format version, “Research-0.0.1”, only the radius of the bond is given, only nearest-neighbor bonds will be drawn. For a different version, i.e. “Research-0.0.2”, more properties, such as bond color, may be required. Details for different format versions can be found in the help pages of the tool. After the file is imported using the menu command “File/Import config”, the user can further modify the system as previously discussed. After the user finishes the configuration, he or she can save it for later use. The saved format is different from the format of the imported file. An internal format is used and contains more information, such as the position of the vanishing point for the 3D visualization. The user can use menu “File/open” to open the saved file with the internal format, and the 3D image will be shown in exactly the same way as when it was saved. The static image on the 3D screen, which illustrates the configuration of the system, can also be exported to a jpeg file.

A.4 VISUALIZING VIBRATIONAL MODES

Information specifying the vibrational modes is imported into OSCILLATOR from a text file with the following general configuration:

```
*****
OSCILLATOR - - - Version Modes-0.0.1
```

```

Ti13ZrC13
81 // degree of freedom
// eigen frequencies
...
...
// eigen vectors
... ..
... ..
18 0.9 // frame, amplitude
*****end of file*****

```

In a similar manner as the file that configures the system, this input version is named “Modes-0.0.1”, and the user can provide a descriptive title in the second line. The third line gives the number of atomic degrees of freedom, which should equal $3N$ if the number of atoms in the system is N . The next line “// eigen frequencies” is followed by $3N$ lines specifying labels for $3N$ eigen frequencies. Usually one can just use the values of the frequencies as the labels. Following the line “// eigen frequencies”, the next $3N$ lines give the $3N \times 3N$ matrix for the eigenvectors. The $3N$ numbers in each row are separated by blank spaces and each eigenvector is specified in a column of the matrix. The $3N$ eigenvectors have a one-to-one correspondence with the $3N$ mode frequencies, in the same order. For each eigenvector, the $3N$ values give the relative motion of the N atoms, with predefined order, in the x , y , and z direction. The last line of this text file gives the number of frames that will be calculated and visualized for one cycle of vibration and a coefficient to adjust the amplitude of the vibrations.

After the mode configuration file is loaded, the labels of the normal modes will be shown in the mode list. If the user selects “show animation” in the menu, the modes can be shown in real-time animations. If this menu item is deselected, arrows through

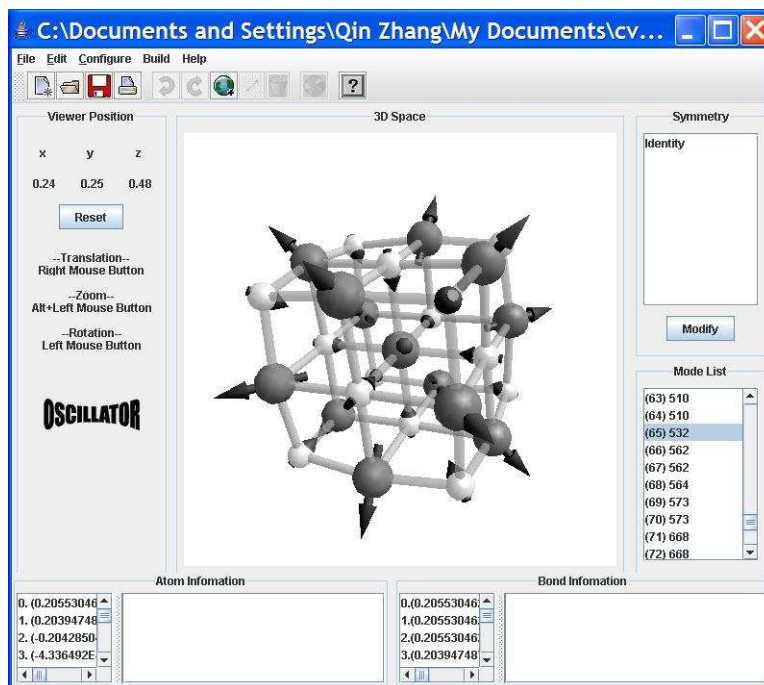


Figure A.4: Visualization of a normal mode. The relative motions of atoms are indicated using arrows.

spheres are used to point in the direction of the atomic motion at an instant of the vibration, as shown in figure A.4. The lengths of the arrows are proportional to the relative magnitudes of the atomic displacements in the vibrations. In the animated mode, all the frames of the motion can be saved one-by-one to jpeg files using menu item “File/Save movie”, and a Quick Time movie file is generated using these frames. It is important to note that the oscillation frequency of an animated mode is the *same* for all modes and is *not* proportional to the specific mode frequency. In the static format, the image of the system with arrows attached can be exported to a single jpeg file.

A.5 SUMMARY

This tool, OSCILLATOR, provides for interactive and collaborative visualization of numerical data in analyzing the normal modes of vibration. The above sections give an overview of the functions of the tool. It offers a user friendly interface including menu and tool bar. In the main layout, the detailed information of atoms and bonds is updated concurrently with their modification on the 3D canvas. In addition, the viewer's position and the symmetry information of the system are also easily set and shown. After loading the large set of numerical data specifying normal modes, the user can visualize these vibrational modes in both animated and static formats. Images of the system configuration and frames for small movies of the vibrational modes can be exported to files in standard formats. The present version of this tool has been used to generate several figures appearing in this dissertation.

BIBLIOGRAPHY

- [1] J. S. Pilgrim and M. A. Duncan, "Beyond metallo-carbohedrenes: Growth and decomposition of metal-carbon nanocrystals," *Journal of the American Chemical Society*, vol. 115, p. 9724, 1993.
- [2] J. S. Pilgrim and M. A. Duncan, "Metallo-carbohedrenes - chromium, iron, and molybdenum analogs," *Journal of the American Chemical Society*, vol. 115, p. 6958, 1993.
- [3] B. C. Guo, K. P. Kerns, and A. W. Castleman Jr., " $\text{Ti}_8\text{C}_{12}^+$ -metallo-carbohedrenes: A new class of molecular clusters," *Science*, vol. 255, pp. 1411–1413, 1992.
- [4] J. Purnell, S. Wei, and A. W. Castleman Jr., "Studies of the metastable decay of Met-Cars - the vanadium and niobium systems," *Chemical Physics Letters*, vol. 229, p. 105, 1994.
- [5] A. W. Castleman Jr. and K. H. Bowen, "Clusters: Structure, energetics, and dynamics of intermediate states of matter," *Journal of Physical Chemistry*, vol. 100, p. 12911, 1996.
- [6] I. Dance, "Geometric and electronic structures of $\text{Ti}_8\text{C}_{12}^+$: Analogies with C_{60} ," *Journal of the Chemical Society-Chemical Communications*.
- [7] Z. Y. Lin and M. B. Hall, "Structure and bonding in M_8C_{12} clusters," *Journal of the American Chemical Society*, vol. 114, p. 10054, 1992.

- [8] Z. Y. Lin and M. B. Hall, "Theoretical-studies on the stability of M_8C_{12} clusters," *Journal of the American Chemical Society*, vol. 115, p. 11165, 1993.
- [9] M. M. Rohmer, M. Berard, C. Bo, and J. M. Poblet, "Ab-initio SCF and CI investigations on titanium carbon clusters - metallocarbohedrenes Ti_8C_{12} and fcc crystallites $Ti_{14}C_{13}$," *Journal of the American Chemical Society*, vol. 117, p. 508, 1995.
- [10] L. S. Wang, S. Li, and H. Wu, "Photoelectron spectroscopy and electronic structure of Met-Car Ti_8C_{12} ," *Journal of Physical Chemistry*, vol. 19211, 1996.
- [11] I. Dance, "Nanocrystal $Ti_{14}C_{13}$ to metallocarbohedrene Ti_8C_{13} : Structural principles and mechanism," *Journal of the American Chemical Society*, vol. 118, p. 2699, 1996.
- [12] S. Li, H. B. Wu, and L. S. Wang, "Probing the electronic structure of metallocarbohedrenes: M_8C_{12} ($M=Ti, V, Cr, Zr, Nb$)," *Journal of the American Chemical Society*, vol. 119, p. 7417, 1997.
- [13] M. M. Rohmer, M. Benard, and J. M. Poblet, "Structure, reactivity, and growth pathways of metallocarboherenes M_8C_{12} and transition metal/carbon clusters and nanocrystals: A challenge to computational chemistry," *Chemical Reviews*, vol. 100, p. 495, 2000.
- [14] G. Gueorguiev and J. Pacheco, "Structural identification of Metcars," *Physical Review Letters*, vol. 88, p. 115504, 2002.
- [15] B. D. Leskiw and A. W. Castleman Jr., "Met-Cars: A unique class of molecular clusters," *Comptes Rendus Physique*, vol. 3, p. 251, 2002.

- [16] Q. Zhang and S. P. Lewis, "Weak bonding of carbon atoms at corner sites in titanium-carbide nanocrystals," *Chemical Physics Letters*, vol. 372, p. 836, 2003.
- [17] H. Hou, J. T. Muckerman, P. Liu, and J. A. Rodriguez, "Computational study of the geometry and properties of the metcars Ti_8C_{12} and Mo_8C_{12} ," *The Journal of Physical Chemistry*, vol. 107, p. 9344, 2003.
- [18] P. Liu, J. A. Rodriguez, H. Hou, and J. T. Muckerman, "Chemical reactivity of metcar Ti_8C_{12} , nanocrystal $\text{Ti}_{14}\text{C}_{13}$ and a bulk TiC (001) surface: A density functional study," *The Journal of Chemical Physics*, vol. 118, p. 7737, 2003.
- [19] G. K. Gueorguiev and J. M. Pacheco, "Shapes of cagelike metal carbide clusters: First-principles calculations," *Physical Review B*, vol. 68, p. 241401, 2003.
- [20] P. Liu, J. A. Rodriguez, and J. T. Muckerman, "The Ti_8C_{12} metcar: A new model catalyst for hydrodesulfurization," *The Journal of Physical Chemistry*, vol. 108, p. 18796, 2004.
- [21] K. Deng, W. Duan, and B. Gu, "Theoretical studies on the electronic structure of Ti_8C_{12} isomers," *Journal of Chemical Physics*, vol. 121, p. 4123, 2004.
- [22] M. Patzschke and D. Sundholm, "Density-functional-theory studies of the infrared spectra of titanium carbide nanocrystals," *Journal of Physical Chemistry B*, vol. 109, p. 12503, 2005.
- [23] P. Hohenberg and W. Kohn, "Inhomogeneous electron gas," *Physical Review*, vol. 136, p. B864, 1964.
- [24] W. Kohn and L. J. Sham, "Self-consistent equations including exchange and correlation effects," *Physical Review*, vol. 140, p. 1113, 1965.

- [25] J. S. Pilgrim, L. R. Brock, and M. A. Duncan, "Photodissociation of niobium-carbon clusters and nanocrystals," *Journal of Physical Chemistry*, vol. 99, p. 544, 1995.
- [26] M. A. Duncan, "Synthesis and characterization of metal-carbide clusters in the gas phase," *Journal of Cluster Science*, vol. 8, p. 239, 1997.
- [27] R. Selvan and T. Pradeep, "Towards the synthesis and characterization of metallocarbohedrenes," *Chemical Physics Letters*, vol. 309, p. 149, 1999.
- [28] B. C. Guo, K. P. Kerns, and A. W. Castleman Jr., "Reactivities of $Ti_8C_{12}^+$ at thermal energies," *Journal of the American Chemical Society*, vol. 115, 1993.
- [29] S. Wei, B. C. Guo, S. A. Buzza, and A. W. Castleman Jr., "Metastable dissociation of metallocarbohedrenes - reaction channels and cluster stabilities," *Chemical Physics Letters*, vol. 97, p. 9559, 1993.
- [30] J. Purnell, S. Wei, and A. W. Castleman Jr., "Studies of the metastable decay of Met-Cars - the vanadium and niobium systems," *Chemical Physics Letters*, vol. 229, p. 105, 1994.
- [31] S. Wei and A. W. Castleman Jr., "Growth-pattern of zirconium carbon clusters - further evidence for formation of multicage structures," *Chemical Physics Letters*, vol. 227, p. 305, 1994.
- [32] G. von Helden, A. G. G. M. Tielens, D. van Heijnsbergen, M. A. Duncan, S. Hony, L. F. M. Waters, and G. Meijer, "Titanium carbide nanocrystals in circumstellar environments," *Science*, vol. 288, p. 313, 2000.
- [33] G. von Helden, D. Van Heijnsbergen, M. A. Duncan, and G. Meijer, "IR-REMPI of vanadium-carbide nanocrystals: Ideal versus truncated lattices," *Chemical Physics Letters Letters*, vol. 333, p. 350, 2001.

- [34] E. B. Wilson Jr., J. C. Decius, and P. C. Cross, *Molecular Vibrations; the Theory of Infrared and Raman Vibrational Spectra*. Dover Publications, New York, 1955.
- [35] D. van Heijnsbergen, G. von Helden, M. A. Duncan, A. J. A. van Roij, and G. Meijer, “Vibrational spectroscopy of gas-phase metal-carbide clusters and nanocrystals,” *Physics Review Letters*, vol. 83, p. 4983, 1999.
- [36] G. von Helden, D. van Heijnsbergen, and G. Meijer, “Resonant ionization using IR light: A new tool to study the spectroscopy and dynamics of gas-phase molecules and clusters,” *The Journal of Physical Chemistry*, vol. 107, p. 1671, 2003.
- [37] R. Car and M. Parrinello, “Unified approach for molecular dynamics and density-functional theory,” *Physical Review Letters*, vol. 55, p. 2471, 1985.
- [38] M. C. Payne, M. P. Teter, D. C. Allan, T. A. Arias, and J. D. Joannopoulos, “Iterative minimization techniques for ab initio total-energy calculations: Molecular dynamics and conjugate gradients,” *Reviews of Modern Physics*, vol. 64, p. 1045, 1992.
- [39] G. Kresse and J. Fürthmüller, “Efficiency of ab-initio total energy calculations for metals and semiconductors using a plane-wave basis set,” *Computational Materials Science*, vol. 6, p. 15, 1996.
- [40] G. Kresse and J. Fürthmüller, “Efficient iterative schemes for ab initio total-energy calculations using a plane-wave basis set,” *Physical Review B*, vol. 54, p. 11169, 1996.
- [41] <http://psi-k.dl.ac.uk/data/codes.html>.

- [42] M. Born and J. Oppenheimer, “Zur Quantentheorie der Molekeln,” *Annalen der Physik*, vol. 84, p. 457, 1927.
- [43] R. M. Martin, *Electronic Structure: Basic Theory and Practical Methods*. Cambridge University Press, Cambridge, UK, 2004.
- [44] D. M. Ceperley and B. J. Alder, “Ground state of the electron gas by a stochastic method,” *Physical Review Letters*, vol. 45, p. 566, 1980.
- [45] J. P. Perdew and A. Zunger, “Self-interaction correction to density-functional approximations for many-electron systems,” *Physical Review B*, vol. 23, p. 5048, 1981.
- [46] F. W. Kutzler and G. S. Painter, “Energies of atoms with nonspherical charge densities calculated with nonlocal density-functional theory,” *Physical Review Letters*, vol. 59, p. 1285, 1987.
- [47] W. E. Pickett, “Pseudopotential methods in condensed matter applications,” *Computer Physics Reports*, vol. 9, p. 115, 1989.
- [48] J. P. Perdew, J. A. Chevary, S. H. Vosko, K. A. Jackson, M. R. Pederson, D. J. Singh, and C. Fiolhais, “Atoms, molecules, solids, and surfaces: Applications of the generalized gradient approximation for exchange and correlation,” *Physical Review B*, vol. 42, p. 6671, 1992.
- [49] J. P. Perdew, K. Burke, and M. Ernzerhof, “Generalized gradient approximation made simple,” *Physical Review Letters*, vol. 77, p. 3865, 1996.
- [50] J. Ihm, A. Zunger, and M. L. Cohen, “Momentum-space formalism for the total energy of solids,” *Journal of Physics C: Solid State Physics*, vol. 12, p. 4409, 1979.

- [51] H. Hellman, *Einführung in die Quantenchemie*. Franz Deuticke, Leipzig, 1937.
- [52] R. P. Feynman, “Forces in molecules,” *Physical Review*, vol. 56, p. 340, 1939.
- [53] F. Bloch, “Über die Quantenmechanik der Elektronen in Kristallgittern,” *Zeitschrift für Physik A Hadrons and Nuclei*, vol. 52, p. 555.
- [54] D. R. Hamann, M. Schlüter, and C. Chiang, “Norm-conserving pseudopotentials,” *Physical Review Letters*, vol. 43, p. 1494, 1979.
- [55] A. M. Rappe, K. M. Rabe, E. Kaxiras, and J. D. Joannopoulos, “Optimized pseudopotentials,” *Physical Review B*, vol. 41, p. 1227, 1990.
- [56] W. Jeitschko, H. Nowotny, and F. Benesovsky, “Carbides of formula T_2MC ,” *Journal of the Less-Common Metals*, vol. 7, p. 133, 1963.
- [57] H. Goldstein, *Classical Mechanics*. Addison-Wesley, Massachusetts, 1980.
- [58] M. Tinkham, *Group Theory and Quantum Mechanics*. McGraw-Hill, New York, 1964.
- [59] J. J. Sakurai, *Modern Quantum Mechanics, (2nd Edition)*. Addison-Wesley, Massachusetts, 1994.
- [60] <http://java.sun.com/products/java-media/3D/>.
- [61] <http://java.sun.com/products/java-media/jai/>.
- [62] H. M. Deitel and P. J. Deitel, *Java How to Program*. Prentice Hall, Upper Saddle River, NJ, 1999.
- [63] H. M. Deitel, P. J. Deitel, and S. E. Santry, *Advanced Java 2 Platform; how to Program*. Prentice Hall, Upper Saddle River, NJ, 2001.
- [64] <http://java.sun.com/developer/onlineTraining/java3d/>.

- [65] <http://java.sun.com/j2se/>.
- [66] <http://java.sun.com/>.
- [67] E. A. Maxwell, *General homogeneous coordinates in space of three dimensions*. Cambridge University Press, Cambridge, UK, 1959.
- [68] J. D. Foley, A. van Dam, S. K. Feiner, and J. F. Hughes, *Computer Graphics: Principles and Practice*. Addison-Wesley, Massachusetts, 1990.